



저작자표시-비영리-변경금지 2.0 대한민국

이용자는 아래의 조건을 따르는 경우에 한하여 자유롭게

- 이 저작물을 복제, 배포, 전송, 전시, 공연 및 방송할 수 있습니다.

다음과 같은 조건을 따라야 합니다:



저작자표시. 귀하는 원저작자를 표시하여야 합니다.



비영리. 귀하는 이 저작물을 영리 목적으로 이용할 수 없습니다.



변경금지. 귀하는 이 저작물을 개작, 변형 또는 가공할 수 없습니다.

- 귀하는, 이 저작물의 재이용이나 배포의 경우, 이 저작물에 적용된 이용허락조건을 명확하게 나타내어야 합니다.
- 저작권자로부터 별도의 허가를 받으면 이러한 조건들은 적용되지 않습니다.

저작권법에 따른 이용자의 권리는 위의 내용에 의하여 영향을 받지 않습니다.

이것은 [이용허락규약\(Legal Code\)](#)을 이해하기 쉽게 요약한 것입니다.

[Disclaimer](#)

공학박사학위논문

강체벽 배열 설계를 통한 음향
메타물질의 광대역 흡차음 성능 구현

Broadband Sound Attenuation by
Acoustic Metamaterials with Rigid Partitions

2016년 8월

서울대학교 대학원

기계항공공학부

양 지 은

강체벽 배열 설계를 통한 음향 메타물질의 광대역 흡차음 성능 구현

Broadband Sound Attenuation by
Acoustic Metamaterials with Rigid Partitions

지도교수 김 윤 영

이 논문을 공학박사 학위논문으로 제출함
2016년 5월

서울대학교 대학원
기계항공공학부
양 지 은

양지은의 공학박사 학위논문을 인준함
2016년 6월

위원장 : 윤 병 동

부위원장 : 김 윤 영

위 원 : 김 도 년

위 원 : 이 진 우

위 원 : 이 중 석

ABSTRACT

Broadband Sound Attenuation by Acoustic Metamaterials with Rigid Partitions

Jieun Yang

Department of Mechanical and Aerospace Engineering

The Graduate School

Seoul National University

This thesis aims to develop acoustic metamaterials for broadband sound attenuation. Acoustic metamaterials, engineered composite structures whose properties cannot be found in nature, have received great attention for their exceptional performances to open new opportunities in engineering. Especially, sound attenuation capability of them has been widely investigated because of its relevance of practical applications. However, their acoustic performances are limited in a narrow bandwidth because physical mechanisms of them only work for single or selective frequencies, which poses a major obstacle in practical use.

The main difficulty of designing acoustic metamaterials for the broadband performances lies on the broadening the frequency ranges of effective performance

in a compact scale. To resolve this issue, this thesis presents acoustic metamaterials designed with acoustically-rigid partitions. Specifically, the proposed acoustic metamaterials are designed in a dissipative porous layer and in an acoustic layer with periodic holes to improve of sound absorption and insulation performances, respectively. The rigid partitions used in the metamaterials are arranged so as to form waveguides or resonators to control wave propagation characteristics for desired engineering purpose. Then, effective propagation distances or the effective propagation velocities of the acoustic waves propagating in the acoustic metamaterials can be tailored. It is shown that the sound attenuation performances of the proposed acoustic metamaterials are significantly enhanced in a broad range of frequency covering a low frequency range, compared with those of conventional acoustic systems without increasing a given geometric dimension.

To investigate the physical mechanism of the outstanding performances of the proposed metamaterials, detailed theoretical analyzes will be carried out for each designed structure based on effective medium approach. Numerical simulations based on finite element method and experimental studies will confirm the validity of the proposed metamaterials.

Keywords: Acoustic metamaterials, Broadband performance, Sound absorption,
Sound transmission, Metaporous layer, Effective medium model

Student Number: 2010-24065

CONTENTS

ABSTRACT	i
CONTENTS	iii
LIST OF FIGURES	vi
LIST OF TABLES	xvi
CHAPTER 1. INTRODUCTION.....	1
1.1 Research motivation.....	1
1.2 Previous works on acoustic metamaterials for sound attenuation.....	3
1.3 Research objective and coverage	6
1.4 Organization of the thesis.....	7
CHAPTER 2. MODELLING OF WAVES IN ACOUSTIC MEDIA	9
2.1 Chapter overview	9
2.2 Fundamental description of acoustic waves.....	10
2.2.1 Derivation of the acoustic wave equation	11
2.2.2 The wave solutions and relevant acoustic quantities.....	16
2.3 Acoustic waves in narrow tubes and slits.....	19
2.4 Acoustic waves in rigid-framed porous media	29

2.5 Reflection and transmission of acoustic layers	36
2.5.1 Transfer matrix modelling	36
2.5.2 Calculation of reflection and transmission coefficients	39

CHAPTER 3. ACOUSTIC METAMATERIALS INVOLVING POROUS MEDIA FOR BROADBAND SOUND ABSORPTION44

3.1 Chapter overview	44
3.2 Sound absorption of a porous layer.....	46
3.3 Metaporous layer with tuned thickness resonances.....	51
3.3.1 Design of the metaporous layer with tuned thickness resonances..	51
3.3.2 Influence of periodic vertical rigid partitions.....	55
3.3.3 Low frequency absorption improvement by gap insertion.....	60
3.3.4 Multiple thickness resonances for broadband sound absorption....	66
3.3.5 Discussions.....	72
3.4 Metaporous layer with multiple slow waves	77
3.4.1 Design of a metaporous layer with multiple slow waves	77
3.4.2 Effective medium model for the multiple slow wave media.....	79
3.4.3 Sound absorption mechanism of the metaporous layer	89
3.4.4 Discussions.....	95
3.5 Concluding remarks	104

CHAPTER 4. ACOUSTIC METAMATERIALS FOR SOUND TRANSMISSION REDUCTION.....	108
4.1 Chapter overview	108
4.2 Sound transmission through acoustic layer with holes.....	110
4.3 Metamaterial resonators for transmission reduction	116
4.3.1 Design issues on the metamaterial resonators.....	117
4.3.2 Parametric studies on the metamaterial resonator.....	119
4.3.3 Theoretical model of the proposed metamaterial	127
4.3.4 Sound insulation performance of the metamaterial system.....	133
4.4 Experiments on the proposed acoustic metamaterials.....	146
4.4.1 Experimental setup.....	146
4.4.2 Experimental results and discussion.....	148
4.5 Concluding remarks	152
CHAPTER 5. CONCLUSIONS	154
APPENDIX A. EFFECTIVE MEDIUM MODELS FOR AXISYMMETRIC METAPOROUS LAYERS	158
REFERENCES	165
ABSTRACT (KOREAN)	178

LIST OF FIGURES

Fig. 2.1 A small volume element of volume V where a fluid travels through. The unit normal vector \vec{n} are defined on the surface boundaries of the volume ∂V .
13

Fig. 2.2 The plane wave with the propagation vector \vec{k} in the cartesian coordinate.
16

Fig. 2.3 The flow propaagates along the z direction in (a) the cylindrical tube of radius R and (b) the slit confined by the planes $x = -a$ and $x = a$ 22

Fig. 2.4 The real and imaginary parts of (a) the equivalent density and (b) the equivalent bulk modulus of the air in the cylindrical tubes and the slits shown in Fig. 2.3. The cross-section dimensions are $R = 1.5$ mm and $a = 1.5$ mm.
27

Fig. 2.5 The real and imaginary parts of (a) the equivalent density and (b) the equivalent bulk modulus of the porous materials A, B, and C of Table 2.2.
35

Fig. 2.6 The real and imaginary parts of the equivalent sound velocity of the porous materials A, B, and C of Table 2.2.35

Fig. 2.7 The schematic configuration to derive the transfer matrix for the acoustic layer of finite thickness h_i37

Fig. 2.8 The multilayer of N acoustic layers under plane wave incidence.....40

Fig. 3.1 (a) A porous layer of thickness H placed on a hard wall under normal sound wave incidence. (b) Sound absorption coefficient of porous layers of various thicknesses.....47

Fig. 3.2 Enhancement of sound absorption performance of metaporous layer shown in the inset, compared to that of a homogeneous porous layer with the same thickness. ($H = 3.0$ cm and $d = 1.6$ cm)52

Fig. 3.3 Configurations of (a) an un-partitioned homogeneous porous layer and (b) periodically partitioned porous layers with the same thickness H_155

Fig. 3.4 (a) The sound absorption coefficients of the two layers in Fig. 3.3 under normal sound wave incidence along the z direction. (b) The real and imaginary parts of the surface impedances of the two layers and the characteristic impedance of the surrounding air. All the impedance values are normalized by the characteristic impedance of air (z_0). For the plots, the values of $H_1 = 3.0$ cm and $d = 1.0$ cm were used.....57

Fig. 3.5 A metaporous layer used to develop a theoretical model. (b) Comparison of the absorption coefficients of the metaporous layer (blue line: by the derived theory, circles: by finite element method) and those of the homogeneous layer (black line: by the derived theory). The color levels (varying from 0 to 0.003 m/s) in the inset denote the magnitude of the particle velocity in the unit cell at the three lowest peak frequencies. ($H_1 = 3.0$ cm, $h = 2.95$ cm, $t = 0.5$ mm, $a = 1.0$ mm and $d = 1.0$ cm)61

Fig. 3.6 (a) A unit cell configuration with two gaps connecting three porous slabs.
 (b) The sound absorption performance of a metaporous layer of the unit cell in (a) compared to that of a homogeneous porous layer. For the plots, $H_1 = 3.0$ cm, $h = 2.95$ cm, $t = 0.5$ mm, $a = 1.0$ mm and $d = 1.5$ cm are used.65

Fig. 3.7 The absorption performance of the partitioned porous layer in which the unit cell is constructed with two porous slabs with different thicknesses. It is compared with that of the original homogeneous porous layer. Solid lines denote the results by the derived theory and symbols, by the finite element analysis. ($H_1 = 3.0$ cm, $H_2 = 2.0$ cm and $d = 1.0$ cm).....67

Fig. 3.8 The configuration of a metaporous layer and its unit cell made of multiple porous slabs. (b) The metaporous layer can be modelled as a parallel connection of the two independent subcells.....68

Fig. 3.9 (a) The absorption coefficients of the metaporous layer in Fig. 3.8(a) compared with the absorption coefficients of the effective layers made of its subcells. Solid lines denote the results by the theory and symbols, by the finite element analysis. (b) The real and imaginary parts of the surface impedances of the metaporous layer compared with those of homogeneous porous layer and the characteristic impedance of the surrounding air.70

Fig. 3.10 (a) The absorption coefficients of the metaporous layer in Fig. 3.8(a) with different partition width values. (b) The absorption performance of the metaporous layer in 3.8(a) under oblique sound incidences ($\theta = 30^\circ$ and 45°)

compared to that under normal sound incidence ($\theta = 0^\circ$).....71

Fig. 3.11 The absorption coefficients of the metaporous layers made of three different unit cells shown in the inset. ($H_1 = 3.0$ cm, $h = 0.75$ cm, $h_1 = 0.75$ cm, $h_2 = 1.85$ cm, $d_1 = 1.5$ cm for the unit cells A and B; $d_2 = 1.6$ cm for the unit cell C. The gap size is set to be 1.0 mm for all the configurations.)73

Fig. 3.12 The influences of the period of the unit cell on the absorption performances of the metaporous layer composed of Unit cell C shown in the inset. The geometric parameters are the same as in Fig. 3.11 except d_2 75

Fig. 3.13 (a) A schematic configuration of the present metaporous layer and its unit cell composed of a hard-backed porous layer and rigid partitions. (b) The absorption coefficients of the metaporous layer compared to those of the homogeneous porous layer. ($H = 3.0$ cm, $d = 3.0$ cm, $t = 2.0$ mm, $b_N = 1.8$ cm, $\Delta H = H/N$, and $N = 6$. The length of the partition b_i from the bottom is determined as $b_i = d - i(d - b_N)/N$, $i = 1, 2, \dots, N$)78

Fig. 3.14 A theoretical model of the proposed metaporous layer which can be modeled as an equivalent multilayer consisting of several effective layers. (a) The unit cell configuration. (b) The unit cell is partially filled with a *static* effective medium of anisotropic material properties $\tilde{\rho}^s$ and κ^s . (c) The unit cell in (b) is sequentially divided into N layers which can be represented as effective layers of *dynamic* material properties ρ_i^e and κ_i^e 80

Fig. 3.15 (a) The metaporous layer in Fig. 3.13(a) can be modeled as a multilayer consisting of N effective layers. (b) Effective densities and (c) effective bulk moduli in the effective layers (normalized by the corresponding properties of air, ρ_0 and κ_0). The red arrow in (c) denotes the lower bound of the negative bulk modulus band of the effective layer 1.....86

Fig. 3.16 Real and imaginary parts of effective velocities in the effective layers normalized by the sound velocity of air, c_0 87

Fig. 3.17 The magnitude of particle velocities in the metaporous layer at the peak frequencies $P_1 \sim P_6$ indicated in Fig. 3.13(b). The results are obtained by numerical (left-hand side) and theoretical (right-hand side) methods. The peak frequencies obtained from the corresponding analysis are presented below.90

Fig. 3.18 Acoustic velocity fields in the metaporous at the peak frequencies (a) P_1 and P_2 , (b) $P_3 \sim P_6$ indicated in Fig. 3.13(b) obtained by the theoretical methods.92

Fig. 3.19 (a) The absorption performance of the metamaterial configuration in Fig. 3.13(a) when the porous material is removed compared with the one of the metaporous layer. (b) The magnitude of the particle velocities at the absorption peaks P_2^L and P_3^L 95

Fig. 3.20 (a) The influence of the number of the inserted partitions on the absorption performance of the metaporous layer. The geometric parameters are the same

as in Fig. 3.13(a) except N . (b) The influence of the slope angle of the partitions on the absorption performance of the metaporous layer.96

Fig. 3.21 The influence of the unit cell period on the absorption performance of the metaporous layer. The geometric parameters are the same as in Fig. 3.13(a) except d and b_i98

Fig. 3.22 (a) The unit cell configuration of the metaporous layer with the same partition lengths. (b) The wave propagation velocity in the metaporous configuration in (a). The present metaporous layer has single slow wave propagation. (c) The sound absorption performance of the single slow wave medium..... 100

Fig. 3.23 Axisymmetric configurations of the metaporous layers. (a) The rigid partition of circular shapes are aligned at the center of the layer. (b) The rigid partitions of disk shapes are aligned at the outer boundary of the layer.... 101

Fig. 3.24 The absorption coefficients obtained by numerical and theoretical methods for the metaporous layer configurations presented in Fig. 3.23(a) when b is (a) 1.15 cm and (b) 0.85 cm, respectively. 102

Fig. 3.25 The absorption coefficients obtained by numerical and theoretical methods for the metaporous layer configurations presented in Fig. 3.23(b) when b is (a) 0.55 cm and (b) 0.25 cm, respectively. 103

Fig. 4.1 (a) Acoustic double layer with periodic rectangular holes. (b) The sound transmission through the acoustic double layer in (a). 112

Fig. 4.2 Acoustic pressure fields in the xy and zx plane of the unit cell at the

frequencies (a) f_1 and (b) f_2 denoted in Fig. 4.1(b).	113
Fig. 4.3 (a) The unit cell configuration of the double layer with multiple slow wave resonator. The examples of the resonators are shown in (b) and (c).	117
Fig. 4.4 (a) The configuration of a waveguide sided by the multiple slow wave resonator in two dimensional xy plane. (b) Four configurations of the resonators considered for the study.	120
Fig. 4.5 The transmission loss through the waveguide in Fig. 4.4(a) with (a) the resonators 1 and (b) the resonator 2.	121
Fig. 4.6 The velocity fields of the waveguide with (a) the resonator 1 and (b) the resonator 2 are presented at the transmission peak frequencies in Fig. 4.5(a) and (b), respectively The corresponding peak frequencies are written on the left-hand side of each figure.....	123
Fig. 4.7 The transmission loss through the waveguide in Fig. 4.4(a) with (a) the resonators 3 and (b) the resonator 4.	124
Fig. 4.8 The velocity fields of the waveguide with (a) the resonator 3 and (b) the resonator 4 are presented at the transmission peak frequencies in Fig. 4.7(a) and (b), respectively The corresponding peak frequencies are written on the left-hand side of each figure.....	125
Fig. 4.9 The schematics of the theoretical model of the proposed metamaterials. (a) The three dimensional view of the unit cell. (b) The twodimensional configuration prsented to help the understanding of the theoretical model.	127

Fig. 4.10 (a) A sliced top view of the presented metamaterial. The one resonator indicated as red dashed line can be analyzed as the configuration in (b)..131

Fig. 4.11 (a) The configuration of the considered metamaterial. (b) The effective sound velocity in effective medium filling the resonator normalized to the sound velocity in air (c_0). (c) The transmission loss through the considered metamaterial..... 135

Fig. 4.12 (a) The configuration of the considered metamaterial. (b) The effective sound velocity in effective medium filling the resonator normalized to the sound velocity in air (c_0). (c) The transmission loss through the considered metamaterial..... 136

Fig. 4.13 The contour plots of the (a)-(d) acoustic pressure and (e)-(h) magnitude of velocities in the metamaterial presented in Fig. 4.12(a) at the transmission loss peak frequencies in Fig. 4.12(c). The corresponding peak frequencies are written on the left-hand side..... 138

Fig. 4.14 (a) The configuration of the considered metamaterial. (b) The effective sound velocities in effective media filling the resonator normalized to the sound velocity in air (c_0). (c) The transmission loss through the considered metamaterial..... 140

Fig. 4.15 (a) The configuration of the considered metamaterial. (b) The effective sound velocities in effective media filling the resonator normalized to the sound velocity in air (c_0). (c) The transmission loss through the considered

metamaterial.....	141
Fig. 4.16 The contour plots of the (a)-(e) acoustic pressure and (f)-(j) magnitude of velocities in the metamaterial presented in Fig. 4.15(a) at the transmission loss peak frequencies in Fig. 4.15(c).....	142
Fig. 4.17 (a) The cross section in the xy plane of the configurations composed of multiple unit cells. (b) The transmission loss curves obtained by finite element simulations using the configurations in (a).....	145
Fig. 4.18 Schematic diagram of the standing wave impedance tube for measuring sound transmission loss.....	146
Fig. 4.19 (a) Designed metamaterials are fabricated by bonding three layers made of acrylic plates; Layer A, B, and A'. (b) Photograph of the fabricated metamaterials. (c) Cross sections of the fabricated samples.	149
Fig. 4.20 The results of the experiments for the samples in Fig. 4.19 for frequency range upto 1600 Hz. The results by the theoretical model are also presented for comparison. (a) Sample 0, (b) Sample 1, (c) Sample 2, and (d) Sample 3.	151
Fig. A.1 Axisymmetric configurations of the metaporous layer of radius R when the rigid partition of circular shapes are aligned at the center of the layer. The radius of the rigid partitions are set to be equal to b_i	159
Fig.A.2 (b) Axisymmetric configurations of the metaporous layer of radius R when the rigid partitions of disk shapes are aligned at the outer boundary of the	

layer. The inner radius of the rigid partitions are set to be equal to a_i163

LIST OF TABLES

Table 2.1 The material properties of the air.28

Table 2.2 The characterization parameters of the porous materials [52]–[54].34

CHAPTER 1.

INTRODUCTION

1.1 Research motivation

Acoustic waves or sound waves exist everywhere in human lives. Propagating in an elastic medium, such as a gas, a liquid, a solid, acoustic waves carry energy by deriving particle motions of the medium. The existence of the acoustic waves allows us to do a lot of things, for example, to interact with other people, to appreciate music, etc. However, there also exists unwanted sound perceived by a human being, which is called noise. The sources of noise are various; industrial machines, vehicles such as cars, trains, and airplanes, or sounds from neighbor. Human's exposure to the noises may be hazardous, give emotional/mental stress, even it may result in loss of hearing or social issues when severe situation.

For over 100 years, there have been lots of efforts to reduce unwanted noises by developing acoustic structures and sound-attenuating materials. The noise problem

can be categorized into two categories; sound absorption and sound transmission problem. When a sound strikes a finite-thickness medium, it is transmitted, absorbed or reflected. The sound absorption problem is defined as a situation to reduce reflected sound energy when the absorbing structures are placed on a hard wall. The sound transmission problem is defined as a situation when a transmitted medium behind the finite-thickness medium is assumed to be infinite so that there will be no waves reflected back in the transmitted medium. In the transmission problem, it needs to consider both of reflected and transmitted waves.

In either problem, a general rule to the noise reduction problem is that sufficiently large structures are needed to attenuate the sound energy. This is due to the fact that the dimension of the absorbing/insulating structures should be comparable to the wavelength of the incident sound wave. The acoustic waves are composed of frequency components in wide frequency range, ranging from 20 Hz to 20 kHz for audible sound. In air, in which sound velocity is about 343 m/s, the wavelength ranges from 17.15 mm to 17.15 m. However, in many practical applications, the space to install the acoustic structures for noise reduction is limited, thus this limitation makes it difficult to control broadband sound especially in the low frequency range.

The main difficulty of the low frequency sound control comes from the lack of high-refractive acoustic medium, unlike in electromagnetic counterpart. For recent years,

acoustic metamaterials have received great attention for their ability to overcome the intrinsic limitation on the acoustic medium. The researchers have shown that the low frequency sound attenuation in deep-subwavelength scale metamaterials is possible by employing local resonance phenomena [1]–[9], wave path elongation by coiling-up spaces [10], [11], and slow waves [12]. Nevertheless, their performances are inevitably limited in a narrow bandwidth because physical mechanisms for the performance only work for single or only few frequencies, which poses a major obstacle in practical use. Except few works [13]–[15], broadband sound attenuation capability of acoustic metamaterials has not received much attention in spite of its practical importance. Therefore, it is still desirable to develop acoustic metamaterials for broadband sound attenuation while maintaining a compact size.

Motivated by the issue, this thesis is dedicated to designing acoustic metamaterials for broadband sound absorption and insulation capability. In the following sections, precedent studies on the sound attenuation of acoustic metamaterials will be reviewed. Then research coverage and organization of the thesis will be introduced.

1.2 Previous works on acoustic metamaterials for sound attenuation

Metamaterials are artificially-designed composites whose characteristics cannot be

found in nature. The metamaterials, firstly devised in electromagnetic fields, have captured great attention of scientists and engineers for their possibility to open new opportunities in technology. Numerous works have shown that the metamaterials can be used for achievement of negative parameters [16]–[18], high absorption [19]–[22], extraordinary transmission [23]–[26], subwavelength imaging [27], [28], etc.

Inspired by the metamaterials in electromagnetic fields, acoustic metamaterials have been widely investigated as well. It was revealed that the anomalous wave phenomena observed in the electromagnetic metamaterials can also be achieved in the acoustic metamaterials. Among the numerous works, their capability to attenuate sound energy in a subwavelength scale is a prominent topic because of its relevance in practical applications.

The noise reduction performance of the acoustic metamaterials was mostly achieved by using negative material properties. The negative acoustic density is realized by dipolar resonance of locally resonant composites [1], [2], [6]. The resonant composite is composed of a soft medium, such as rubber or membranes, as a spring and a solid inclusion as a mass. On the other hand, the negative bulk modulus is realized by a waveguide with an array of monopolar resonators [29], [30]. Due to the local resonances of the resonators, the negative bulk modulus is caused by the dispersion characteristic of the metamaterial. More recently, an acoustic metamaterial that has negative density and bulk modulus simultaneously in distinct

frequency range was also proposed [31]. At the frequency range of the negative properties, the relative motion of the metamaterial medium is opposite to the direction of the driving force of the medium. Therefore, the metamaterials act as noise barriers by interrupting wave propagation.

Another type of acoustic metamaterials for noise reduction is to use a strategy of elongation of wave propagation distance. There are two ways of elongating the wave propagation distance; by elongating actual path [10], [11] and by elongating effective propagation distance [12]. To increase the actual wave propagation distance, coiling-up is usually used. The effective propagation distance is able to be increased when the effective sound velocity in the medium can be reduced. It can be realized by using local resonance of an array of resonators, such as in the acoustic metamaterials for negative bulk modulus. The increase of the propagation distance, either actual or effective, means that the refractive index of the acoustic medium is higher than that of the air, which is not observed in existing acoustic medium. Once the high-refractive medium is realized, the corresponding frequency for the resonant absorption can be shifted to much lower frequency.

However, the acoustic performances of the acoustic metamaterials presented so far are limited in narrow bandwidth of low frequency because they were mostly focused on the findings of the anomalous phenomena. As mentioned before, the broadband performance is crucial for the practical purpose, therefore, researches on the acoustic

metamaterials for broadband sound attenuation should be carried out. One of the key to achieve broadband performance would be a proper incorporation of dissipative mechanism to the acoustic metamaterials. It has been started several attempts to involve dissipative media recently [13], [15], [32], [33], however, there is much room for improvement.

1.3 Research objective and coverage

The main objective of the thesis is to develop acoustic metamaterials for broadband sound absorption and insulation performances. In particular, considering practical applications, this thesis provides acoustic metamaterials in two representative situations; sound absorption of acoustic metamaterials involving acoustic porous materials and sound transmission through acoustic metamaterials with holes to allow airflow. As mentioned in the previous section, the absorption problem in the thesis considers a situation when sound-absorbing structure is placed on a hard wall so that only reflected waves will be considered. The transmission problem considers both of reflected and transmitted waves by the metamaterials under acoustic excitation.

In each chapter, to achieve the major objectives, the acoustic performances and involving physics of the nominal case will be investigated first. Then acoustic

metamaterials to achieve the desired performances will be presented. The acoustic metamaterials proposed in the thesis is designed by rigid partitioning that forms a structure to guide wave propagation or change wave propagation properties in the acoustic metamaterials. For the proposed acoustic metamaterials, theoretical models to describe wave propagation characteristic in the metamaterials will be presented. In addition, their outstanding acoustic performances will be validated by numerical simulations based on finite element method and experiments.

1.4 Organization of the thesis

The thesis is organized as follows.

In chapter 1, a brief explanation on the noise reduction problem and its precedent studies are addressed. Especially, the acoustic metamaterials for sound absorption and insulation are introduced and their limitation on the acoustic performance are introduced. Then, the necessity and significance of the development of the acoustic metamaterials for broadband sound attenuation are highlighted as a research objective also with the research coverage of the thesis.

In chapter 2, theoretical backgrounds and fundamental description of acoustic waves will be presented. Basic governing equation of the acoustic waves in inviscid

acoustic media, its solution and relevant acoustic quantities that are useful to describe sound propagation will be presented. Then, to provide basic knowledge about dissipative materials considered in the thesis, modelling of acoustic waves in narrow waveguides and in acoustic porous materials will be introduced.

In chapter 3, acoustic metamaterials for broadband sound absorption are introduced. In this chapter, the acoustic metamaterial designed with porous layer, so-called metaporous layers, will be presented to effectively achieve broadband sound absorption performance by incorporating dissipative property of an acoustic medium. Two representative metaporous layers will be introduced; one with multiple tuned resonances and one with multiple slow waves.

In chapter 4, acoustic metamaterials for broadband transmission reduction are introduced, especially considering acoustic double layers with holes. To suppress the sound transmission effectively, a newly-designed resonator based on multiple slow wave mechanism will be presented. The effects of multiple slow waves in the transmission problem will be investigated as well.

Finally, the overall conclusion of the thesis is presented in chapter 5.

CHAPTER 2.

MODELLING OF WAVES IN ACOUSTIC MEDIA

2.1 Chapter overview

This chapter aims to present the theoretical backgrounds necessary to understand general methodologies to describe wave propagations in acoustic media. Especially, this thesis deals with acoustic media with viscous and thermal losses including wave propagations in porous media and narrow waveguides where inherent losses of air cannot be ignored. Therefore, the description of acoustic waves in non-viscous media as well as in viscous media will be presented in the following sections. In section 2.2, fundamental description of acoustic waves in inviscid media will be presented. The basic governing equation for sound waves, its solution and relevant acoustic quantities will be derived. Then, the wave equations are expanded to the viscous media represented by complex material properties through section 2.3 and section 2.4. Section 2.4 is dedicated to the description of the waves in narrow tubes and slits,

when the viscous and thermal losses at surrounding rigid walls have significantly influence on the wave propagation. In section 2.4, a modelling method of the sound propagation in rigid-framed porous medium will be introduced as well as the parameters to determine the characteristic of the porous medium. Finally, in section 2.5, a method to calculate the transmitted and reflected waves through acoustic layers will be presented.

2.2 Fundamental description of acoustic waves

Acoustic waves are a type of longitudinal waves that propagate by means of adiabatic compression and decompression. The acoustic waves are represented by pressure fluctuations in a compressible fluid. The oscillations of the particle located at the position caused by an acoustic source result in interaction among near particles in such a way that energy propagates through the medium. In this section, the derivation of the linearized wave equation for the acoustic waves in lossless medium will be presented. In addition, the solutions of the wave equation and some important acoustic quantities which are necessary to describe the wave motion and phenomena in acoustic medium.

2.2.1 Derivation of the acoustic wave equation

The governing equation of the acoustic waves can be developed from the equation of the state, the equation of continuity (conservation of mass), and the equation of motion for compressible fluids.

The equation of the state

The acoustic pressure fluctuation p is defined as the difference of the instantaneous pressure P and the equilibrium pressure P_0 at the equilibrium position of the fluid element. Likewise, the density fluctuation is defined as $\rho - \rho_0$, where ρ and ρ_0 are instantaneous and equilibrium density, respectively. In adiabatic process, the linearized relationship between pressure and density fluctuations can be represented by

$$P - P_0 = \left(\frac{\partial P}{\partial \rho} \right)_{\rho_0} (\rho - \rho_0). \quad (2.1)$$

When the adiabatic bulk modulus is defined as $\kappa_0 = \rho_0 \left(\frac{\partial P}{\partial \rho} \right)_{\rho_0}$, Eq. (2.1) can be rewritten as

$$P - P_0 = \kappa_0 \frac{\rho - \rho_0}{\rho_0}. \quad (2.2)$$

The change in density for a given ambient fluid density is defined as condensation, $s = (\rho - \rho_0) / \rho_0$, thus it gives the result

$$p = \kappa_0 s . \quad (2.3)$$

The equation of continuity (Conservation of mass)

Consider a flow of fluid travels with particle velocity \vec{v} through a volume element shown in Fig. 2.1. The volume of the volume element is given by V with boundary ∂V and the normal unit vector directed outwards the volume element is \vec{n} . The net rate of fluid mass flows into the volume through the surfaces should be equal to the rate of increase of the mass within the volume. Then the conservation of mass is expressed by the relation

$$-\frac{\partial}{\partial t} \int_V \rho dV = \oint_{\partial V} \rho (\vec{v} \cdot \vec{n}) dS . \quad (2.4)$$

The surface integral on the right-hand side of Eq. (2.4) is transformed into a volume integral by the Gauss theorem, $\oint_{\partial V} (\vec{F} \cdot \vec{n}) dS = \int_V (\nabla \cdot \vec{F}) dV$, where \vec{F} is an arbitrary continuously differentiable vector field. Thus, Eq. (2.4) becomes

$$\int_V \left(\frac{\partial \rho}{\partial t} + \nabla \cdot (\rho \vec{v}) \right) dV = 0 , \quad (2.5)$$

which leads to the continuity equation

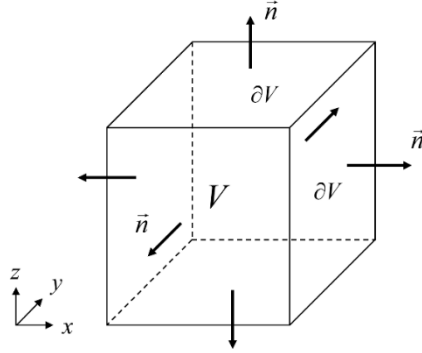


Fig. 2.1 A small volume element of volume V where a fluid travels through. The unit normal vector \vec{n} are defined on the surface boundaries of the volume ∂V .

$$\frac{\partial \rho}{\partial t} + \nabla \cdot (\rho \vec{v}) = 0. \quad (2.6)$$

Recall that $s = (\rho - \rho_0) / \rho_0$ or $\rho = \rho_0(1 + s)$, and assume that s is very small, the linearized equation of the continuity becomes

$$\frac{\partial s}{\partial t} + \nabla \cdot \vec{v} = 0. \quad (2.7)$$

The equation of motion

Now consider that the volume element in Fig. 2.1 is subject to a hydrostatic pressure P . Then, by the Newton's second law, the equation of motion is expressed as

$$-\oint_{\partial V} P \vec{n} dS = \int_V \rho \frac{d\vec{v}}{dt} dV. \quad (2.8)$$

By definition, the material derivative d/dt is defined for any tensor field G as $dG/dt = \partial G/\partial t + \bar{v} \cdot \nabla G$, where \bar{v} is the flow velocity. In addition, again by the Gauss theorem, Eq. (2.4) is rewritten as

$$-\nabla P = \rho \left[\frac{\partial \bar{v}}{\partial t} + (\bar{v} \cdot \nabla) \bar{v} \right]. \quad (2.9)$$

By substituting $\nabla P = \nabla p$ and $\rho = \rho_0(1+s)$, Eq. (2.9) becomes

$$-\nabla p = \rho_0(1+s) \left[\frac{\partial \bar{v}}{\partial t} + (\bar{v} \cdot \nabla) \bar{v} \right]. \quad (2.10)$$

Assume that $|\partial \bar{v}/\partial t| \gg |(\bar{v} \cdot \nabla) \bar{v}|$ and s is very small, the linearized Euler's equation can be obtained as

$$-\nabla p = \rho_0 \frac{\partial \bar{v}}{\partial t}. \quad (2.11)$$

The linearized wave equation

The combination of the linearized equations, Eqs. (2.3), (2.7) and (2.11), can give the linearized wave equation for the acoustic waves. Firstly, the combination of Eqs. (2.3) and (2.7) gives

$$\frac{1}{\kappa_0} \frac{\partial p}{\partial t} + \nabla \cdot \vec{v} = 0. \quad (2.12)$$

Then take the divergence of Eq. (2.11) and the time derivative of Eq. (2.12) multiplied by ρ_0 as

$$-\nabla^2 p = \nabla \cdot \left(\rho_0 \frac{\partial \vec{v}}{\partial t} \right), \quad (2.13)$$

$$\frac{\rho_0}{\kappa_0} \frac{\partial^2 p}{\partial t^2} + \nabla \cdot \left(\rho_0 \frac{\partial \vec{v}}{\partial t} \right) = 0. \quad (2.14)$$

Elimination of the divergence term of the two equations results in the linearized wave equation

$$\nabla^2 p - \frac{1}{c^2} \frac{\partial^2 p}{\partial t^2} = 0, \quad (2.15)$$

with the thermodynamic speed of sound c , which is defined by the relation of the acoustic mass density ρ_0 and bulk modulus κ_0 of the medium as

$$c = \sqrt{\frac{\kappa_0}{\rho_0}}. \quad (2.16)$$

The linearized wave equation holds for the propagation of small amplitude pressure fluctuation in inviscid, adiabatic medium.

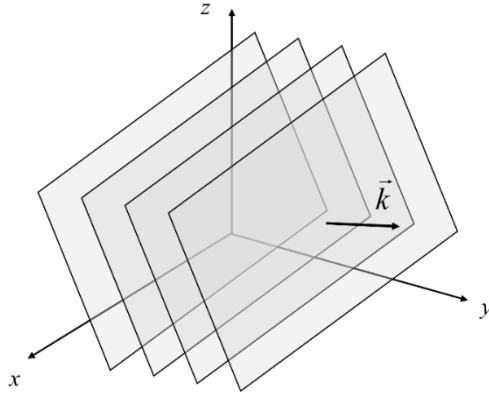


Fig. 2.2 The plane wave with the propagation vector \vec{k} in the cartesian coordinate.

2.2.2 The wave solutions and relevant acoustic quantities

The time-harmonic plane wave solution in Cartesian coordinates of the Eq. (2.15)

propagating in the direction of \vec{k} , such as shown in Fig. 2.2, is given by

$$p(\vec{x}, t) = A e^{j(\omega t - \vec{k} \cdot \vec{x})}, \quad (2.17)$$

where ω is radial frequency ($\omega = 2\pi f$) of propagating wave. For three-

dimensional case, \vec{k} is a vector of directional components (k_x, k_y, k_z) and its

magnitude $|\vec{k}| = \sqrt{k_x^2 + k_y^2 + k_z^2}$ is the wave number defined as $2\pi/\lambda$, where λ is

the wavelength at the specific frequency. The frequency, the wavenumber and the

wave velocity is related by $c = f\lambda$ and it also can be rewritten as $c = \omega/k$. In the

plane wave assumption, each acoustic variable has constant amplitude and phase on any plane perpendicular to the direction of propagation and the surfaces of constant phase are given by $\vec{k} \cdot \vec{x} = \text{constant}$. In lossless medium, material properties as well as wave constants have real values.

In time-harmonic assumption, the linearized Euler's equation, Eq. (2.11) can be rewritten in terms of particle velocity as

$$\vec{v} = -\frac{1}{j\omega\rho_0} \nabla p. \quad (2.18)$$

Then by substituting Eq. (2.17) into Eq. (2.18), the velocity can be expressed as

$$\vec{v} = \frac{A\hat{k}}{\rho_0 c} e^{j(\omega t - \vec{k} \cdot \vec{x})}, \quad (2.19)$$

where \hat{k} means the unit vector along the propagation direction \vec{k} .

One of the important acoustic quantity is acoustic impedance. The specific acoustic impedance (or characteristic acoustic impedance) is the acoustic impedance per unit area, defined as the ratio of acoustic pressure to the associated particle velocity in the medium,

$$z_c = \frac{p}{v}. \quad (2.20)$$

In general, for plane waves, this ratio is $z_c = \pm \rho_0 c$, where the sign is determined by the propagation direction with respect to the considered coordinate. The acoustic impedance is a very useful notion to determine the characteristic of the acoustic medium as well as to evaluate the reflected or transmitted waves when finite, multiple acoustic media are considered. The characteristic impedance is purely real for lossless medium, however, it can be complex both with real and imaginary parts, which represent the resistance and reactance of the material, respectively.

The acoustic waves transport the energy by potential and kinetic energy forms. When a fluid element that occupies volume V_0 , the potential energy E_p associated with a volume change from V_0 to V and kinetic energy E_k of the mass element of $\rho_0 V_0$ can be expressed as

$$E_p = -\int_{V_0}^V p dV, \quad (2.21)$$

$$E_k = \frac{1}{2} \rho_0 V_0 v^2, \quad (2.22)$$

respectively. Using that $\rho V = \text{const.}$, the total acoustic energy becomes after some derivations,

$$E = E_p + E_k = \frac{1}{2} \rho_0 V_0 \left[\left(\frac{p}{\rho_0 c} \right)^2 + v^2 \right]. \quad (2.23)$$

Then the energy density is obtained by

$$E_d = \frac{1}{T} \int_0^T \frac{E}{V_0} dt = \frac{1}{2} \rho_0 \left[\left(\frac{A_p}{\rho_0 c} \right)^2 + A_v^2 \right], \quad (2.24)$$

where A_p and A_v are amplitude of the acoustic pressure and particle velocity, respectively. By using Eq. (2.20) and the characteristic impedance $z_c = \pm \rho_0 c$, Eq. (2.24) becomes

$$E_d = \frac{A_p^2}{2\rho_0 c^2} = \frac{A_p A_v}{2c} = \frac{\rho_0 A_v^2}{2}. \quad (2.25)$$

Note that the energy density is proportional to the squared value of amplitude of the acoustic pressure or the particle velocity.

2.3 Acoustic waves in narrow tubes and slits

In section 2.2, the wave equations and solutions for the inviscid acoustic medium are presented. However, for example, when the sound waves propagate in structures and geometries with small dimensions, the sound waves become attenuated because of viscous losses and thermal conduction of the boundaries. Therefore, the effects of dissipative losses should be involved in describing the waves in the such media.

Therefore, in this section, the modelling of sound propagation in narrow tubes and slits is presented based on Refs. [34], [35]. Starting from the linearized Navier-Stokes equations, this section aims to derive the equations of the equivalent acoustic density and bulk modulus to express the waves in such media as in an acoustic media with complex material properties governed by the linearized wave equation presented in Eq. (2.15). The term ‘*effective*’ is also used instead of ‘*equivalent*’ to indicate the material properties of the porous material, however, ‘*equivalent*’ was used in this thesis to distinguish from the ‘*effective*’ material properties of the metamaterials that will be shown in Chapter 3 and 4. The introduction of this modelling also will be useful to understand the modelling of the porous materials presented later in section 2.4.

The linearized Navier-Stokes equations of ideal gas for the acoustic pressure p , the particle velocity \vec{v} , the acoustic temperature τ of the fluid in a pore, i.e. the variation of the temperature in an acoustic field are given by

$$\rho_0 \frac{\partial \vec{v}}{\partial t} = -\nabla p + \frac{4}{3} \mu \nabla (\nabla \cdot \vec{v}) - \mu \nabla \times \nabla \times \vec{v}, \quad (2.26)$$

$$\frac{\partial \rho}{\partial t} + \rho_0 \nabla \cdot \vec{v} = 0, \quad (2.27)$$

$$k_t \nabla^2 \tau = \frac{T_0}{P_0} \left(\rho_0 c_v \frac{\partial \tau}{\partial t} - P_0 c_p \frac{\partial \rho}{\partial t} \right), \quad (2.28)$$

$$p = \frac{P_0}{\rho_0 T_0} (\rho_0 \tau + \rho T_0), \quad (2.29)$$

where λ_d is dilatational viscosity coefficient, μ is shear viscosity coefficient, k_t is thermal conductivity, c_v is specific heat at constant volume, and c_p is a specific heat at constant pressure. Eqs. (2.26) to (2.29) represent the conservation of mass, conservation of momentum, conservation of energy, and the equation of the state, respectively. The simplification of Eqs. (2.26) and (2.28) yields

$$\rho_0 \frac{\partial \bar{v}}{\partial t} = -\nabla p + \mu \Delta \bar{v}, \quad (2.30)$$

$$\rho_0 c_p \frac{\partial \tau}{\partial t} = k_t \nabla^2 \tau + \frac{\partial p}{\partial t}. \quad (2.31)$$

Figure 2.3 shows cross-sectional views of the considered narrow acoustic waveguide. Figure 2.3(a) and Fig. 2.3(b) correspond to the one of a cylindrical tube of radius R and a slit of width $2a$, respectively. The slit is confined by the planes $x = a$ and $x = -a$, there is no limitation along the y direction. Because the cross-section dimension of the tubes and slits are very small compared to the wavelength, the pressure is considered constant on a cross-section. The boundary conditions at the walls surrounding the tubes and slits are $\bar{v} = 0$ and $\tau = 0$.

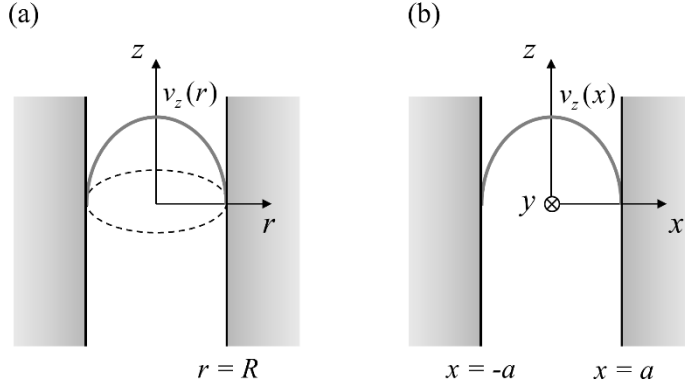


Fig. 2.3 The flow propaagates along the z direction in (a) the cylindrical tube of radius R and (b) the slit confined by the planes $x = -a$ and $x = a$.

Equivalent acoustic density

For a wave propagating along the z direction, Eq. (2.30) can be rewritten in time-harmonic acoustic fields in arbitrary Cartesian coordinate as

$$j\omega\rho_0 v_z = -\frac{\partial p}{\partial z} + \mu \left[\frac{\partial^2 v_z}{\partial x^2} + \frac{\partial^2 v_z}{\partial y^2} \right]. \quad (2.32)$$

When the above equation is transformed for the considered coordinates of the cylindrical tube and for the slit shown in Fig. 2.3, it becomes

$$j\omega\rho_0 v_z = -\frac{\partial p}{\partial z} + \mu \frac{1}{r} \frac{\partial}{\partial r} \left(r \frac{\partial v_z}{\partial r} \right), \quad (2.33)$$

$$j\omega\rho_0 v_z = -\frac{\partial p}{\partial z} + \mu \frac{\partial^2 v_z}{\partial x^2}, \quad (2.34)$$

for the cylindrical tube and the slit, respectively. Considering the boundary condition on the surrounding walls $\bar{v} = 0$, the solution of Eqs. (2.33) and (2.34) are

$$v_z = -\frac{1}{j\omega\rho_0} \frac{\partial p}{\partial z} \left(1 - \frac{J_0(lr)}{J_0(lR)} \right), \quad (2.35)$$

$$v_z = -\frac{1}{j\omega\rho_0} \frac{\partial p}{\partial z} \left(1 - \frac{\cosh(l'x)}{\cosh(la)} \right), \quad (2.36)$$

where $l = (-j\omega\rho_0/\mu)^{1/2}$, $l' = (j\omega\rho_0/\mu)^{1/2}$ and J_0 is the zero order Bessel function of the first kind. The equivalent density of the air in the tubes and slits is defined by rewriting Eq. (2.27) as

$$\rho = -\frac{1}{j\omega\bar{v}_z} \frac{\partial p}{\partial z}, \quad (2.37)$$

with the mean velocity over the cross-section, \bar{v}_z . The mean velocity of Eqs. (2.34) and (2.35) can be obtained as

$$\bar{v}_z = \frac{\int_0^R 2\pi r v_z dr}{\pi R^2} = -\frac{1}{j\omega\rho_0} \frac{\partial p}{\partial z} \left[1 - \frac{2}{R\sqrt{-j\omega\rho_0/\mu}} \frac{J_0(R\sqrt{-j\omega\rho_0/\mu})}{J_1(R\sqrt{-j\omega\rho_0/\mu})} \right], \quad (2.38)$$

$$\bar{v}_z = \frac{\int_{-a}^a v_z dx}{2a} = -\frac{1}{j\omega\rho_0} \frac{\partial p}{\partial z} \left[1 - \frac{\tanh(a\sqrt{j\omega\rho_0/\mu})}{a\sqrt{j\omega\rho_0/\mu}} \right], \quad (2.39)$$

respectively. Therefore, the equivalent acoustic density of the air in the tubes ρ_t and the slits ρ_s are obtained by Eqs. (2.37), (2.38) and (2.39) as

$$\rho_t = \rho_0 \left/ \left[1 - \frac{2}{R\sqrt{-j\omega\rho_0/\mu}} \frac{J_0(R\sqrt{-j\omega\rho_0/\mu})}{J_1(R\sqrt{-j\omega\rho_0/\mu})} \right] \right., \quad (2.40)$$

$$\rho_s = \rho_0 \left/ \left[1 - \frac{\tanh(a\sqrt{j\omega\rho_0/\mu})}{a\sqrt{j\omega\rho_0/\mu}} \right] \right.. \quad (2.41)$$

Equivalent bulk modulus

For the waves propagating along the z direction in the tubes and slits, the variations of the temperature τ in the z direction are smaller than in the cross-sectional direction x and y . Therefore, Eq. (2.31) can be rewritten in time-harmonic acoustic fields as

$$\frac{\partial^2 \tau}{\partial x^2} + \frac{\partial^2 \tau}{\partial y^2} - j\omega \frac{\tau}{v'} = -j \frac{\omega}{k_t} p, \quad (2.42)$$

where $v' = k_t / \rho_0 c_p$. Then the above equation can be expressed with the defined angular frequency $\omega' = \omega \mu / \rho_0 v'$

$$\frac{\partial^2 \tau}{\partial x^2} + \frac{\partial^2 \tau}{\partial y^2} - j\omega' \frac{\rho_0}{v'} \tau = -j \frac{\omega'}{k_t \text{Pr}} p, \quad (2.43)$$

where $\text{Pr} = \mu/(\rho_0 \nu)$ is the Prandtl number. When the Eq. (2.32) is rewritten as

$$\frac{\partial^2 v_z}{\partial x^2} + \frac{\partial^2 v_z}{\partial y^2} - j\omega \frac{\rho_0}{\mu} v_z = \frac{1}{\mu} \frac{\partial p}{\partial z}, \quad (2.44)$$

the similarity between Eqs. (2.43) and (2.44) can be noticed. By comparing two equations, the solutions τ and v_z of the equations can be expressed as

$$\tau = \frac{p\nu'}{k_t} \psi(x, y, \text{Pr } \omega), \quad (2.45)$$

$$v_z = -\frac{\partial p}{\partial z} \psi(x, y, \omega) \frac{1}{j\omega\rho_0}, \quad (2.46)$$

where $\psi(x, y, \omega)$ is a solution of the equation

$$\frac{\partial^2 \psi}{\partial x_1^2} + \frac{\partial^2 \psi}{\partial x_2^2} - j\omega \frac{\rho_0}{\mu} \psi = -j\omega \frac{\rho_0}{\mu}, \quad (2.47)$$

with the boundary condition $\psi = 0$ on the walls. Then the equation for the equivalent density Eq. (2.37) can be expressed as

$$\rho = -\frac{\partial p}{\partial z} \frac{1}{j\omega \bar{v}_z} = \frac{\rho_0}{\bar{\psi}(x, y, \omega)}. \quad (2.48)$$

By the definition of the bulk modulus, the equivalent bulk modulus becomes

$$\kappa = \rho_0 \frac{p}{\rho}, \quad (2.49)$$

with the mean value of density over the cross section, $\bar{\rho}$. From the equation of state given in Eq. (2.30), $\bar{\rho}$ becomes

$$\bar{\rho} = \frac{\rho_0}{P_0} p - \frac{\rho_0}{T_0} \bar{\tau}. \quad (2.50)$$

Then combining Eq. (2.46), (2.50) and (2.51), the equivalent bulk modulus is

$$\kappa = \frac{P_0}{1 - \frac{P_0}{T_0} \frac{v'}{k_t} \bar{\psi}(x_1, x_2, \text{Pr } \omega)}. \quad (2.51)$$

By using the relations $(c_p - c_v) = P_0 / \rho_0 T_0$ and $\gamma = c_p / c_v$, the above equation becomes

$$\kappa = \frac{\gamma P_0}{\gamma - (\gamma - 1) \bar{\psi}(x, y, \text{Pr } \omega)}. \quad (2.52)$$

By comparing Eq. (2.49) with the equations for the equivalent densities in Eq. (2.41) and (2.42), $\bar{\psi}(x, y, \text{Pr } \omega)$ can be obtained. Therefore, for the cylindrical tubes the equivalent bulk modulus is

$$\kappa_t = \frac{\gamma P_0}{1 + (\gamma - 1) \frac{2}{R\sqrt{-j\omega\rho_0 \text{Pr}/\mu}} \frac{J_1(R\sqrt{-j\omega\rho_0 \text{Pr}/\mu})}{J_0(R\sqrt{-j\omega\rho_0 \text{Pr}/\mu})}}. \quad (2.53)$$

And the equivalent bulk modulus for the slits is

$$\kappa_s = \frac{\gamma P_0}{1 + (\gamma - 1) \tanh(a\sqrt{j\omega\rho_0 \text{Pr}/\mu}) / (a\sqrt{j\omega\rho_0 \text{Pr}/\mu})}. \quad (2.54)$$

Figure 2.4 shows the equivalent acoustic density and the bulk modulus of the air in the tubes and slits for the cross-sectional dimensions $R = 1.5$ mm and $a = 1.5$ mm normalized to the acoustic density and the bulk modulus of air in free domain. For calculation, the material properties of the air presented in Table 2.1 are used. The equivalent values have imaginary parts to represent the viscous and thermal losses of the equivalent medium. Using the equivalent material properties, the waves in

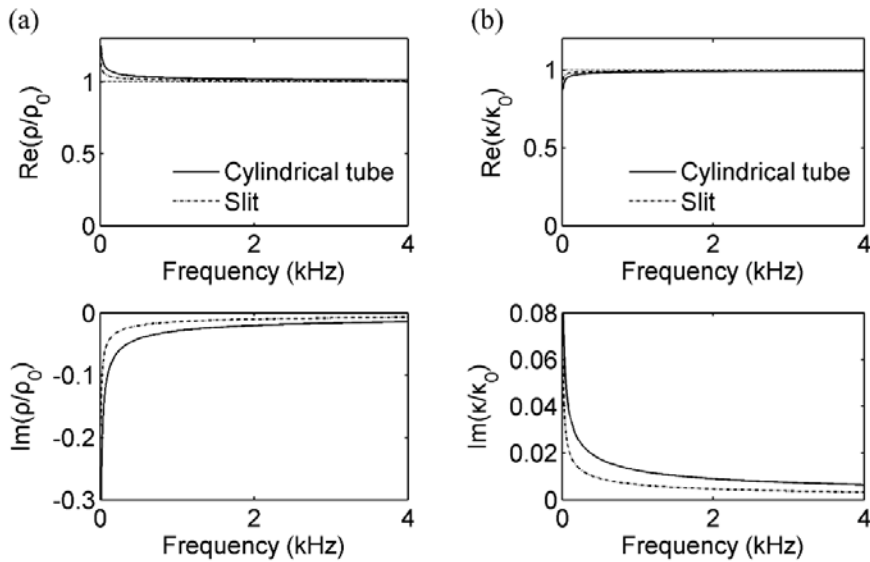


Fig. 2.4 The real and imaginary parts of (a) the equivalent density and (b) the equivalent bulk modulus of the air in the cylindrical tubes and the slits shown in Fig. 2.3. The cross-section dimensions are $R = 1.5$ mm and $a = 1.5$ mm.

Table 2.1 The material properties of the air.

Material property	Symbol	Unit	Value
Acoustic density	ρ_0	[kg/m ³]	1.213
Specific heat ratio	γ	.	1.4
Atmospheric pressure	P_0	[Pa]	101325
Viscosity	μ_0	[kg/m/s]	1.839×10^{-5}
Sound speed	c_0	[m/s]	$341.97 (= \sqrt{\gamma P_0 / \rho_0})$
Bulk modulus	κ_0	[Pa]	$1.42 \times 10^5 (= \rho_0 c_0^2)$
Specific heat	c_p	[J/kg/K]	1005
Kinematic viscosity	ν	[m ² /s]	1.511×10^{-5}
Fluid dynamic viscosity	μ	[kg/m/s]	$1.833 \times 10^{-5} (= \rho_0 \nu_f)$
Thermal conductivity	k_t	[W/m/K]	0.0257
Prandtl number	Pr	.	$0.7167 (= c_p \mu / k_t)$

such medium can be interpreted as if in an acoustic medium governed by the linearized wave equation in Eq. (2.16). Therefore, just like in the inviscid acoustic medium, the sound velocity and the characteristic impedance can be defined by using the derived equivalent material properties.

From the theoretical derivations made above, it is noticeable that the effects of the viscosity and the thermal conduction is decoupled and those effects are considered

in the equivalent acoustic density and the bulk modulus, respectively. For the time-harmonic convention considered in the thesis, $e^{j\omega t}$, it can be seen that the results follow the condition for the passive media with losses, $\text{Im}(\rho_{eq}) < 0$ and $\text{Im}(\kappa_{eq}) > 0$ [36]. When opposite sign of time-harmonic convention $e^{-j\omega t}$ is used, the signs of the imaginary parts of the material properties become opposite.

2.4 Acoustic waves in rigid-framed porous media

Acoustic porous materials [35] are widely used for passive noise control for their low weight and effectiveness. In the porous materials, the acoustic waves propagate in a network of interconnected pores and the acoustic energy is converted into heat due to the viscous boundary layer effects and thermal conduction. Because of their complicated microscopic topologies, the characterization and modeling of the porous materials are not easy. However, to predict the noise reduction performance of the porous material, the knowledge of their static/dynamic material properties are required.

In the porous media, wave propagations in both fluid and solid phases exist. The waves in such porous materials can be represented by Biot's model [37]. Then the porous media have three wave components; two compressional waves and shear wave. When elastic deformation of the frame of the porous materials negligible, the

wave propagations in the porous materials can be represented as in an equivalent fluid. Then, the wave equation for the acoustic waves inside the porous material follows the Helmholtz equation with changed material or wave properties.

The wave-based models of the rigid-framed porous materials have been developed for several decades. They can be classified into two categories; empirical models and theoretical models. The empirical models [38]–[42] proposed empirical expressions for the complex wavenumber and characteristic impedance of porous materials using a large number of measurement data. The theoretical models [43]–[46] are developed considering wave propagations in various and complicated pore morphologies. Among the numerous models to represent the waves in the porous material, the Johnson-Champoux-Allard model [44], [45] and the relevant parameters to represent the model will be presented in the thesis.

The Johnson-Champoux-Allard model is a semi-phenomenological model based on the two works by Johnson *et. al.* [44] and Champoux and Allard [45] proposed to describe the complex dynamic density and bulk modulus of rigid-framed acoustic porous materials with arbitrary pore shapes. The equivalent acoustic model derived in section 2.3 can be regarded as a type of porous material with straight pores. As such model, Johnson *et al.* derived an equation for the equivalent acoustic density considering visco-inertial effects in the porous media. Because the morphologies of pores are much more complicated than the configuration considered in section 2.3,

the equivalent models have complicated equations dependent on various parameters of the porous material. The equation is given by

$$\rho = \frac{\alpha_\infty \rho_0}{\phi} \left[1 + \frac{\eta \phi}{j \omega \rho_0 \alpha_\infty} \sqrt{1 + \frac{4 j \omega \alpha_\infty^2 \mu \rho_0}{\sigma^2 \lambda_v^2 \phi^2}} \right], \quad (2.55)$$

Based on the work of Johnson *et al.*, Champoux and Allard presented an equation for the equivalent bulk modulus of the porous media that contains the thermal dissipative effects as

$$\kappa = \frac{\gamma P_0}{\phi} \left[\gamma - (\gamma - 1) \left(1 + \frac{8 \mu}{j \omega \lambda_t^2 \text{Pr} \rho_0} \sqrt{1 + \frac{j \omega \lambda_t^2 \text{Pr} \rho_0}{16 \mu}} \right)^{-1} \right]^{-1}. \quad (2.56)$$

The equivalent density and bulk modulus are frequency dependent because they were derived based on the consideration of the dynamic wave behavior in the porous materials. To calculate the equivalent density and bulk modulus of the Johnson-Champoux-Allard model, 5 parameters of the porous material are needed. The parameters are open porosity ϕ , the static air flow resistivity σ , the tortuosity α_∞ , the viscous characteristic length λ_v , and the thermal characteristic length λ_t . Brief explanations of the parameters and characterization methods of them are presented below.

Open porosity ϕ

The open porosity is the ratio of the fluid volume occupied by the continuous fluid phase to the total volume of the porous material. The open porosity can be obtained by measuring volumes and pressure differences when the volume of an enclosure where the porous material is placed is reduced [47], [48].

Static air flow resistivity σ

The static air flow resistivity is defined as the specific flow resistance per unit thickness. As the flow resistance is defined by the ratio of the pressure difference across a sample of the material to the normal flow velocity through the material, the flow resistivity can be obtained by measuring pressure difference under a steady flow [49], [50].

Tortuosity α_∞

In the porous materials, the pores with various shapes and cross sections are connected randomly, therefore the particle velocity at a microscopic level in the pores deviates from the average particle velocity at a macroscopic scale. This leads to the change of effective density of the fluid, $\rho = \alpha_\infty \rho_0$, where the tortuosity is defined as

$$\alpha_\infty = \left(\frac{1}{V} \int_V |\vec{v}|^2 dV \right) / \left(\frac{1}{V} \int_V \vec{v} dV \right)^2. \quad (2.57)$$

In above equation, V means the elementary volume of the porous material and \bar{v} is the particle velocity. The tortuosity has a value larger than one so that the phase velocity of the acoustic waves in the porous media is lower than the velocity in the air due to the so-called tortuosity effect.

Viscous characteristic length λ_v

The viscous characteristic length characterizes the viscous interaction between the oscillating air and the pore walls for a material with pores with various sections [51].

The definition is given using the integral of the square value of the microscopic velocity in a inviscid liquid in pores v by

$$\frac{2}{\lambda_v} = \frac{\int_S v^2 dS}{\int_V v^2 dV}, \quad (2.58)$$

where the integral in the numerator is over the walls of the pore-grain interface and that in the denominator is over the pore volume.

Thermal characteristic length λ_t

The thermal characteristic length was introduced to describe the high-frequency behavior of the bulk modulus influenced by thermal effects of the acoustic medium [45]. The parameter is given by

$$\frac{2}{\lambda_t} = \frac{\int_S dS}{\int_V dV} = \frac{S}{V}, \quad (2.59)$$

similar to the definition of the viscous characteristic length without weighting by the squared velocity.

Figure 2.5 shows the equivalent density and bulk modulus of three porous materials, porous material A, B, and C, obtained by the Johnson-Champoux-Allard model given in Eqs. (2.31) and (2.32) normalized to the density and bulk modulus of free air. The parameters of each porous material are shown in Table 2.2. For the material properties of the air, the values in Table 2.1 are used. Given the equivalent density and bulk modulus, the sound velocity in the porous medium can be directly calculated by the relation $c = \sqrt{\kappa/\rho}$. The velocity in the porous material is shown in Fig. 2.6 normalized to the sound velocity in free air. Due to the dissipative mechanism of the porous medium, the velocity also is frequency dependent and

Table 2.2 The characterization parameters of the porous materials [52]–[54].

	Porosity	Flow resistivity	Tortuosity	Viscous characteristic length	Thermal characteristic length
	ϕ	σ [N · s/m ⁴]	α_∞	λ_v [μ m]	λ_t [μ m]
Porous material A	0.95	8900	1.42	180	360
Porous material B	0.96	2843	1.07	273	672
Porous material C	0.97	28500	1.03	56	85

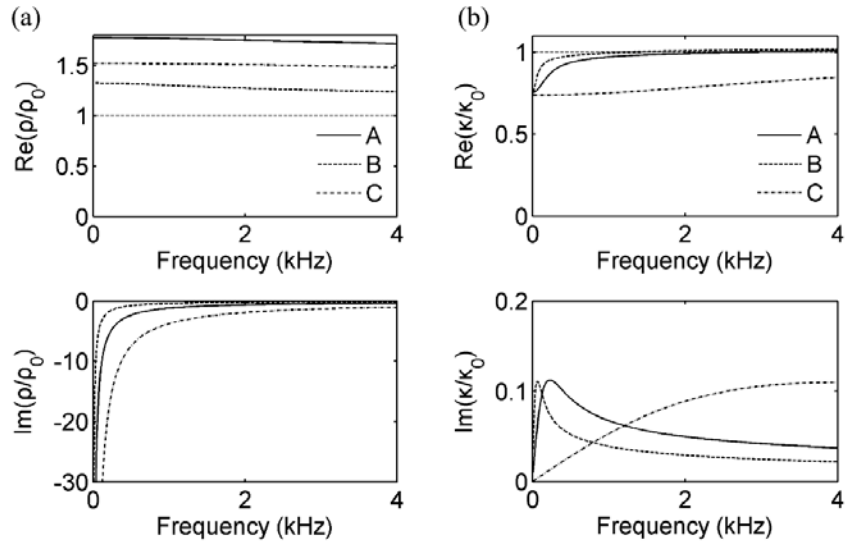


Fig. 2.5 The real and imaginary parts of (a) the equivalent density and (b) the equivalent bulk modulus of the porous materials A, B, and C of Table 2.2.

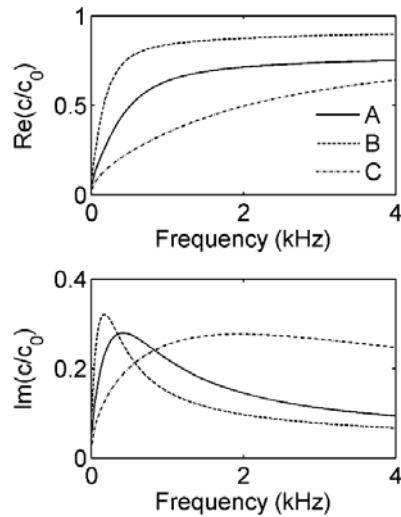


Fig. 2.6 The real and imaginary parts of the equivalent sound velocity of the porous materials A, B, and C of Table 2.2.

complex value. It can be observable that the real part value of the velocity is smaller than that of the velocity in air due to the tortuosity effect, as mentioned before.

2.5 Reflection and transmission of acoustic layers

In this section, a description method to evaluate the reflection and transmission of acoustic layers will be presented. The acoustic layers considered in the thesis can be comprised of single or multiple medium. When an acoustic wave travelling in one medium encounters the boundary of a second medium, reflected and transmitted waves are generated. To measure the quantities, the transfer matrix method will be presented.

2.5.1 Transfer matrix modelling

The transfer matrix approach (also called transmission matrix or four-pole parameter representation) is a very powerful method to evaluate transmitted, reflected waves of multilayers, acoustic ducts and mufflers, etc [35], [55]–[57]. The transfer matrix is made by considering continuity relations of acoustic pressure and volume velocity under an assumption of plane wave propagation. Consider the situation shown in Fig. 2.7 that a plane acoustic wave impinges upon the i^{th} layer of thickness h_i at an incidence angle θ_{i+1} from the $(i+1)^{\text{th}}$ layer. At the boundary of the layers, the waves

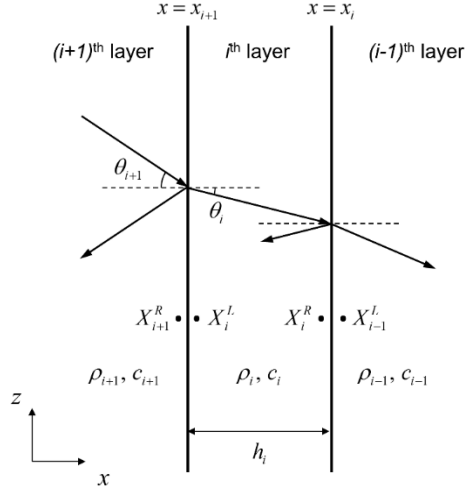


Fig. 2.7 The schematic configuration to derive the transfer matrix for the acoustic layer of finite thickness h_i .

should meet the Snell's law, $k_{i+1} \sin \theta_{i+1} = k_i \sin \theta_i$, where k_{i+1} and k_i are the wavenumber in the $(i+1)^{\text{th}}$ and i^{th} layer, respectively. The acoustic density and the sound velocity in the acoustic medium filling the i^{th} layer are given as ρ_i and c_i .

Then with the x directional propagation component $k_{ix} (= k_i \cos \theta_i)$, the pressure and the x component of the velocity fields in the layer are given by

$$p(x) = A_1 e^{-jk_{ix}x} + A_2 e^{jk_{ix}x}, \quad (2.60)$$

$$v_x(x) = \frac{\cos \theta_i}{\rho_i c_i} \left[A_1 e^{-jk_{ix}x} - A_2 e^{jk_{ix}x} \right], \quad (2.61)$$

where A_1 and A_2 are amplitudes of the acoustic waves propagating along to the $-x$ and $+x$ direction, respectively. By the pressure and volume velocity continuity conditions at the boundaries of the layers, the pressure and the particle velocity at the right-hand side of the $(i+1)^{\text{th}}$ layer, at X_{i+1}^R , and those at the left-hand side of the i^{th} layer, at X_i^L are the same. It is also the same for the boundaries of the i^{th} layer and $(i-1)^{\text{th}}$ layer, at X_i^R and X_{i-1}^L . Therefore, the pressure and the particle velocity at the boundaries are represented at the exact boundary at $x = x_{i+1}$ and $x = x_i$.

At $x = x_i$, Eqs. (2.60) and (2.61) becomes

$$p(x_i) = A_1 e^{-jk_{ix}x_i} + A_2 e^{jk_{ix}x_i}, \quad (2.62)$$

$$v_x(x_i) = \frac{\cos\theta_i}{\rho_i c_i} \left[A_1 e^{-jk_{ix}x_i} - A_2 e^{jk_{ix}x_i} \right]. \quad (2.63)$$

At $x = x_{i+1} = x_i - h_i$,

$$p(x_{i+1}) = A_1 e^{-jk_{ix}(x_i - h_i)} + A_2 e^{jk_{ix}(x_i - h_i)}, \quad (2.64)$$

$$v_x(x_{i+1}) = \frac{\cos\theta_i}{\rho_i c_i} \left[A_1 e^{-jk_{ix}(x_i - h_i)} - A_2 e^{jk_{ix}(x_i - h_i)} \right]. \quad (2.65)$$

Then the relation between the pressure and velocity fields at $x = x_i$ and $x = x_{i+1}$

can be represented by a matrix relation as

$$\begin{pmatrix} p \\ v_x \end{pmatrix}_{x_{i+1}} = \begin{bmatrix} \cos(k_{ix}h_i) & j \frac{\rho_i c_i}{\cos \theta_i} \sin(k_{ix}h_i) \\ j \frac{\cos \theta_i}{\rho_i c_i} \sin(k_{ix}h_i) & \cos(k_{ix}h_i) \end{bmatrix} \begin{pmatrix} p \\ v_x \end{pmatrix}_{x_i} = \mathbf{T}_i \begin{pmatrix} p \\ v_x \end{pmatrix}_{x_i}. \quad (2.66)$$

The 2x2 matrix in Eq. (2.66) connecting the vector composed of the pressure and the velocity fields at the other side of the boundaries of the layer is the transfer matrix \mathbf{T}_i . Equation (2.66) is a recursive equation from which the pressure and velocity of any layer can be determined from boundary and incident sound wave conditions.

2.5.2 Calculation of reflection and transmission coefficients

Figure 2.8 shows a multilayer consisting of N acoustic layers under plane wave incidence at incidence angle θ_i . The acoustic pressure and velocity in the incident medium, fluid (I), are represented as

$$p_I = Ae^{-jk_{Ix}x} + Re^{jk_{Ix}x}, \quad (2.67)$$

$$v_{Ix} = \frac{\cos \theta_i}{\rho_I c_I} (Ae^{-jk_{Ix}x} - Re^{jk_{Ix}x}), \quad (2.68)$$

where A and R are the amplitudes of the incident and reflected waves, respectively. For simplification, A is set to be 1. And the wave fields in the transmitted medium, fluid (F), are described as

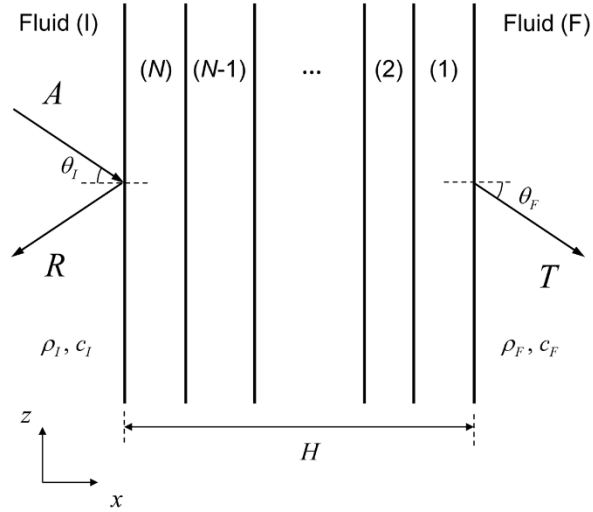


Fig. 2.8 The multilayer of N acoustic layers under plane wave incidence.

$$p_F = T e^{-jk_{Fx}x}, \quad (2.69)$$

$$v_{Fx} = \frac{\cos \theta_F}{\rho_F c_F} T e^{-jk_{Fx}x}, \quad (2.70)$$

where T is the amplitude of the transmitted wave.

For a multilayer of acoustic media, the total transfer matrix can be constructed by connecting the transfer matrix of the i^{th} layer given by Eq. (2.66). Then the transfer matrix modelling for the acoustic pressure and particle velocity in the fluid (I) and (F) is expressed as

$$\begin{pmatrix} p \\ v_x \end{pmatrix}_I = \mathbf{T}_{total} \begin{pmatrix} p \\ v_x \end{pmatrix}_F = \mathbf{T}_n \mathbf{T}_{n-1} \cdots \mathbf{T}_1 \begin{pmatrix} p \\ v_x \end{pmatrix}_F. \quad (2.71)$$

Then the transmission and reflection coefficients can be calculated as below,

$$T = \frac{2e^{-jk_F H}}{T_{11} + \frac{\cos \theta_F}{\rho_F c_F} T_{12} + \frac{\rho_I c_I}{\cos \theta_I} T_{21} + \frac{\rho_I c_I \cos \theta_F}{\cos \theta_I \rho_F c_F} T_{22}}, \quad (2.72)$$

$$R = \rho_I c_I \frac{T_{11} + \frac{\cos \theta_F}{\rho_F c_F} T_{12} - T_{21} - \frac{\cos \theta_F}{\rho_F c_F} T_{22}}{\frac{\cos \theta_I}{\rho_I c_I} T_{11} + \frac{\cos \theta_I}{\rho_I c_I} \frac{\cos \theta_F}{\rho_F c_F} T_{12} + T_{21} + \frac{\cos \theta_F}{\rho_F c_F} T_{22}}, \quad (2.73)$$

where T_{pq} means the (p, q) component of the total transfer matrix \mathbf{T}_{total} and H is the total thickness of the multilayer.

When the multilayer is backed by a hard wall, i.e., the fluid (F) is an acoustically-rigid material so that the acoustic waves cannot propagate into, the velocity in the particle velocity in the transmitted medium should be vanished. By applying this condition, the reflection coefficient can be obtained as

$$R_{rigid} = \frac{\frac{T_{11}}{T_{21}} - \frac{\rho_I c_I}{\cos \theta_I}}{\frac{T_{11}}{T_{21}} + \frac{\rho_I c_I}{\cos \theta_I}}. \quad (2.74)$$

In the hard-backed condition, the fraction T_{11}/T_{21} represents the impedance at the surface of the multilayer, p_I/v_{Ix} , called *surface impedance*. By using the symbol Z_N for the surface impedance of the total system and z_I for the characteristic impedance of the medium fluid (I), the reflection coefficient of Eq. (2.72) can be rewritten as

$$R_{rigid} = \frac{Z_N - \frac{z_I}{\cos \theta_I}}{Z_N + \frac{z_I}{\cos \theta_I}}. \quad (2.75)$$

When only one layer placed on the hard wall is considered, the surface impedance of the layer becomes

$$Z_i = -j \frac{\rho_i c_i}{\cos \theta_i} \cot(k_{ix} h_i). \quad (2.76)$$

The surface impedance on the i^{th} layer can be represented as a successive relation as

$$Z_i = z_i \frac{Z_{i-1} + j z_i \tan(k_{ix} h_i)}{j Z_{i-1} \tan(k_{ix} h_i) + z_i} \quad (i = 2, 3, \dots, N). \quad (2.77)$$

After the reflection and transmission coefficients are obtained, the absorption coefficients α and the transmission loss TL are calculated by the relation

$$\alpha = 1 - |R|^2 - |T|^2, \quad (2.78)$$

$$TL = -20 \log_{10} |T|. \quad (2.79)$$

When the layer is terminated with a hard backing, the absorption coefficient is calculated as $\alpha = 1 - |R|^2$.

CHAPTER 3.

ACOUSTIC METAMATERIALS INVOLVING POROUS MEDIA FOR BROADBAND SOUND ABSORPTION

3.1 Chapter overview

Even though there have been numerous works on sound absorption performance of the acoustic metamaterials, the broadband acoustic performance of them is still a challenging issue. Because the acoustic metamaterials presented so far mostly rely on the resonance phenomena for selective frequencies of the non-dissipative medium, the frequency range of their acoustic performance is inevitably narrow. The difficulty of achieving broadband performance may lie on the realization of an absorbing structure with a constant characteristic for a high absorption in a wide range of frequency.

Acoustic porous materials [35], widely used to dissipate sound energy, are known to have effective sound absorption performances in the broad bandwidth. However, the efficiency of these materials with regard to sound absorption is strongly dependent on the frequencies of interest. Because the absorption of long-wavelength sound waves requires sufficiently thick porous layers, thin porous layers are used to absorb sound waves mainly in high frequency ranges. When the thickness of a layer is constrained to be less than the order of the wavelength of incident sound waves, efficient low-frequency sound absorption as well as broadband sound absorption can be quite demanding for a homogenous porous material.

To deal with the thickness constraint on the sound absorption performance, several attempts, such as optimal multi-layering and porous foam shaping, have been made [58]–[60]. In those works, the researchers attempted to overcome the thickness constraint by finding optimal distributions of the porous materials. The optimization-based design problems were solved within a constrained design domain according to the frequency of interest. More recently, porous materials combined with artificially engineered structures were studied in an effort to enhance their acoustic performance in the concepts of sonic crystals and acoustic metamaterials [13], [32], [61]–[65]. Among these efforts, the effects of circular inclusions [61], [62] resonant slotted inclusions [32] in a hard-backed porous layer were investigated to enhance the sound absorption performance. Periodic arrangements of porous slabs were also tested for broadband sound absorption [13], [63]. Although these earlier studies have made

some progress on improving the sound absorption characteristics, it remains difficult to overcome the thickness constraint in an installed porous layer to broaden the overall sound absorption performance.

Under such circumstances, this chapter presents acoustic metamaterials designed by incorporating porous materials involving dissipative loss of acoustic media. The designed metamaterials show that the high sound absorption performances are achievable in a broad range of frequency not only by complex multiple resonance modes but also by the dissipative loss of the porous materials. In the following sections, the sound absorption mechanism of a homogeneous, finite-thickness porous layer will be studied first. Based on the observation, the two acoustic metamaterials will be presented whose broadband sound absorption performance is realized by so-called ‘tuned thickness resonances’ and ‘multiple slow waves’ in section 3.3 and 3.4, respectively. The physical mechanism and relevant phenomena will be thoroughly investigated.

3.2 Sound absorption of a porous layer

In this section, we investigate the sound absorption performance and related physical mechanisms of a porous layer. Figure 3.1(a) shows a configuration of a porous layer which has a finite thickness H placed on a hard wall surrounded by air. The porous

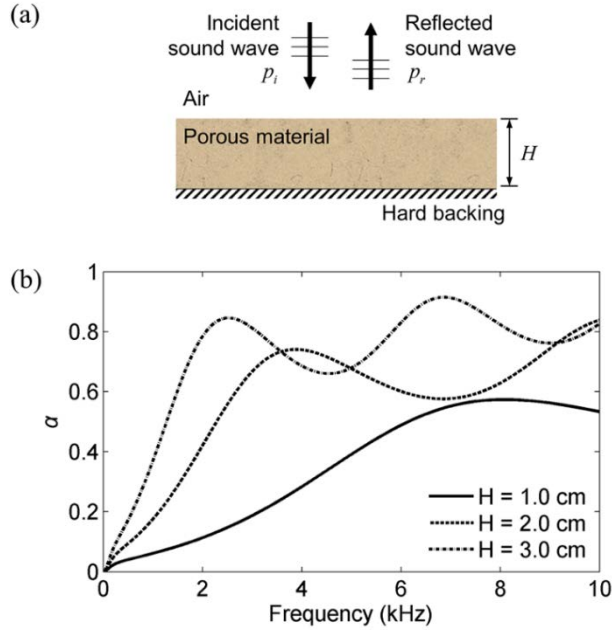


Fig. 3.1 (a) A porous layer of thickness H placed on a hard wall under normal sound wave incidence. (b) Sound absorption coefficient of porous layers of various thicknesses.

material under consideration in the thesis is assumed to have a motionless frame. Hence, the wave motion in the porous materials can be represented as that in an equivalent fluid, which is defined by the complex-valued effective mass density ρ_1 and bulk modulus κ_1 . In this work, the Johnson-Champoux-Allard model presented in section 2.4 is employed to represent the effective parameters of the rigid porous materials. The acoustic density and the sound velocity in the air are ρ_0 and c_0 , respectively. Following the description of Eqs. (2.75) and (2.76) in section 2.5, the reflection coefficient R of a porous layer placed on the hard wall under normal

incidence is obtained as

$$R = \frac{Z - z_0}{Z + z_0}, \quad (3.1)$$

where Z and z_0 are the surface impedance of the porous layer and the characteristic impedance of the air, respectively, and those values are obtained as $Z = -j\rho_1 c_1 \cot(k_1 H)$ and $z_0 = \rho_0 c_0$ with the wavenumber in the porous medium, $k_1 (= \omega/c_1)$. Then the absorption coefficient becomes

$$\alpha = 1 - |R|^2. \quad (3.2)$$

By investigating the impedance relation of the porous layer and the air, it is possible to draw some qualitative conclusions on the sound absorption performance of the porous layer. When the denominator and the numerator of Eq. (3.1) are divided by z_0 , it can be given as

$$R = \frac{z_s - 1}{z_s + 1}, \quad (3.3)$$

where z_s means the specific acoustic impedance ($Z/\rho_0 c_0$). The specific acoustic impedance can be separated into the real and imaginary parts as

$$z_s = \text{Re}(z_s) + j \text{Im}(z_s). \quad (3.4)$$

Physically, the real and imaginary parts of the impedance mean the resistive and

reactance parts, respectively. By combining Eqs. (3.3), (3.4) and (3.2), the absorption coefficient is obtained by

$$\alpha = \frac{4\text{Re}(z_s)}{\{1 + \text{Re}(z_s)\}^2 + \{\text{Im}(z_s)\}^2} . \quad (3.5)$$

Eq. (3.5) implies that the total absorption can be achieved when $\text{Im}(z_s)$ becomes 0 and $\text{Re}(z_s)$ becomes 1. It means the impedance matching with the air ($\text{Re}(z_s) = 1$) at the resonance state ($\text{Im}(z_s) = 0$) [66].

Figure 3.1(b) shows the absorption coefficients for several thicknesses $H = 1.0$ cm, 2.0 cm, and 3.0 cm of the porous layer. The material properties of the air are given in Table 2.1 and characterization parameters of the porous material A in Table 2.2 are used for calculation. The sound absorption performance of a porous layer is strongly dependent on its thickness. For a layer of very thin thickness compared to the wavelength, $k_1 H \ll 1$, the surface impedance of the porous layer can be replaced with $1/k_1 H$. Then the surface impedance has a very large impedance, which means a large impedance mismatch with the air. Therefore, it leads to a low sound absorption. In other words, the high sound absorption of a porous layer is not easily achieved in a low frequency range.

In the mid-frequency range, the surface impedance is governed by the periodicity of the cotangent function. It is observable that the absorption curves have peaks for a

fixed thickness that come from the resonance states of the porous layer. Suppose that the porous layer is lossless, material properties of the medium only have real parts. Then the surface impedance becomes pure imaginary, which means only reactive, and it becomes zero when

$$k_1 H = (2n - 1) \cdot \frac{\pi}{2}, \quad (3.6)$$

where n is an integer. If expressed in terms of the wavelength in the porous medium, λ_1 , above equation becomes

$$H = (2n - 1) \cdot \frac{\lambda_1}{4}. \quad (3.7)$$

As the above condition for the resonance is related to the thickness of the layer, it is named as *thickness resonances* in the thesis. Note that the porous medium has complex equivalent material properties, the resonance frequencies can be shifted from the exact thickness resonance condition. At the thickness resonances, the particle velocities in the porous layer are zero in the bottom of the layer (hard wall) and maximum at the top of the layer. At the resonance state, the absorption coefficient is determined by the resistive part of the surface impedance and the characteristic impedance of the air, as mentioned before. Because the real parts of the surface impedance are different for the defined thicknesses, the peak values at the thickness resonances are obtained as different values. It is also noticeable in the graph that the absorption curves have trough between the successive thickness resonances due to the anti-resonances. At the resonance states, the particle velocities

are minimum at the top and the bottom of the layer, and maximum in the plane of the layer. However, energy losses can take place only if the air is moving in the pores of the layer [67], therefore, the location where the maximum particle velocity exists would be very crucial for the sound absorption.

3.3 Metaporous layer with tuned thickness resonances

This section shows that if rigid partitions that are impervious to sound waves are periodically and appropriately embedded in a hard-backed porous layer, the thickness constraint can be overcome to some extent. In addition to the improvement in the low-frequency range, the sound absorption capability in the overall frequency range of interest can be substantially improved even under a given layer thickness constraint if the configuration of the partitioned porous material units is engineered according to the method to be developed in this study.

3.3.1 Design of the metaporous layer with tuned thickness resonances

To give an idea of how much the sound absorption can be improved, we present the results of our investigation in Fig. 3.2. In this figure, a porous layer with periodically embedded rigid partitions, referred to here as a metaporous layer, can be considered

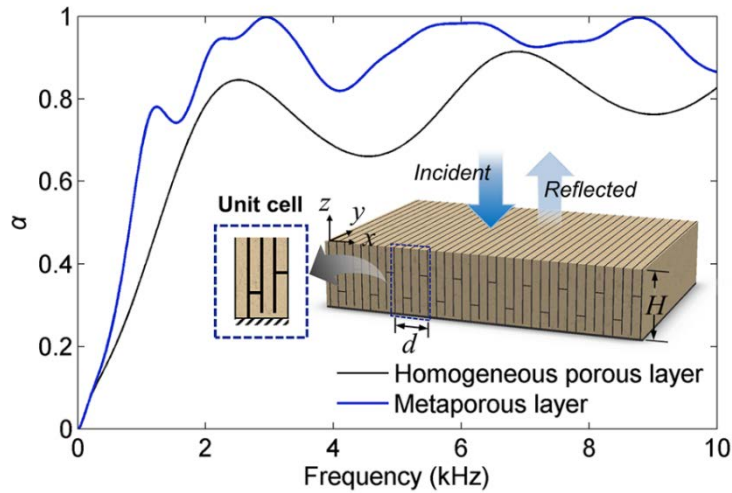


Fig. 3.2 Enhancement of sound absorption performance of metaporous layer shown in the inset, compared to that of a homogeneous porous layer with the same thickness. ($H = 3.0$ cm and $d = 1.6$ cm)

as a hard-backed porous system consisting of unit cells. The unit cell is constructed in a homogeneous porous layer with several rigid partitions (black in color), which are vertical or horizontal to the x -axis, where the sound waves are assumed to impinge upon the layer along the z -direction. In the unit cell in the inset of Fig. 3.2, while some vertical partitions are attached to the hard wall directly, two narrow gaps from the bottom are designed so as to connect neighboring porous slabs. As a result of these treatments, the present metaporous layer exhibits greatly enhanced sound absorption performance over a wide range of frequencies, as shown in Fig. 3.2, compared to a homogeneous porous layer with the same total thickness without any partitioning treatment. The physics related to the proposed metaporous layer

structure will be revealed in this study.

Our approach to overcome the thickness constraint for broadband sound absorption is to use the proposed metaporous layers realized by unique treatments in a homogenous porous layer. Compared with the homogeneous porous layer, no thickness increase will be considered throughout the present investigation. The proposed treatments include (i) the vertical and horizontal partitioning of a porous layer with acoustically impervious rigid partitions, (ii) opening narrow gaps around the hard wall between neighboring porous slabs, and (iii) building multiple porous slabs with different thicknesses. To analyze the corresponding physical mechanisms in sound absorption based on the effective medium approach [68], theoretical models are derived and utilized. The theoretical models are validated by comparing their predictions of the sound absorption performance with those by the finite element method (FEM) using COMSOL Multiphysics 4.3 [69]. In the finite element modeling, Floquet-Bloch periodic boundary conditions are imposed on the left- and right-hand sides of the unit cell in order to express the infinitely periodic arrangement of the unit cell in the proposed layers. In addition, the rigid partitions are represented with a hard-wall boundary condition.

Compared with the original homogeneous porous layer, the metaporous layers are structured by unit cells containing three unique features, i.e., a periodic arrangement of vertical partitions, a gap between the partition and the hard wall, and multiple

porous slabs of different thicknesses. In order to explain the effect of each feature, differently configured, periodically partitioned porous layers will be considered in the following sections. All of the layers considered in this work are assumed to be infinitely long in the y -direction such that the wave problem under consideration can be considered as a two-dimensional problem in the xz -plane. In addition, they are open to an infinite air region, in which the density and the bulk modulus are respectively ρ_0 and κ_0 . The equivalent mass density ρ_1 and bulk modulus κ_1 of the porous medium are obtained by the Johnson-Champoux-Allard model presented in section 2.4, Eqs. (2.55) and (2.56). If the density and bulk modulus of each medium are given, it becomes possible to determine the sound velocity $c_i = \sqrt{\kappa_i/\rho_i}$, the wave number $k_i = \omega/c_i$ and the characteristic impedance $z_i = \rho_i c_i$ of air ($i = 0$) and the porous media ($i = 1$) immediately. The material parameters of air and porous material used in this work can be found in Table 2.1 and Table 2.2, porous material A.

The layers under consideration are also assumed to have subwavelength periodicity within the frequency range of interest. Accordingly, they can be represented as effective layers, characterized by the effective characteristic impedance (z_e) and the effective surface impedance (Z_e). This assumption is equivalent to using a one-dimensional wave model in a layer filled with a homogeneous medium. The effective

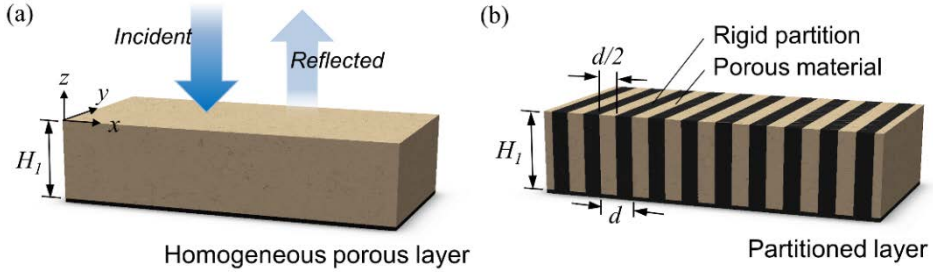


Fig. 3.3 Configurations of (a) an un-partitioned homogeneous porous layer and (b) periodically partitioned porous layers with the same thickness H_1 .

impedances z_e and Z_e can be determined if several effective parameters of an effective medium, such as the density ρ_e , the bulk modulus κ_e , the wave speed $c_e = \sqrt{\kappa_e/\rho_e}$, the wave number $k_e = \omega/c_e$, are known.

3.3.2 Influence of periodic vertical rigid partitions

Consider a homogeneous porous layer and a partitioned porous layer on a hard wall, as shown in Figs. 3.3(a) and (b). In the latter case, the porous slab and the rigid partition are equally spaced, and the unit cell is then infinitely repeated in a subwavelength period of d along the x -direction. The period d is set to be smaller than half of the minimum wavelength in the frequency range of interest, i.e., $d < \lambda_{\min}/2$, which is a general criteria to model the metamaterials as an effective homogeneous medium of effective material properties defined by the relation of the properties of constituting media. For normally incident sound waves along the z -

direction, the homogeneous layer (superscripted with h) of thickness H_1 has its sound absorption peaks at the thickness resonance frequencies ($P_1^h(H_1)$ and $P_2^h(H_1)$ in Fig. 3.4(a)). At these frequencies, odd multiples of the quarter wavelength of the incident sound wave are coincident with the layer's thickness. For the partitioned porous layer, each unit cell acts as a locally reacting layer. This can be observed in Fig. 3.4(a), which shows that the periodic arrangement of the vertical partitions increases the sound absorption coefficients substantially at the peak frequencies ($P_1(H_1)$ and $P_2(H_1)$) compared to those of the homogeneous layer. On the other hand, it lowers the absorption coefficients at intermediate frequencies between the successive thickness resonances.

The phenomenon observed for the partitioned porous layer arises from the change in the surface impedance of the layer upon the periodic insertion of rigid partitions. For an analytical investigation of this phenomenon, the effective medium approach, which represents the partitioned layer as an anisotropic homogeneous effective layer, is employed. The volume fraction of the porous material in the unit cell is set to η ($0 < \eta \leq 1$); the state of $\eta = 1$ corresponds to a homogeneous porous layer. The x - and z -directional effective densities and the effective bulk modulus of the effective medium are given by [68]

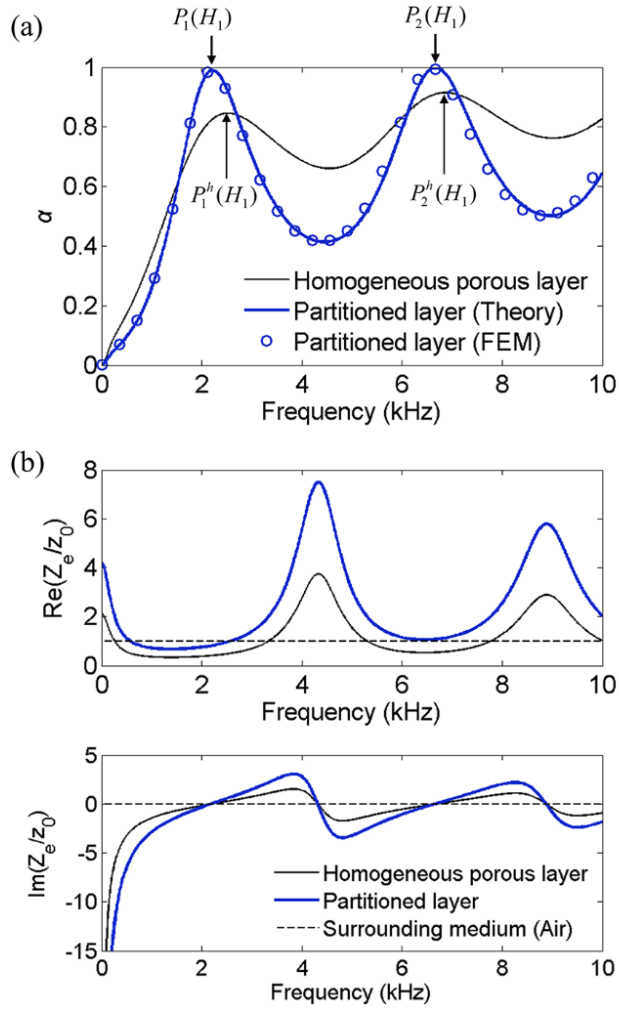


Fig. 3.4 (a) The sound absorption coefficients of the two layers in Fig. 3.3 under normal sound wave incidence along the z direction. (b) The real and imaginary parts of the surface impedances of the two layers and the characteristic impedance of the surrounding air. All the impedance values are normalized by the characteristic impedance of air (z_0). For the plots, the values of $H_1 = 3.0$ cm and $d = 1.0$ cm were used.

$$\rho_{e,x} = \eta\rho_1 + (1-\eta)\rho_2, \quad (3.8)$$

$$\rho_{e,z}^{-1} = \eta\rho_1^{-1} + (1-\eta)\rho_2^{-1}, \quad (3.9)$$

$$\kappa_e^{-1} = \eta\kappa_1^{-1} + (1-\eta)\kappa_2^{-1}, \quad (3.10)$$

where the subscript e indicates the effective quantities. In addition, ρ_2 and κ_2 denote the density and the bulk modulus, respectively, of the rigid material. Considering that ρ_2 and κ_2 can be set to infinite values, the effective material parameters in Eq. (3.9)-(3.10) can be written as $\rho_{e,x} = \infty$, $\rho_{e,z} = \rho_1/\eta$ and $\kappa_e = \kappa_1/\eta$. According to their definitions, the effective sound velocity and characteristic impedance of the layer along the wave propagating z direction become $c_{e,z} = \sqrt{\kappa_e/\rho_{e,z}} = c_1$ and $z_e = \rho_{e,z}c_{e,z} = \rho_1c_1/\eta$, respectively. Then, the effective surface impedance Z_e of the partitioned porous layer can be given by

$$Z_e = -jz_e \cot(k_e H_1) = -j \frac{\rho_1 c_1}{\eta} \cot(k_1 H_1). \quad (3.11)$$

In Eq. (3.12), k_e and k_1 denote the wavenumbers in the present effective medium and in the original bulk porous material, respectively. Note that the effective characteristic impedance (z_e) and the effective surface impedance (Z_e) of the metaporous layer increase with regard to those of the homogeneous porous layer as a multiple of $1/\eta$, while the effective sound velocity ($c_{e,z}$) remains the same. With

the effective surface impedance in Eq. (3.11), the reflection coefficient $r(\omega) = [Z_e(\omega) - z_0] / [Z_e(\omega) + z_0]$ and the sound absorption coefficient $\alpha(\omega) = 1 - |r(\omega)|^2$ of the effective layer can be calculated.

For the partitioned porous layer, the absorption coefficients calculated from the derived theoretical formulation (blue line) are compared to those through the finite element modeling (blue circles) in Fig. 3.4(a). The good agreement between them is evidence of the effectiveness of the derived theoretical models of the partitioned porous layer in Fig. 3.3(b) in the context of metamaterials in the considered frequency range. The real and imaginary parts of the surface impedance of the partitioned porous layer are plotted in Fig. 3.4(b) together with those of the homogeneous porous layer. As shown in Eq. (3.11), the main parameter which changes the surface impedance is the effective density of the medium in the wave-propagation direction. In other words, the insertion of the periodic rigid partitions increases the density of the effective medium by a factor of $1/\eta$, which results in an increase of the effective surface impedance. For the partitioned porous layer shown in Fig. 3.3(b), the effective surface impedances increase to twice that of the homogeneous porous one.

It is conceivable that the insertion of the rigid vertical partitions would only worsen the absorption performance. However, it is possible to offset the impedance

mismatch between the porous medium and the surrounding air at the thickness resonances with an increase in the effective surface impedance. At the first and second thickness resonance frequencies (2190 Hz and 6670 Hz, respectively) of the partitioned porous layer, the surface impedances approach the characteristic impedance of air, as shown in Fig. 3.4(b), resulting in an enhancement of the sound absorption characteristics. In contrast, the real and imaginary parts of the surface impedances diverge more from the value of the characteristic impedance of air at the frequencies between the successive thickness resonances; therefore, the partitioned layer has worse sound absorption performance in those frequency ranges.

3.3.3 Low frequency absorption improvement by gap insertion

The proposed metaporous layers have narrow porous gaps near the bottom, as shown in Fig. 3.2. In order to see the effect of the gap clearly, a unit cell with a simpler configuration is presented as shown in Fig. 3.5(a), which may be viewed as a special case of a unit cell of a metaporous layer. In this unit cell, a horizontal partition is located at the top of the porous slab on the right-hand side, while a gap of size a is opened near the hard wall. The gap in the metaporous layer can serve as 1) an acoustic path connecting the two porous slabs of thicknesses H_1 and h , and 2) a neck of a Helmholtz chamber. When the gap functions as a connecting path, the two porous slabs act as if they were a single porous slab with an effective thickness $H_1^e = H_1 + h$. An incident sound waves would travel through the porous slab on the

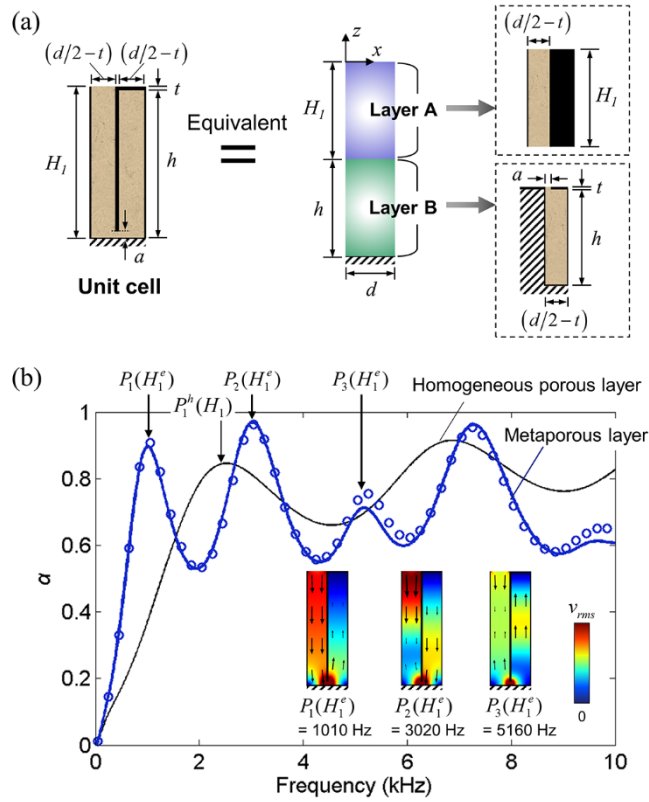


Fig. 3.5 A metaporous layer used to develop a theoretical model. (b) Comparison of the absorption coefficients of the metaporous layer (blue line: by the derived theory, circles: by finite element method) and those of the homogeneous layer (black line: by the derived theory). The color levels (varying from 0 to 0.003 m/s) in the inset denote the magnitude of the particle velocity in the unit cell at the three lowest peak frequencies. ($H_1 = 3.0$ cm, $h = 2.95$ cm, $t = 0.5$ mm, $a = 1.0$ mm and $d = 1.0$ cm)

left-hand side of a distance of H_1 , pass through the narrow gap and travel further through the porous slab on the right-hand side of a distance of h . The acoustic waves finally reach the horizontal partition and are reflected backward. When the gap is

viewed as the neck of an absorbing cavity formed by the partitions surrounding the porous slab on the right-hand side, the physics of the Helmholtz chamber may also be involved here. How these mechanisms improve the sound absorption capability of the metaporous layer will be investigated.

For quantitative analyses of the effects of the designed structures on the sound absorption characteristics, the unit cell is modelled as an acoustic system of two serially connected effective layers A and B, as illustrated in Fig. 3.5(a); Layers A and B correspond to the porous slabs on the left- and right-hand sides of the unit cell. First, Layer A can be modelled as an acoustic component consisting of a porous slab and a rigid partition in parallel, as illustrated in the dashed box in Fig. 3.5(a). Given that the width of the porous slab is $d/2 - t$, the rigid inclusion has a width of $d/2 + t$. With a definition of $\eta = (d/2 - t)/d$, the characteristic impedance of Layer A is expressed as $z_A = \rho_1 c_1 / \eta$. Secondly, Layer B in Fig. 3.5(a) represents the porous slab on the right-hand side with a gap. Because this gap can act as the neck of an acoustic chamber filled with a porous material, the acoustic mass effect of the neck as well as the effect of the slab thickness should be considered when evaluating the effective surface impedance of the hard-backed Layer B at $z = -H_1$. This can therefore be represented by the following formula, which is commonly used for a Helmholtz chamber [55]:

$$Z_B = \frac{j}{\eta} \{ \omega m - \rho_1 c_1 \cot(k_1 h) \}. \quad (3.12)$$

Here, the symbol m denotes the acoustic mass given by $m = (t + 2\delta a)\rho_1 d / 2a$ with a correction factor δ of 1.9. Because the porous slabs on the left- and right-hand sides of the unit cell have the same width in the x direction, the volume fraction η in Eq. (3.12) is identical to that used for Layer A. Using the above results, the surface impedance of the acoustic system made of serially connected Layers A and B can be written as

$$Z_{AB} = z_A \frac{Z_B \cot(k_1 H_1) + jz_A}{jZ_B + z_A \cot(k_1 H_1)}. \quad (3.13)$$

Eq. (3.13) may be expressed in detail simply by substituting the expressions of z_A and Z_B into it as follows. Finally, the effective surface impedance of the metaporous layer composed of the unit cell in Fig. 3.5(a) is found to be

$$Z_{AB} = \frac{j \frac{\omega m}{\eta} \frac{\cot(k_1 H_1)}{\cot(k_1 H_1) + \cot(k_1 h)} - j \frac{\rho_1 c_1}{\eta} \cot\{k_1 (H_1 + h)\}}{-\frac{\omega m}{\rho_1 c_1} \frac{1}{\cot(k_1 H_1) + \cot(k_1 h)} + 1}. \quad (3.14)$$

Using Eq. (3.14), the absorption coefficient of the metaporous layer of this unit cell is plotted in Fig. 3.5(b). As shown in this figure, the result from the present theoretical model is in good agreement with the result from a two-dimensional finite element model.

In Fig. 3.5(b), the first peak in the absorption coefficient appears at 1010 Hz ($P_1(H_1^e)$), which is nearly half the first peak frequency of the original un-partitioned homogeneous porous layer ($P_1^h(H_1)$). This can be explained by the elongated effective thickness $H_1^e = H_1 + h \approx 2H_1$ in the present metaporous layer; the first thickness resonance frequency in a hard-backed layer is inversely proportional to its thickness. The contour plots in the inset of Fig. 3.5(b) show the particle velocity fields at the three lowest absorption peak frequencies, which correspond to the first ($P_1(H_1^e)$), second ($P_2(H_1^e)$) and third ($P_3(H_1^e)$) thickness resonances. The velocity fields resemble those in a straight hard-backed layer of thickness H_1^e , although there are some local distortions around the gap. This result suggests that the gap between the two porous slabs acts more as an acoustic path connecting the two slabs rather than as the neck of a Helmholtz chamber. In fact, the term $\left[-j(\rho_1 c_1 / \eta) \cot \{k_1(H_1 + h)\}\right]$ in the numerator of Eq. (3.14) is predominant. This implies that the effective surface impedance is calculated from a hard-backed layer of thickness $H_1^e = H_1 + h$, which is vertically partitioned at a volume fraction of η . The Helmholtz resonance occurs at around 2300 Hz, but its influence is marginal with regard to the overall absorption coefficient. Therefore, the Helmholtz resonance peak cannot be clearly seen in the absorption curve.

Note that the insertion of a gap makes it possible to connect neighboring porous slabs, extending the effective thickness of the metaporous layer. The realization of the extended effective thickness in the present work may be compared to the space coiling-up in earlier works [70]–[73]. The acoustic path in the present metaporous layer is open to air at one end and blocked at the other end by the horizontal partition such that the thickness resonance phenomenon is utilized. The insertion of the gap is significant because this can overcome the thickness constraint of the finite porous layer in low-frequency ranges. Furthermore, the increased surface impedance of the configuration presented in Fig. 3.5(a) by the factor of $1/\eta$ considerably enhances the absorption coefficients at the thickness resonance frequencies.

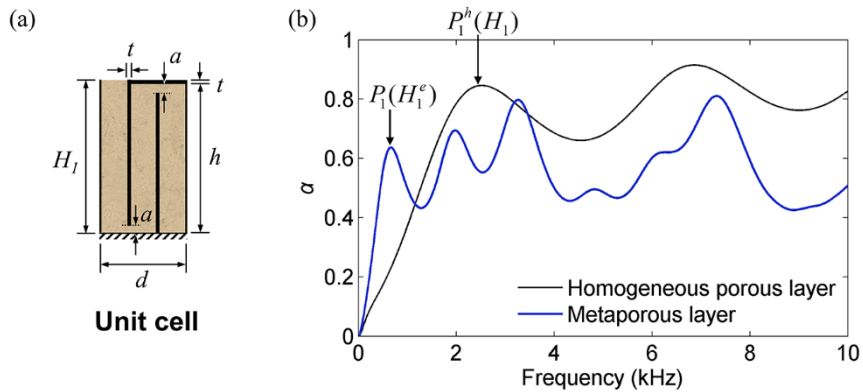


Fig. 3.6 (a) A unit cell configuration with two gaps connecting three porous slabs. (b) The sound absorption performance of a metaporous layer of the unit cell in (a) compared to that of a homogeneous porous layer. For the plots, $H_1 = 3.0$ cm, $h = 2.95$ cm, $t = 0.5$ mm, $a = 1.0$ mm and $d = 1.5$ cm are used.

The effective thickness of the layer can be further increased to $H_1+H_2+H_3$ by adding another gap. An example of the unit cell configuration is shown in Fig. 3.6(a). The first resonance frequency of the metaporous layer is decreased to 660 Hz ($P_1(H_1^e)$ in Fig. 3.6(b)), nearly 1/3 value of the first resonance frequency of a homogeneous porous layer because its effective thickness is increased to almost three times compared with the nominal thickness H_1 . However, the overall sound absorption capability of the metaporous layer becomes worse than that of the homogeneous layer because a large amount of sound waves is reflected back at the interface. Therefore, to improve the broadband sound absorption capability using the partitioning method, the rigid partitions have to be arranged appropriately.

3.3.4 Multiple thickness resonances for broadband sound absorption

In the previous sections, the vertical partitioning and gap insertion effects in a porous layer were investigated to understand the enhancement of the absorption performance at thickness resonance frequencies. On the other hand, Figs. 3.4(a) and 3.5(b) show that the absorption coefficients at intermediate frequencies between the successive thickness resonances worsen as compared to those of an un-partitioned homogeneous layer. This negative result originates from the single characteristic thickness in the partitioned porous layer (e.g., H_1 in Fig. 3.3(b) and H_1^e in Fig. 3.5(a)). To resolve this drawback, one can conjecture that if resonance peaks are additionally formed between the successive thickness resonances, the absorption

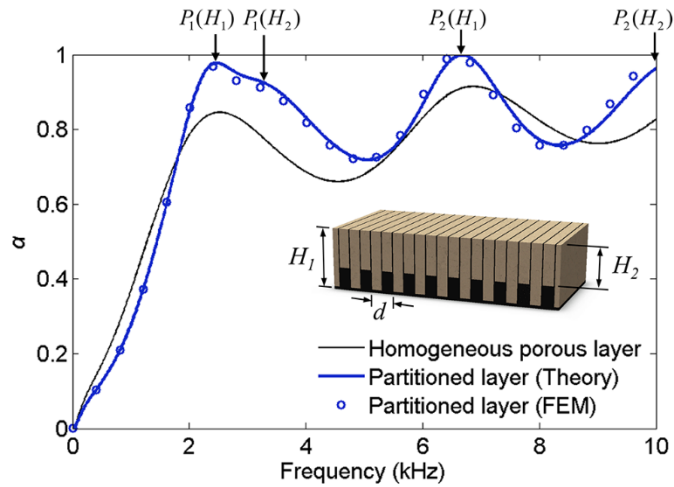


Fig. 3.7 The absorption performance of the partitioned porous layer in which the unit cell is constructed with two porous slabs with different thicknesses. It is compared with that of the original homogeneous porous layer. Solid lines denote the results by the derived theory and symbols, by the finite element analysis. ($H_1 = 3.0$ cm, $H_2 = 2.0$ cm and $d = 1.0$ cm)

performance in the frequency range would also be enhanced. Figure 3.7 shows the configuration of a partitioned porous layer and its absorption performance compared to that of a homogeneous porous layer with the same thickness. The unit cell of the partitioned layer is constructed with two porous slabs, each of which has different thicknesses H_1 and H_2 , such that two sets of thickness resonances can be developed in the layer. As indicated in Fig. 3.7 as $P_1(H_2)$ and $P_2(H_2)$, new resonance peaks arise at intermediate frequencies due to the porous slabs of thickness H_2 . Consequently, a considerable improvement in the overall sound absorption is

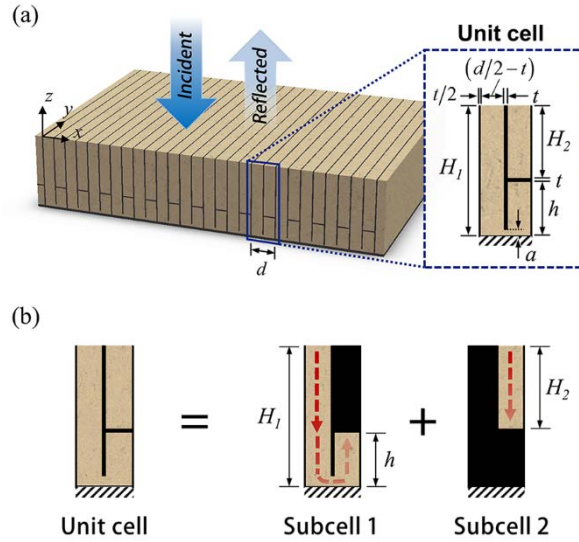


Fig. 3.8 The configuration of a metaporous layer and its unit cell made of multiple porous slabs. (b) The metaporous layer can be modelled as a parallel connection of the two independent subcells.

observed. The effect of multiple porous slabs having different thicknesses in a metaporous layer is studied with the partitioned porous layer shown in Fig. 3.8(a).

The metaporous layer resembles that shown in Fig. 3.2, but the unit cell in Fig. 3.8(a) has a simpler configuration. The unit cell can be modelled as an acoustic system connected in parallel by Subcell 1 and Subcell 2 as illustrated in the inset of Fig. 3.8(b). The region in black in each subcell indicates that it is filled with rigid materials. Then, the surface impedance of the metaporous layer becomes

$$(Z_e)^{-1} = (Z_{sc1})^{-1} + (Z_{sc2})^{-1}, \quad (3.15)$$

where the surface impedances of the layer made of Subcell 1 and Subcell 2 are denoted as Z_{sc1} and Z_{sc2} , respectively. Because Subcell 1 is constructed with two porous slabs and a gap, as shown in Fig. 3.8(a), Z_{sc1} can be obtained by Eq. (3.14) by changing the h value. Moreover, the effective surface impedance of Subcell 2 is calculated as $Z_{sc2} = -j(\rho_1 c_1 / \eta) \cot(k_1 H_2)$ from Eq. (3.11).

The sound absorption coefficients of layers made of each subcell and the unit cell are compared in Fig. 3.9(a). Lined-data are obtained from a theoretical analysis using Eq. (3.15) and symbol-data are obtained through a finite element analysis. The results show good agreement. The first peak frequencies of the Subcell 1 ($P_1(H_1^e)$) and Subcell 2 ($P_1(H_2)$) layers are lower and higher, respectively, than that of the homogeneous layer ($P_1^h(H_1)$) owing to their elongated (H_1^e) and shortened (H_2) effective thicknesses. The total number of thickness resonances by the metaporous layer in Fig. 3.8(a) is nearly double that of the homogeneous layer, which enables broadband sound absorption. The surface impedance of the metaporous layer in Fig. 3.8(a) is plotted in Fig. 3.9(b) in a comparison with that of the homogenous layer.

Figure 3.10 presents parametric studies of the metaporous layer in Fig. 3.8(a). Too large value of the partition width t would worsen the sound absorption performance of the metaporous layer because it decreases the volume fraction of the porous material in the unit cell. For the metaporous layer as seen in Fig. 3.8(a), the sound

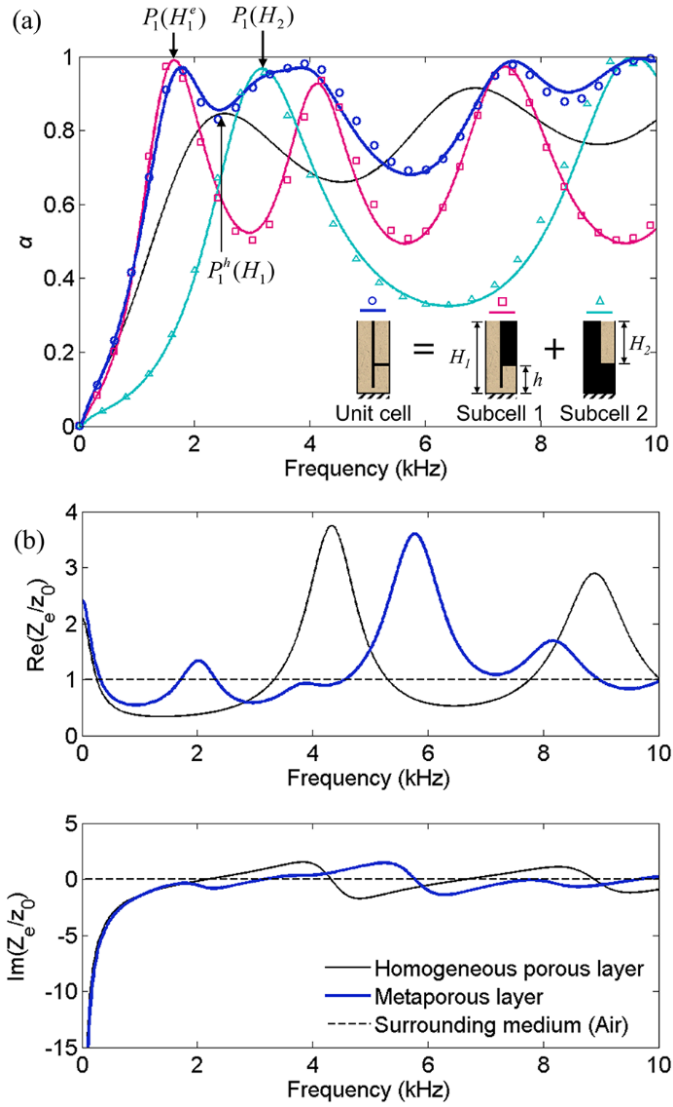


Fig. 3.9 (a) The absorption coefficients of the metaporous layer in Fig. 3.8(a) compared with the absorption coefficients of the effective layers made of its subcells. Solid lines denote the results by the theory and symbols, by the finite element analysis. (b) The real and imaginary parts of the surface impedances of the metaporous layer compared with those of homogeneous porous layer and the characteristic impedance of the surrounding air.

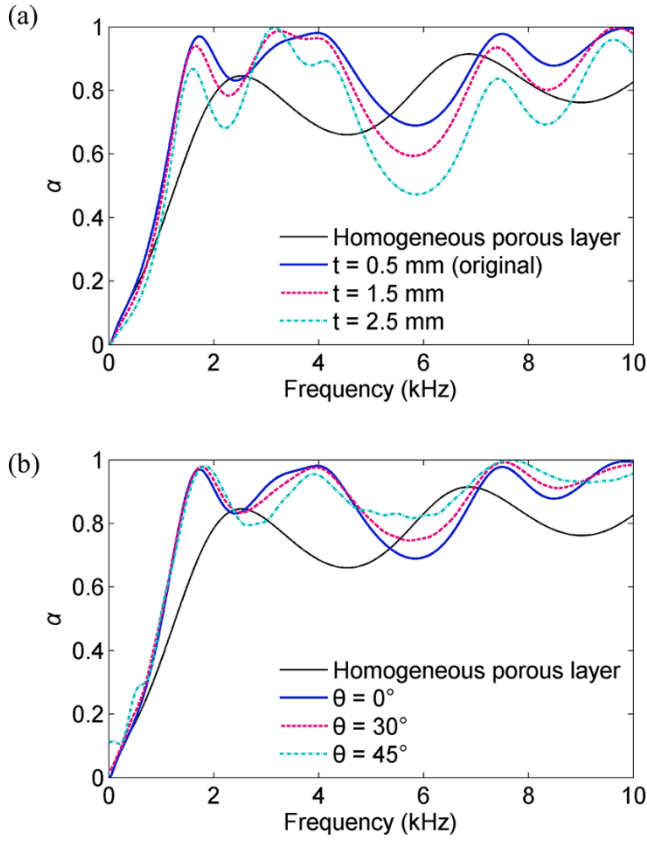


Fig. 3.10 (a) The absorption coefficients of the metaporous layer in Fig. 3.8(a) with different partition width values. (b) The absorption performance of the metaporous layer in 3.8(a) under oblique sound incidences ($\theta = 30^\circ$ and 45°) compared to that under normal sound incidence ($\theta = 0^\circ$).

absorptions of the layer with different widths of the partitions (e.g., $t = 0.5$ mm, 1.5 mm and 2.5 mm) are compared in Fig. 3.10(a). For the t values, the volume fraction factors η of the subcells are 0.45, 0.35 and 0.25, respectively. As explained above, the factor η determines the increase of the surface impedance of the layer. As the

width of the partitions increases too much, differences between the surface impedances of the layer and the characteristic impedance of air are enlarged, and then the overall absorption coefficients including those at the thickness resonances decrease. Figure 3.10(b) presents the absorption coefficients of the metaporous layer for obliquely-incident acoustic waves calculated by using the finite element model. The oblique angle (θ) of 30° and 45° have been tested. It can be observed in Fig. 3.10(b) that the absorption peaks move to higher frequencies slightly as the increase of the incidence angle but their effects are not significant in the overall sound-absorption performance under consideration.

Until now, the physical mechanisms of the sound absorption in the proposed metaporous layer were thoroughly investigated by deriving theoretical models based on the effective medium approach. The effectiveness of these present theoretical models used to explain the physics of the proposed metaporous layers is validated by comparing the results with those from the finite element method. With the combined effects of these mechanisms, the proposed metaporous layers exhibit a remarkable enhancement in the sound absorption characteristics over a wider range of frequencies by overcoming the thickness constraint.

3.3.5 Discussions

Based on the physical findings made, it is possible to design metaporous layers

which show better broadband sound absorption performance. Three possible configurations of the unit cell are suggested in the inset of Fig. 3.11. They are designed to consist of three or four subcells.

In Unit cell A, the subcell on the very left is acoustically disconnected from the other subcells and has the same thickness resonance frequencies with the original layer, as its thickness is the original thickness H_1 . Therefore, the existence of this subcell would put more resonance peaks between those of the metaporous layer made of the remaining subcells (Note that the former resonances corresponding to the thickness H_1 are still present). The effective surface impedance of Unit cell A would be represented as a parallel

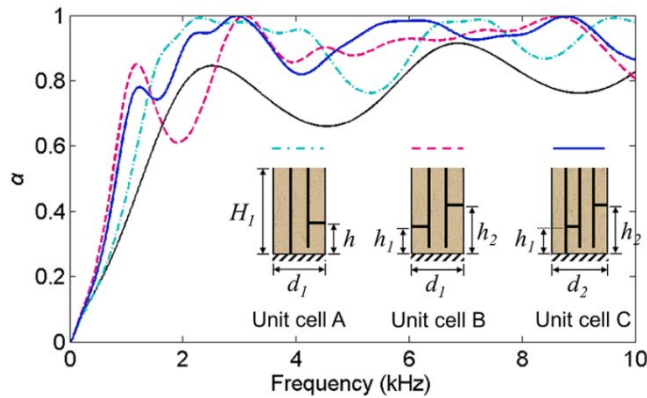


Fig. 3.11 The absorption coefficients of the metaporous layers made of three different unit cells shown in the inset. ($H_1 = 3.0$ cm, $h = 0.75$ cm, $h_1 = 0.75$ cm, $h_2 = 1.85$ cm, $d_1 = 1.5$ cm for the unit cells A and B; $d_2 = 1.6$ cm for the unit cell C. The gap size is set to be 1.0 mm for all the configurations.)

combination of the effective surface impedances of the three subcells in the same H_1 appear between the resonance peaks of the original layer; e.g., see Fig. 3.9(a)). The effective surface impedance of Unit cell A would be represented as a parallel combination of the effective surface impedances of the three subcells in the same manner, as expressed in Eq. (3.15).

When two gaps and two horizontal partitions are used to form Unit cell B, the first peak frequency can be lowered even more because the effective thickness of the metaporous layer will be much longer than the original layer thickness. The effective surface impedance of the subcell with two gaps can be modelled as an effective layer with two Helmholtz chambers. In the first and third porous slabs in Unit cell B, two subcells of effective thicknesses $(H_1 - h_1)$ and $(H_1 - h_2)$ diversify the thickness resonances in the mid and high frequency ranges.

Unit cell C, shown in Fig. 3.2 as noted above, is expected to exhibit the combined effects of unit cells A and B. All three of these unit cells show greatly improved broadband sound absorption performance over a homogenous porous layer with the same total thickness. Note that besides the value of h , which determines the effective thickness, the values of partition width t and gap size a can be considered as design parameters to obtain the desired acoustic performance.

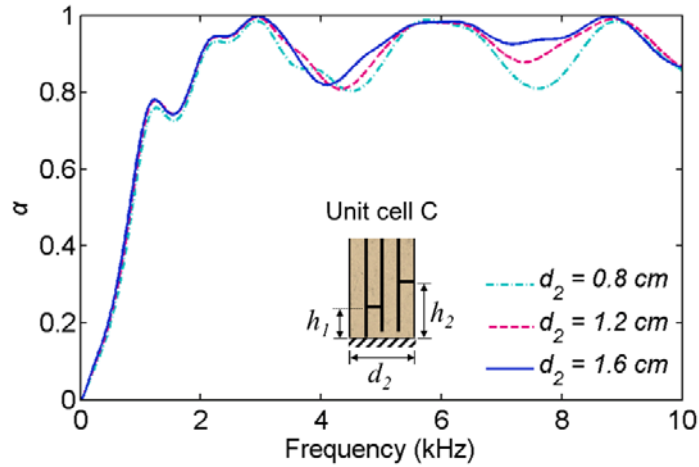


Fig. 3.12 The influences of the period of the unit cell on the absorption performances of the metaporous layer composed of Unit cell C shown in the inset. The geometric parameters are the same as in Fig. 3.11 except d_2 .

In Fig. 3.12, for the configuration of the Unit cell C, the influence of the period d_2 of the on the sound absorption performance is presented while maintaining other parameters. The values of the period d_2 are chosen within the subwavelength condition, especially $d_2 < \lambda_{\min}/2$; The minimum wavelength in the considered frequency range of this problem is around 1.7 cm. Because the absorption performance of the present metaporous layer is mostly affected by the effective thicknesses determined by the location of the horizontal rigid partitions regardless of the width of the subcells, the graph shows that the absorption performances remain the same except some small deviations. The differences come from the changed impedances as the ratio of the vertical rigid partitions on the surface of the

metaporous layer increases as the period decreases.

By embedding rigid partitions periodically parallel to the direction of the incident acoustic waves in a porous layer, the metaporous layers in this work have a locally reactive property, meaning that the surface impedance of the metaporous layer is independent of the nature of the incident waves and that acoustic wave propagation can be assumed to be normal to the surface of the metaporous layer [55]. Due to this locally reactive property of these metaporous layers within the frequency range of interest, it is physically valid to adopt the effective medium approach to build the theoretical models in this work. Note that the proposed metaporous layers are designed to have subwavelength periodicities in the frequency range considered here so as to guarantee the validity of the effective medium approach. If the scattering fields of acoustic waves are not negligible, the effective medium approach is not applicable in this work. In higher frequency ranges, theoretical models may predict results less accurately, even for the same configuration. Uses of such local reactions for sound attenuation can also be found in classical acoustic devices, such as the Helmholtz resonator, the side-branch resonator, and the Schroeder diffuser. Note that treatments which impose the locally reactive property in the present metaporous layers appear to be quite relevant to those of classical acoustic absorbers (e.g., the partitioning of acoustic cavities and the consideration of an impervious wall of negligible stiffness compared to the mass effect [55]).

3.4 Metaporous layer with multiple slow waves

In this section, metaporous layer with multiple slow waves will be presented. The metaporous layer, designed in a hard-backed porous layer with acoustically rigid partitions, can realize the broadband sound absorption, ranging from low frequencies to high frequencies. The considered rigid partitions are inserted in the porous layer perpendicularly to the wave incident direction and their lengths vary gradually. By deriving a theoretical model based on the effective medium approach, it is revealed that the so-called ‘metaporous layer’ has multiple slow wave propagations which are generated from the dispersion characteristic of multiple local resonators. In the proposed metaporous layer, two types of resonances allow the broadband sound absorption performance: (i) the global resonances, defined in a whole effective medium where the multiple slow waves propagate and (ii) the local resonances, geometrically confined at resonators. The influence of each type of resonances on the sound absorption performance of the proposed metaporous layer are thoroughly investigated in the theoretical and numerical manners.

3.4.1 Design of a metaporous layer with multiple slow waves

Figure 3.13(a) shows a schematic configuration of the proposed metaporous layer. The hard-backed metaporous layer, composed of infinitely periodic unit cells along x direction, has a finite thickness H in the wave incident/reflected y direction. In the

unit cell, one rigid vertical partition parallel to the y direction acts as a pillar and N rigid horizontal partitions are attached to the pillar (here, $N = 6$) in a porous slab of the width d and the thickness H . The N horizontal partitions have a uniform thickness t and are regularly spaced ΔH apart each other. The length of these partitions

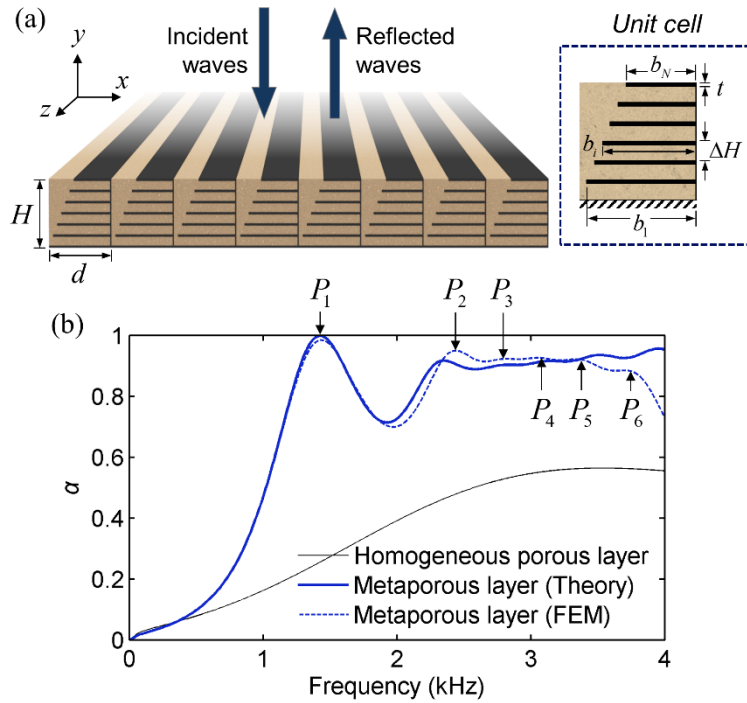


Fig. 3.13 (a) A schematic configuration of the present metaporous layer and its unit cell composed of a hard-backed porous layer and rigid partitions. (b) The absorption coefficients of the metaporous layer compared to those of the homogeneous porous layer. ($H = 3.0$ cm, $d = 3.0$ cm, $t = 2.0$ mm, $b_N = 1.8$ cm, $\Delta H = H/N$, and $N = 6$. The length of the partition b_i from the bottom is determined as $b_i = d - i(d - b_N)/N$, $i = 1, 2, \dots, N$)

varies linearly along the wave incident direction. Then, the horizontal partitions and the pillar form N quarter-wavelength side branch resonators filled with porous material within the unit cell. Figure 3.13(b) shows the sound absorption coefficients of the present metaporous layer in the frequency range up to 4 kHz. It is apparently observable that the metaporous layer has highly enhanced absorption performance over a broad range of frequencies compared with the homogeneous porous layer.

The configuration of the metaporous layer may look similar to the previously-studied electromagnetic [20], [22] or acoustic metamaterials [14], [74] of tapered shapes that use resonance trapping at specific positions. However, as well as the resonance trapping in the local side resonators, the proposed metaporous layer allows low frequency absorption peaks by slow waves. This phenomenon can be successfully explained by deriving theoretical model to describe wave behavior in the metaporous layer.

3.4.2 Effective medium model for the multiple slow wave media

The wave propagation in the present unit cell is similar to the one in duct-type acoustic metamaterials with periodic side resonators [12], [29], [30], [75]. The wave motions in the metamaterials are described using the effective medium concept to regard the metamaterial as a homogenized medium. Then, the metamaterials have negative bulk modulus in the frequency range of band gap formed by local

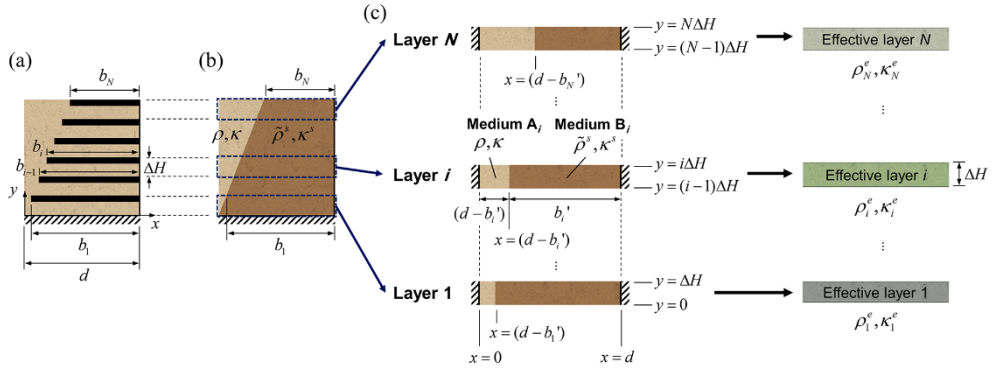


Fig. 3.14 A theoretical model of the proposed metaporous layer which can be modeled as an equivalent multilayer consisting of several effective layers. (a) The unit cell configuration. (b) The unit cell is partially filled with a *static* effective medium of anisotropic material properties $\tilde{\rho}^s$ and κ^s . (c) The unit cell in (b) is sequentially divided into N layers which can be represented as effective layers of *dynamic* material properties ρ_i^e and κ_i^e .

resonances of the side resonators. In the band gap (negative modulus zone), the wave propagation velocity becomes zero so that the waves are not allowed to propagate into the metamaterials. Below the lowest bound of the band gap, the wave velocity in the metamaterials has smaller value than in the medium which fills the duct with the decrease of the bulk modulus. As such metamaterials, the metaporous layer can be analyzed by employing effective medium approach.

To build a theoretical model for the present metaporous layer, we employ an effective medium approach that may convert wave motions in the two-dimensional

configuration in Fig. 3.14(a) into those in the one-dimensional multilayered model. Following the results in section 3.3.2, the region containing the horizontal rigid partitions can be modelled as an effective medium with *static* anisotropic properties, which is illustrated as a dark brown-colored trapezoidal part in Fig. 3.14(b). The effective density tensor $\tilde{\rho}^s$ and bulk modulus κ^s of this medium can be expressed as

$$\tilde{\rho}^s = \begin{pmatrix} \rho_x^s & 0 \\ 0 & \rho_y^s \end{pmatrix} = \begin{pmatrix} \rho/\eta & 0 \\ 0 & \infty \end{pmatrix}, \quad \kappa^s = \kappa/\eta, \quad (3.16)$$

where $\eta (= 1 - t/\Delta H)$ is the volume ratio of the porous medium in the y direction. In Eq. (3.16), ρ and κ are the acoustic density and the bulk modulus of the base porous medium, respectively. The acoustic waves in this medium are confined along the x direction with the effective velocity $c^s = \sqrt{\kappa^s/\rho_x^s} = c$.

Because of the discrete variation of the length of the horizontal rigid partitions, we horizontally divide the unit cell into N rectangular parts, the thickness of each part is assumed to be identical to ΔH as shown in Fig. 3.14(b) and (c). Due to the presence of the vertical rigid partition parallel to the y direction, both sides of the N -part layers at $x=0$ and $x=d$ are regarded as hard-backed walls. Then, each layer acts as if it were a thin rectangular duct of a length ΔH , filled with dissimilar materials. Since layer i is partially filled with the base porous medium denoted by a light brown-colored medium A_i and the *static* effective medium denoted by a dark

brown-colored medium B_i , as indicated in the left figure of Fig. 3.14(c), the distributions of the density and bulk modulus may be expressed as

$$\{\tilde{\rho}_i(x, y), \kappa_i(x, y)\} = \begin{cases} \{\rho, \kappa\} & \text{for } 0 < x \leq (d - b_i'), \text{ medium } A_i \\ \{\tilde{\rho}^s, \kappa^s\} & \text{for } (d - b_i') < x < d, \text{ medium } B_i \end{cases} \quad (3.17)$$

with an averaged value of $b_i' (= (b_{i-1} + b_i)/2)$.

The effective medium properties of the N layers can be obtained by considering the dispersion relation of medium A_i , affected by wave interaction with the medium B_i . Because wave motion in the medium B_i occurs mainly along the x direction, the medium B_i may be regarded as a locally reacting liner in an acoustic duct [56] whose surface acoustic impedance at $x = (d - b_i')$ from the right-hand side hard wall ($x = d$) is given by [76]

$$Z_{B_i} = -j\rho_x^s c^s \cot(kb_i') = -j\frac{\rho c}{\eta} \cot(kb_i'), \quad (3.18)$$

where k is the wavenumber of the base porous medium.

On the other hand, the guided modes in medium A_i have x - and y -directional wave vector components, k_{ix} and k_{iy} , respectively, which satisfy $k_i^2 (= k^2) = k_{ix}^2 + k_{iy}^2$.

Since the sound wave in medium A_i propagates along the y direction and oscillates along the x direction, the pressure field can be written as

$$p_{A_i}(x, y; \omega) = C_i \cos(k_{ix}x) e^{jk_{iy}y} e^{j\omega t}, \quad (3.19)$$

where C_i is the amplitude coefficient of the pressure field and ω denotes the angular frequency. Note that the wave function was so chosen to satisfy the boundary condition of the left-hand side hard wall. The x -directional particle velocity in the medium A_i is given by

$$v_{A_i,x}(x, y; \omega) = \frac{C_i k_{ix}}{j\omega\rho} \sin(k_{ix}x) e^{jk_{iy}y} e^{j\omega t}. \quad (3.20)$$

Along the interface between the media A_i and B_i (i.e., at $x = (d - b_i')$), the pressure and velocity fields in Eqs. (3.19) and (3.20) should meet the interface condition of $(p_{A_i} / v_{A_i,x})_{x=d-b_i'} = Z_{B_i}$, which is derived as

$$\frac{\cos(k_{ix}(d - b_i'))}{\frac{k_{ix}}{j\omega\rho} \sin(k_{ix}(d - b_i'))} = -j \frac{\rho c}{\eta} \cot(kb_i'). \quad (3.21)$$

The rearrangement of Eq. (3.21) gives the dispersion relation in the layer i shown in the left figure of Fig. 3.14(c).

$$k_{ix} \tan(k_{ix}(d - b_i')) = -\eta k \tan(kb_i'). \quad (3.22)$$

In a low frequency range, one can get the expressions related to the x - and y -directional wave-vector components as

$$\begin{aligned} k_{ix}^2 &= -\eta k \tan(kb_i') / (d - b_i'), \\ k_{iy} &= k \sqrt{1 + \eta \tan(kb_i') / k(d - b_i')}. \end{aligned} \quad (3.23)$$

By using the derived dispersion relation in Eq. (3.23), the N layers can be regarded as the N effective layers with *dynamic* properties, ρ_i^e and κ_i^e , as shown in the right-hand side figure of Fig. 3.14(c).

Recall that the vertical rigid partitions in the metaporous layer block sound propagation in the x direction. While the x -directional wave propagation can be neglected, the y -directional component of the effective acoustic density of the effective medium can be obtained from

$$\frac{1}{\rho_i^e} = \frac{(1 - \phi_i)}{\rho} + \frac{\phi_i}{\rho_y^s}. \quad (3.24)$$

Since $\rho_y^s = \infty$ as denoted in Eq. (3.16), the effective acoustic density ρ_i^e of the effective medium layer i can be given by

$$\rho_i^e = \rho / (1 - \phi_i). \quad (3.25)$$

The effective sound velocity in the effective medium layer is obtained from the

relation $c_i^e = \omega/k_i^e = \omega/k_{iy}$,

$$c_i^e = \frac{c}{\sqrt{1 + \eta \tan(kb_i)/k(d - b_i)}}. \quad (3.26)$$

Then the effective bulk modulus is determined as follows

$$\kappa_i^e = \rho_i^e (c_i^e)^2 = \frac{\kappa}{(1 - \phi_i) \cdot [1 + \eta \tan(kb_i)/k(d - b_i)]}. \quad (3.27)$$

The effective bulk modulus is also increased by a factor $1/(1 - \phi_i)$, due to the x -directional rigid partitions. In addition, the bulk modulus is affected by the dispersion that originate from the wave interaction between the waveguide and the periodic side resonators. It is remarked that the derived expressions of the effective parameters in the present metaporous layer agree well with the results of Ref. [12] which were obtained for an air-rigid structure with the side resonators of the same resonance frequencies (the constant b_i).

Figure 3.15(a) shows the final equivalent model of the metaporous layer in Fig. 3.13(a). For an effective layer i ($i=1,2,\dots,N$), the expression of the effective material properties can be given by Eq. (3.25)-(3.27). Figures 3.15(b) and (c) show the effective medium properties in the effective layers calculated from Eq. (3.25) and Eq. (3.27), respectively. First, we observe that the imaginary parts of the effective parameters plotted in Fig. 3.15(b) and (c) meet the condition of the

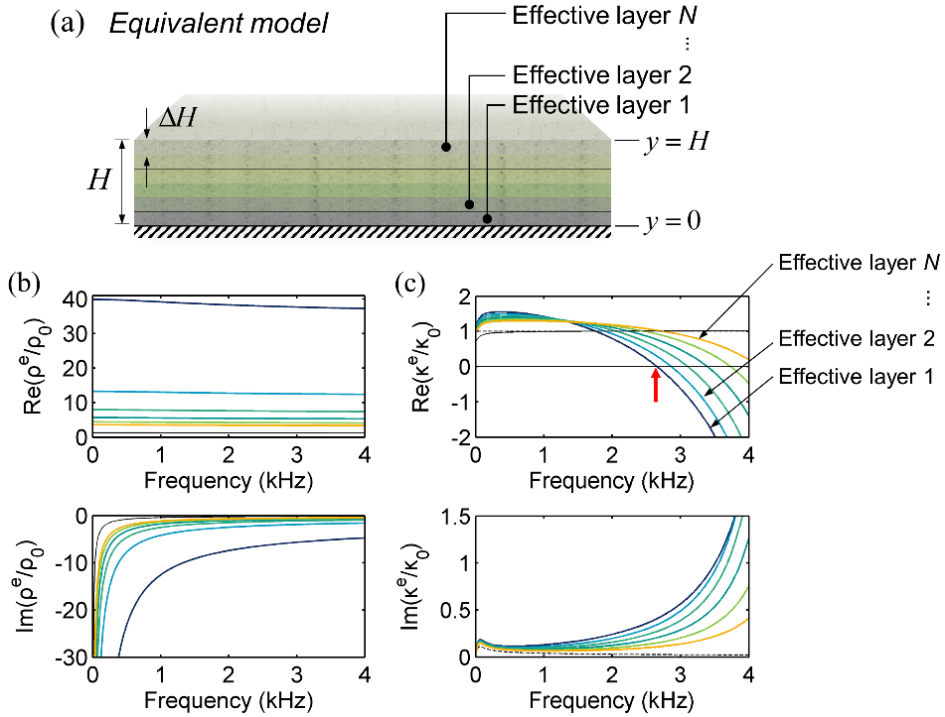


Fig. 3.15 (a) The metaporous layer in Fig. 3.13(a) can be modeled as a multilayer consisting of N effective layers. (b) Effective densities and (c) effective bulk moduli in the effective layers (normalized by the corresponding properties of air, ρ_0 and κ_0). The red arrow in (c) denotes the lower bound of the negative bulk modulus band of the effective layer 1.

dissipative conventional media, i.e., $\text{Im}(\rho_i^e) < 0$ and $\text{Im}(\kappa_i^e) > 0$ [36]. For comparison, the acoustic properties of the homogeneous bulk porous material are also shown in the graphs (black lines). The Johnson-Champoux-Allard model for rigid porous materials is employed to represent the acoustic density and bulk

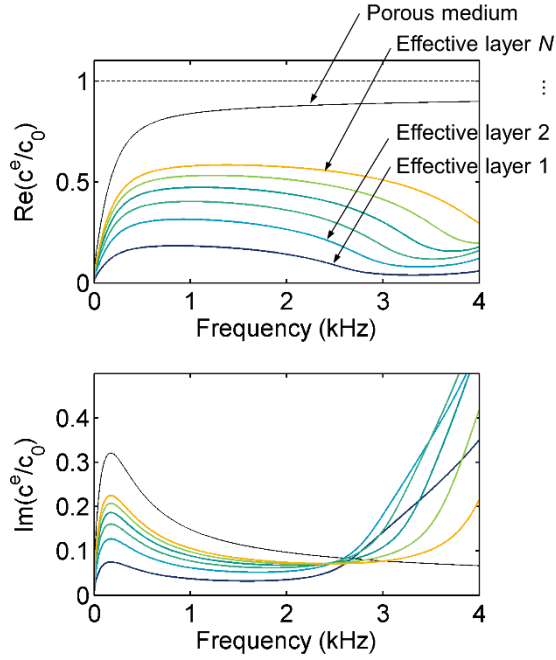


Fig. 3.16 Real and imaginary parts of effective velocities in the effective layers normalized by the sound velocity of air, c_0 .

modulus of the porous material used in this work. The material parameters of air and porous materials used in this work can be found in Table 2.2, porous material B. As shown in in Fig. 3.15(c), the effective bulk moduli become negative at a certain frequency range because resonance gaps are formed by the side resonators. This result is consistent with earlier studies with the acoustic metamaterials of negative bulk moduli [12], [29], [30].

Figure 3.16 shows real and imaginary parts of effective velocities in the effective

layers. According to Fig. 3.16, the effective sound velocities in the effective layers are lower than c , making N different slow waves in the N effective layers, respectively. The slow wave phenomenon may be viewed as if the wave propagation distance is increased but it is different from an actual path elongation used in the coiling-up space [71], [72]. Note that the wave velocities do not reach zero in the band gaps due to the dissipative property of the porous material [75]. The change of the effective material properties also affects the impedance of the effective media since the effective characteristic impedance is $z_i^e = \rho_i^e c_i^e = \sqrt{\rho_i^e \kappa_i^e}$. Given that the amounts of reflected or transmitted sound energy are critically affected by the impedance of an acoustic medium, the sound absorption performance of the metaporous layer is strongly influenced by the effective impedance.

For given characteristic impedance z_i^e and the wavenumber k_i^e in the effective layer i , the effective surface impedance Z_i^e on the top surface of the effective layer i (at $y = i\Delta H$) is represented as a successive relation of the constituting layers [55],

$$\begin{aligned} Z_1^e &= -jz_1^e \cot(k_1^e \Delta H), \\ Z_i^e &= z_i^e \frac{Z_{i-1}^e + jz_i^e \tan(k_i^e \Delta H)}{jZ_{i-1}^e \tan(k_i^e \Delta H) + z_i^e} \quad (i = 2, 3, \dots, N). \end{aligned} \quad (3.28)$$

Once the total surface impedance of the metaporous layer Z_N^e is obtained, the reflection coefficient R and absorption coefficient α are calculated as

$R = (Z_N^e - z_0)/(Z_N^e + z_0)$ and $\alpha = 1 - |R|^2$, respectively, where z_0 is the characteristic impedance of the wave incidence medium, air. Figure 3.13(b) shows the sound absorption coefficients of the present metaporous layer in the frequency range up to 4 kHz. It is apparently observable that the metaporous layer has highly enhanced absorption performance over a broad range of frequencies compared with the homogeneous porous layer.

To check the validity of the theoretical model, we compare the results from the numerical method, finite element model (FEM) using COMSOL Multiphysics 4.3 [69]. Although there are some discrepancies between the results from theoretical model and finite element one, their results show good agreement. In the numerical simulations, one-unit cell is considered and the Floquet-Bloch periodic boundary condition is imposed on the boundaries on the x direction of the unit cell to represent its periodic nature.

3.4.3 Sound absorption mechanism of the metaporous layer

In order to understand the sound absorbing mechanism of the metaporous layer, the wave fields at the specific frequencies corresponding to the sound absorption peaks which are obtained from the theoretical and numerical analyses are examined. Figures 3.17 presents the magnitude of the acoustic particle velocities in the unit cell

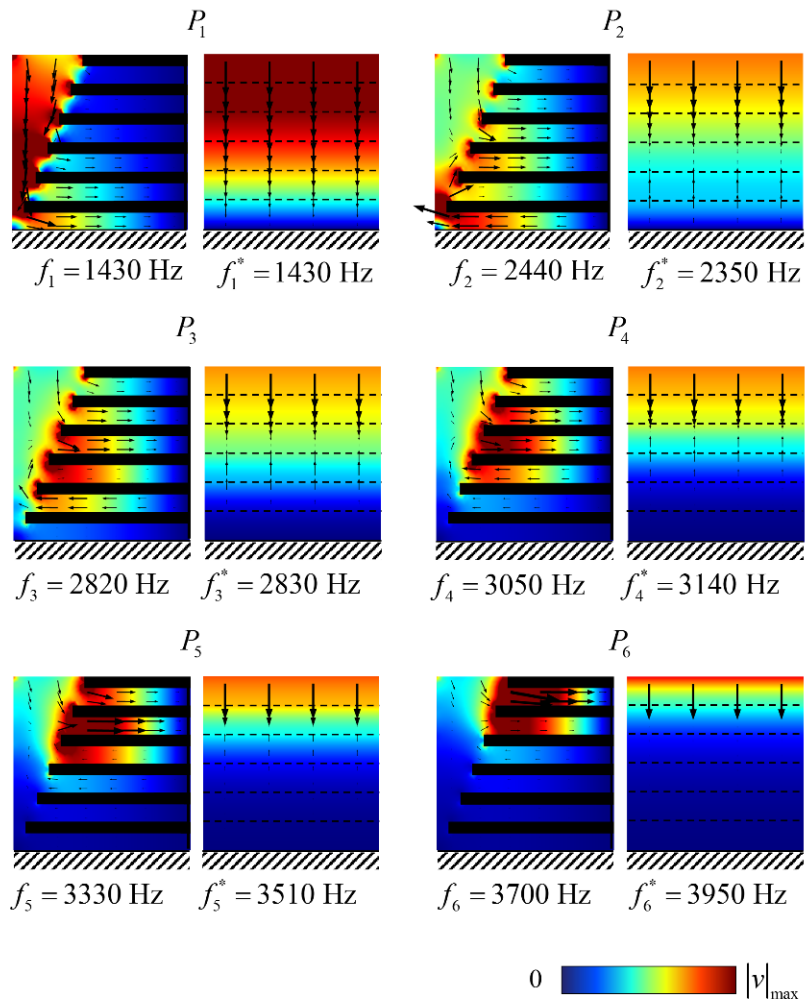


Fig. 3.17 The magnitude of particle velocities in the metaporous layer at the peak frequencies $P_1 \sim P_6$ indicated in Fig. 3.13(b). The results are obtained by numerical (left-hand side) and theoretical (right-hand side) methods. The peak frequencies obtained from the corresponding analysis are presented below.

at those peaks, denoted as P_1, P_2, \dots, P_6 , respectively, in Fig. 3.13(b). For each absorption peak, the left-hand sided plots are obtained from the FEM model while the right-hand sided ones are from the derived theoretical model. The particle motions from the FEM model are so complicated that it is not easy to understand the sound absorption mechanisms in the structures. Meanwhile, the theoretical representations convert the complicated two-dimensional wave motions into the one-dimensional one in the effective medium along the y direction, which are really helpful to interpret what happens in the considered metaporous layer.

Figure 3.18(a) shows the normalized particle velocity profiles at the absorption peaks P_1 and P_2 from the theoretical analysis. This graph denotes the same results with the right-hand sided plots in Fig. 3.17 but with the phase of the velocities. The noticeable thing is that the wave fields in the metaporous layer, composed of effective layers with different properties, can be explained as if in the uniform layer. The particle velocity fields at P_1 forms a quarter-wavelength profile which is zero at the bottom ($y=0$) and maximum at the top ($y=H^*$) of the effective layers. Likewise, the velocity fields at P_2 forms a three quarter-wavelength profile. These imply that the absorption peaks P_1 and P_2 correspond to the global resonance modes occurred along the thickness direction of the effective multilayer, as expressed by $H^* = (2n-1) \cdot \lambda^* / 4$. It should be noted that the effective thickness

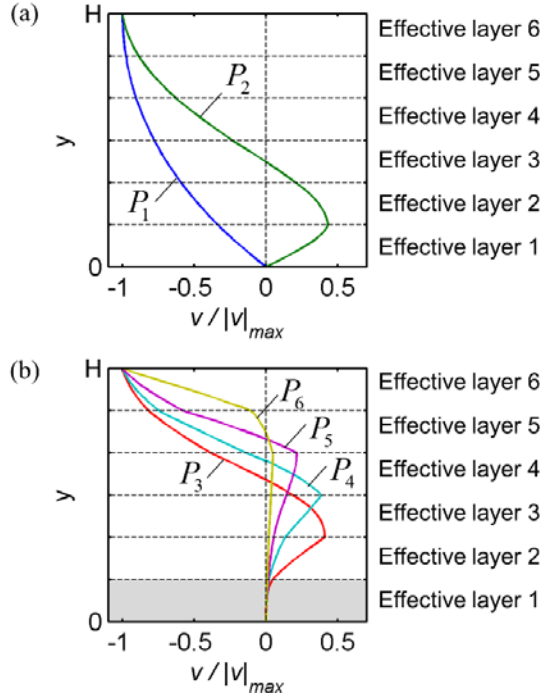


Fig. 3.18 Acoustic velocity fields in the metaporous at the peak frequencies (a) P_1 and P_2 , (b) $P_3 \sim P_6$ indicated in Fig. 3.13(b) obtained by the theoretical methods.

H^* of the whole effective multilayer ($H^* = \sum_{i=1}^6 h_i^*$ with the thickness h_i^* of the effective layer i) is much longer than the geometric thickness dimension H due to the propagations of the slow waves in the metaporous layer than those in the homogeneous porous one. As a result, the thickness resonances occur at much longer wavelengths λ^* (i.e., the lower frequencies) in the present metaporous layer, so as to overcome the thickness constraint in sound absorption effectively. Because the constituting effective media of the metaporous layer are dispersive, the elongation

factor of the effective thickness may not be definitely defined as a fixed value over the frequency, contrary to the metaporous layers that used rigid partitioning to control the effective thickness in section 3.3. However, provided that the resonance frequencies of the original porous layer corresponding to $\lambda/4$ and $3\lambda/4$ are 3400 and 8500 Hz, it is possible to evaluate that the present metaporous layer works as an effective layer with elongated thicknesses H^* by factors 2.4 and 3.5 of the original thickness H at the first and second peak frequencies.

Now we move to the absorption peaks at higher frequencies, $P_3 \sim P_6$. The particle velocity fields in Figs. 3.17 and 3.18(b) show that the participating region for the resonance modes tend to move upward within the effective multilayers as the frequency increases. While the resonances P_1 and P_2 occur in the whole effective layers from 1 to 6, the particle velocity fields at other resonances $P_3 \sim P_6$ vary through some parts of the multilayers. At P_3 , for example, the wave velocity in the effective layer 1 (see gray region in Fig. 3.18(b)) at this frequency is very low. This is because the corresponding frequency of P_3 is in the band gap, i.e., negative bulk modulus zone, of the effective layer 1. A red arrow in Fig. 3.15(c) denotes the low frequency bound of the band gap, 2655 Hz. Because the absorption peak P_3 lies in the negative modulus zone, the waves are reflected on the surface of the effective layer 1. Therefore, only five upper layers (the effective layers 2 to 6) are participating

in the resonance mode of the absorption peak P_3 and the remaining effective layer 1 works as a layer filled with a rigid material. In other words, P_3 corresponds to the global resonance related to the slow wave propagation in effective multilayer 2 to 6, and its resonance frequency is determined by a relation $\sum_{i=2}^6 h_i^* = 3\lambda^*/4$. Similarly, only four effective layers (the effective layer 3 to 6) are participating the global resonance mode for the absorption peak P_4 , and similar phenomena occur at P_5 and P_6 as well. However, these resonance modes are not clearly distinguishable because the local resonances at the side resonators are also generated.

The absorption curves of the present metaporous layer with and without porous material are compared together in Fig. 3.19(a). In the figure, the meta-layer without a porous material has high absorption peaks at the frequencies for the local resonances occurring at the side branch resonators. Figure 3.19(b) shows the particle velocity fields at two peaks denoted as P_2^L and P_3^L in Fig. 3.19(a). The particle velocity fields at those peaks are strongly confined in the second and third side branch resonators from the bottom, with the quarter-wavelength resonance profiles. The local resonances of the side resonators exist in the metaporous layer in Fig. 3.13(a) as well, however, the waves are not confined in the specific location of the side resonators strongly as in here because the global resonances and local resonances are generated concurrently. Without the porous material, the absorption

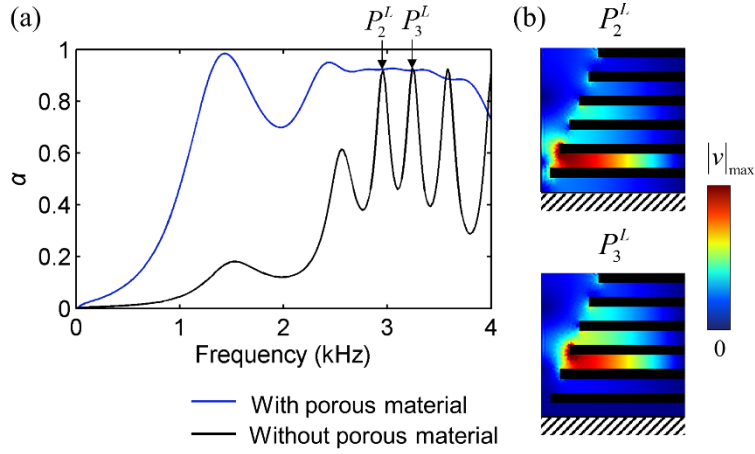


Fig. 3.19 (a) The absorption performance of the metamaterial configuration in Fig. 3.13(a) when the porous material is removed compared with the one of the metaporous layer. (b) The magnitude of the particle velocities at the absorption peaks P_2^L and P_3^L .

peaks from global resonances due to the slow wave propagation are relatively small. It denotes that the dissipative effect of the porous medium on the global resonance modes are crucial because the global resonances are generated all over the layer in along the y direction.

3.4.4 Discussions

The sound absorption performance of the proposed metaporous layer can be tailored by controlling the geometric parameters of the inserted rigid partitions. The influence

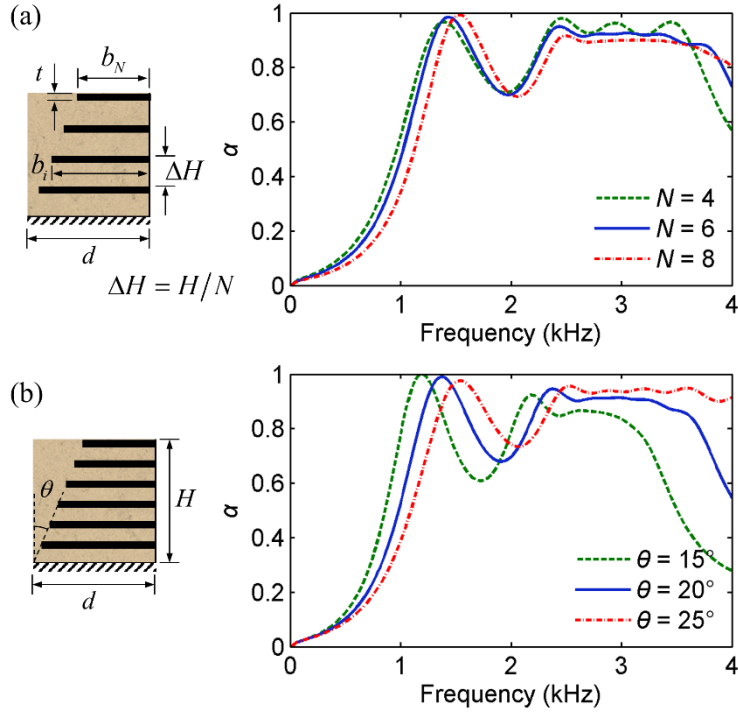


Fig. 3.20 (a) The influence of the number of the inserted partitions on the absorption performance of the metaporous layer. The geometric parameters are the same as in Fig. 3.13(a) except N . (b) The influence of the slope angle of the partitions on the absorption performance of the metaporous layer.

of the number of horizontal partitions in the porous layer is investigated in Fig. 3.20(a) under the constraints of the layer thickness H , the partition thickness t , and the shortest partition length b_N . When the number of rigid partitions increases, the property changes along the layers' thickness direction vary smoothly so as to result in more continuous changes between the effective layers. Therefore, the metaporous

layer with 8 horizontal partitions ($N = 8$) has smoother absorption curve compared to the case of $N = 4$. Since the partition thickness t is fixed, the volume ratio of the porous medium in the y direction, η , decreases as the increase of N . This results in the slight increase of sound velocity in the effective multilayer, consequently the absorption peak frequencies related to the slow waves tend to shift to slightly higher frequencies.

In Fig. 3.20(b), the change of the horizontal partition lengths is represented as the angle θ between the y axis and an imaginary line connecting the ends of the partitions. As the angle decreases, the overall lengths of the partitions increase, which result in the slower wave propagation in the effective multilayer. Accordingly, the absorption peaks shift to lower-frequency values. On the other hand, the absorption coefficients in high-frequency region become decreased because of a larger reflection of the incident sound energy on the surface of the metaporous layer. There would be other parameters to control the properties of the metaporous layer and some optimization techniques based on the multilayering scheme [58], [59] can be used for enhancement of sound absorption performance.

Figure 3.21 presents the influence of the period of the unit cell on the sound absorption performance. For the fundamental configuration of the unit cell given in Fig. 3.13(a), the lengths of the horizontal rigid partitions, b_i , change according to

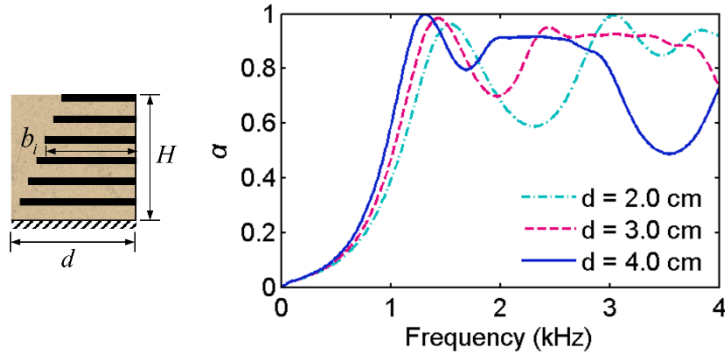


Fig. 3.21 The influence of the unit cell period on the absorption performance of the metaporous layer. The geometric parameters are the same as in Fig. 3.13(a) except d and b_i .

the change of the period to maintain the same proportion of the original unit cell configuration, while other geometric parameters are fixed. For example, the partition lengths reduce to $2b_i/3$ when the period is changed to 2.0 cm from the original value, 3.0 cm. It is observable that the first peaks move to higher frequencies as the period decreases. As it has been discussed above, it is due to the overall increase of the wave velocities in the metaporous layer due to the decrease of the partition lengths. Other peaks also move to other frequencies according to the changed wave velocities caused by the change of the partition lengths. This study suggests that the sound absorption performance of the present metaporous layer is dependent on the given periodicity which is distinct from the earlier observations made in section 3.3.5 for the metaporous layer with tuned thickness resonances. For the present

metaporous layer, the lengths of the rigid partitions should be adjusted to ensure the sound absorption performances of the metaporous layer.

Among the parameter studies, we would like to emphasize the case of the insertion of the horizontal rigid partitions with the same length in the metaporous layer, in which the unit cell has a configuration as shown in Fig. 3.22(a). According to the theoretical model derived in this work, these identical partitions cause the effective layers to be homogenous along the y direction because of the same effective properties at every layer. This means a single slow wave propagates in the whole effective layers, as shown in Fig. 3.22(b). The partition lengths are set to have the same effective properties with the lowest effective layer (effective layer 1) in Fig. 3.15(a). Figure 3.22(c) shows the sound absorption performance of the current metaporous layer. The absorption peaks denoted as P_1^G , P_2^G and P_3^G originate from the global resonances of the single slow wave propagation in the effective layer in the thickness direction ($H^* = \lambda^*/4$, $3\lambda^*/4$, and $5\lambda^*/4$). Compared to the performance by the multiple slow waves in Fig. 3.13(b), the peaks from the single slow wave propagation appear in lower-frequency range. It is because the wave velocity in the current metaporous layer is averagely slower than those of the multiple slow wave medium, as compared in Fig. 3.16 and Fig. 3.22(b). As well as the single slow wave propagation, the installation of the identical partitions allows only one kind of side branch resonator, in which the local resonance occurs at P^L

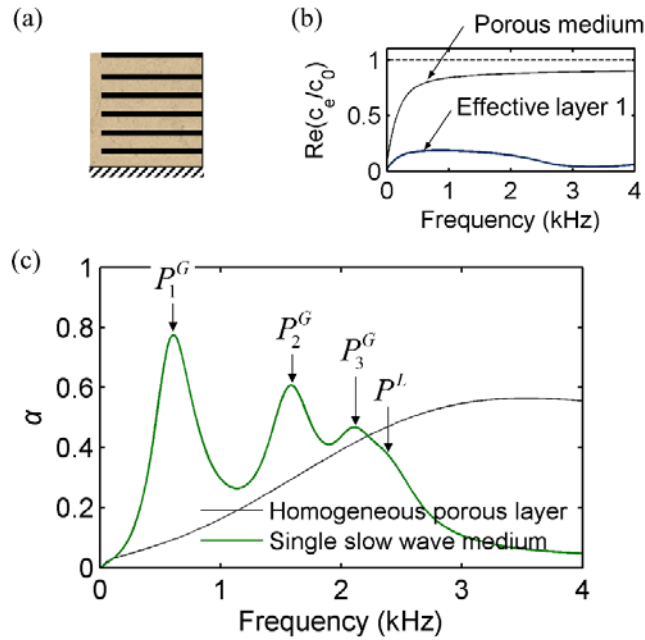


Fig. 3.22 (a) The unit cell configuration of the metaporous layer with the same partition lengths. (b) The wave propagation velocity in the metaporous configuration in (a). The present metaporous layer has single slow wave propagation. (c) The sound absorption performance of the single slow wave medium.

in Fig. 3.22(c). The sound absorption performance from the single slow wave propagation and one type of side branch resonator is very poor except at some peaks. Therefore, these observations apparently substantiate the powerfulness of the proposed metaporous layer having multiple slow waves for broadband sound absorption.

The configuration of the present metaporous layer can be expanded to the 3 dimensional configurations and the effective medium models also can be derived for corresponding layers. Figure 3.23 shows configurations of metaporous layers in cylindrical coordinates. The metaporous layers are axisymmetric to the z direction. For the axisymmetric configurations, two types of metaporous layers can be built. The first one is shown in Fig. 3.23(a), the rigid partitions of the shapes of circular plates are inserted aligned to the center of the cylindrical coordinates. The second one is shown in Fig. 3.23(b), the rigid partitions are aligned to the outer side of the

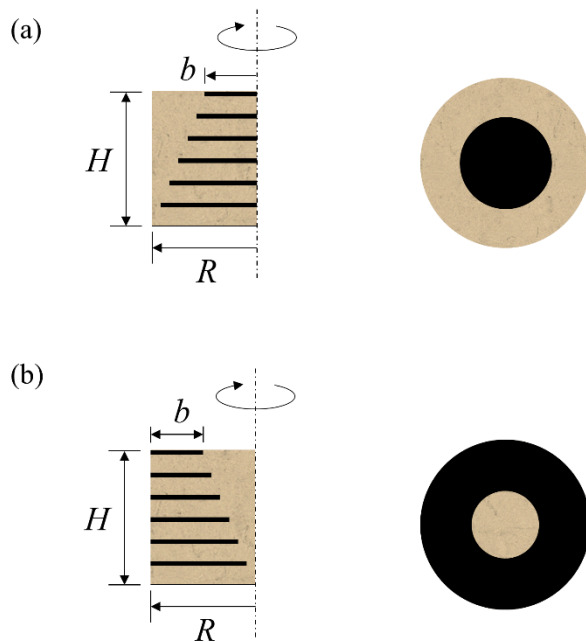


Fig. 3.23 Axisymmetric configurations of the metaporous layers. (a) The rigid partition of circular shapes are aligned at the center of the layer. (b) The rigid partitions of disk shapes are aligned at the outer boundary of the layer.

circle and have the shapes of disk. The right-hand side figures of Figs. 3.23(a) and (b) show the top view of the considered axisymmetric metaporous layers.

Figures 3.24 and 3.25 show the absorption coefficients of the metaporous configuration in Fig. 3.23(a) and (b), respectively. The radius of the metaporous layer

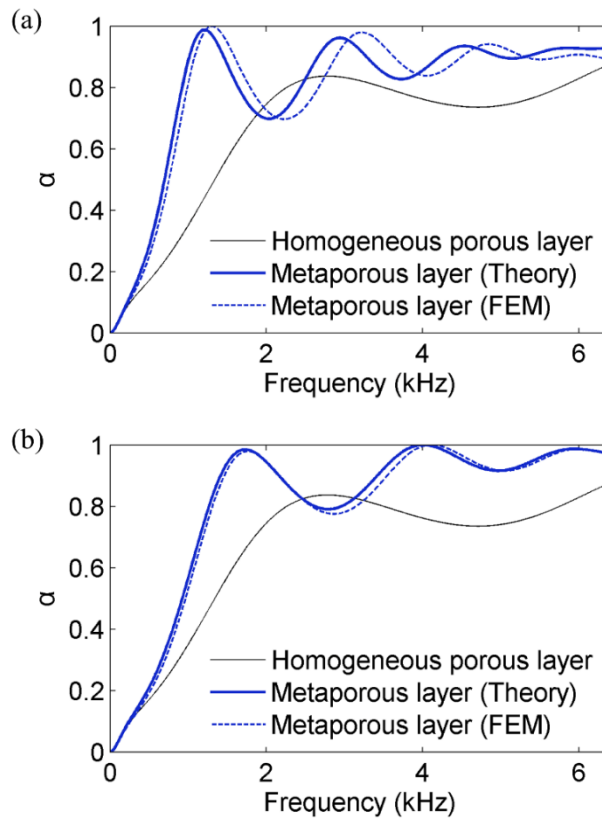


Fig. 3.24 The absorption coefficients obtained by numerical and theoretical methods for the metaporous layer configurations presented in Fig. 3.23(a) when b is (a) 1.15 cm and (b) 0.85 cm, respectively.

R is 1.45 cm and the thickness H is 3.0 cm. In the defined dimension, the absorption coefficients up to 6.4 kHz can be calculated. The theoretical models based on the effective medium approach for the considered metaporous layers are presented in Appendix I. Theoretical analysis shows that the multiple slow waves are successfully generated in the present axisymmetric metaporous layers. In addition to that, not only

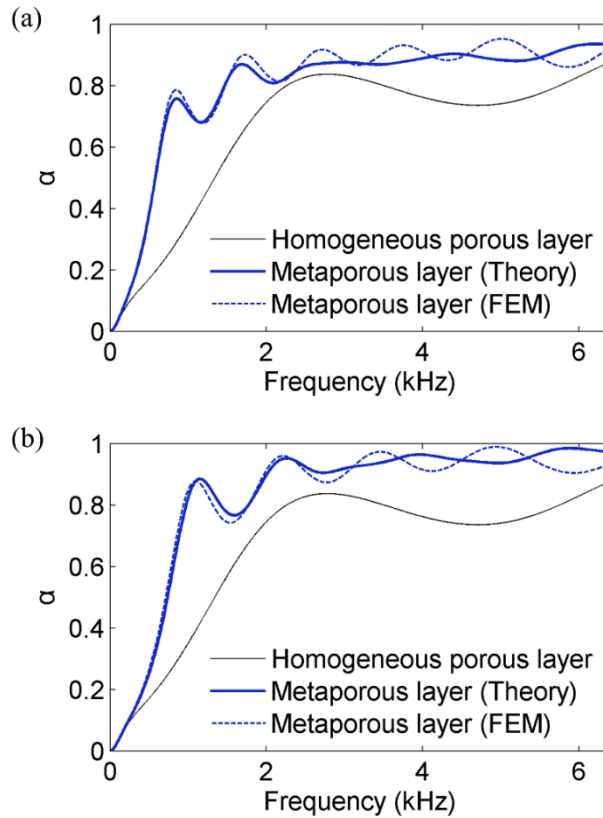


Fig. 3.25 The absorption coefficients obtained by numerical and theoretical methods for the metaporous layer configurations presented in Fig. 3.23(b) when b is (a) 0.55 cm and (b) 0.25 cm, respectively.

the simple partition length b in Figs. 3.24(a) and (b) but the shape of inserted rigid partitions affects considerably on the effective sound velocities, which is distinctive from the results of two dimensional metaporous layers. The results in Figs. 3.24 and 3.25, by comparing with the results obtained from the numerical method, show that the derived theoretical models express the behavior in the metaporous layer efficiently. Figures 3.24(a) and (b) are the results when b indicated in Fig. 3.23(a) is 1.15 cm and 0.85 cm, respectively. Likewise, Figs. 3.25(a) and (b) are the results when b indicated in Fig. 3.23(b) is 0.55 cm and 0.25 cm. The material properties of the porous material used here can be found in Table 3.1, porous material C. It is shown that the absorption performances are considerably enhanced in the frequency range of considered due to the multiple slow wave propagation in the metaporous layers.

3.5 Concluding remarks

In this chapter, the acoustic metamaterials designed with porous layer and rigid partitions, which is called metaporous layers, were presented in an effort to achieve broadband sound absorption performance. The proposed metaporous layers are classified into two types; the one with tuned thickness resonances and the other one with multiple slow waves. The two types of metaporous layers have in common that both of them use the resonance phenomena related to the thickness of the porous

layer. However, they also have difference in that the first one increases or decreases the effective thicknesses directly by guiding the wave path, on the other hand, the other one controls the peak frequencies of the absorption by tailoring effective wave velocity in the porous layer. Contrary to the acoustic metamaterials for narrowband performance, the various and multiple resonance modes enabled high sound absorption over a broad range of frequencies, which covers the low frequency range as well. The proposed metaporous layer having such an outstanding sound absorption performance is expected to be a solution to overcome the performance limitation of sound-absorbing system.

For the metaporous layer presented in section 3.3, vertical and horizontal rigid partitions are periodically inserted in a homogeneous porous layer and a narrow gap is introduced to connect neighboring porous slabs in a periodic unit cell. The increased sound absorption by the metaporous layer is due to three physical mechanisms. First, the absorption peak values are substantially increased at the thickness resonance frequencies because the effective surface impedances of the metaporous layer match better the characteristic impedance of the surrounding air. Secondly, the effective thickness along the direction of the incident wave is elongated, thus lowering the lower bound frequency of effective sound absorption. Finally, compared with those by a homogenous layer, the higher number of resonance peaks formed by the metaporous layer enhance its absorption performance over a broad range of frequencies. Because the proposed metaporous layers has the

subwavelength periodicities, it is valid to develop a theoretical model based on the effective medium theory. The model accurately described the physics of metaporous layers in various configurations outperforming a homogeneous porous layer of the same thickness.

The metaporous layer presented in section 3.4 is composed of a porous layer and horizontal rigid partitions with various lengths. As the inserted horizontal rigid partitions form the side-branch resonators along the wave propagation direction in the porous layer, the multiple slow wave propagations were generated. The absorption enhancement by the resulting metaporous layer, especially at the lower frequency range, is shown to be attributed to multiple slow waves formed over the full layer thickness. For a 3-cm thick layer of a selected porous medium considered in this study, the absorption coefficient value reached almost 0.9 for frequencies approximately starting from 1.4 kHz, which is substantial improvement when compared with the value of 0.56, the absorption coefficient of the nominal porous layer above 3 kHz. Actually, the increased absorption coefficient over a wide frequency band is due to the combined effects of the multiple slow waves and local resonance motions confined in certain regions of the metaporous layer by negative effective bulk moduli. The parametric studies of the metaporous layer suggested that the sound absorption performance of the proposed metaporous layer can be further tailored by controlling the geometric parameters of the inserted rigid partitions.

Therefore, optimization techniques [58], [59] can be used for engineering of metaporous layers to realize desired performances

CHAPTER 4.

ACOUSTIC METAMATERIALS

FOR SOUND TRANSMISSION

REDUCTION

4.1 Chapter overview

This chapter is dedicated to tackle a sound transmission problem through an acoustic medium. The works on the transmission control can be classified into two categories; enhancement and the suppression of the transmitted sound waves. The suppression of the transmitted waves requires impedance mismatching of the media. Generally, the use of solid bodies whose impedance is greater than the surrounding medium is known to be effective for the suppression of the sound waves. However, because the waves in the low frequency range, which have very long wavelengths, are hard to block with thin layers, the thicker layers whose dimension is comparable to the wavelength should be installed.

To overcome this limitation, various acoustic metamaterials were proposed [2], [6], [9], [77]. The proposed acoustic metamaterials are designed with membranes and solid cores or boundaries to generate resonance modes whose wavelength at the corresponding resonance frequency is much longer than the dimension of the structure. However, the acoustic metamaterials designed with membranes are still not practical to use for the real application because of the weak stiffness of the membranes. In addition, the membrane-type metamaterials cannot be used when the introduction of the holes are needed for the purpose of ventilation, which is frequently required in practical use. The acoustic metamaterials made of solid layer with periodic holes were proposed as well. However, their main purpose is focused on the enhancement of transmission by resonant transmission phenomena and other exotic performance originated from periodicity and only few works were conducted for the suppression purpose.

Therefore, in this chapter, the acoustic metamaterials for the transmission reduction will be presented. The proposed acoustic metamaterials are designed to have holes to allow a flow through the medium. It will be shown that the proposed metamaterials enhance sound insulation performance in a low and broad frequency range by adopting elaborately-designed resonator based on multiple slow wave phenomena. In the following sections, the sound transmission through acoustic layer with holes will be investigated first. Based on the study, the newly-designed metamaterial will be proposed and its physical phenomena will be investigated by theoretical and

numerical modellings. Compared with the nominal configuration of the acoustic double layer with holes, the superior performance of the proposed metamaterial will be confirmed.

4.2 Sound transmission through acoustic layer with holes

The use of solid bodies is generally effective at blocking the transmission of sound. However, for the purpose to exhaust heat or to ventilate the room, the addition of void holes to the acoustic transmission layer is often necessary. As the holes permits the transmission of sounds, unwanted sound transmission could occur depending on the covering area. To successfully design a noise barrier considering the holes, it requires comprehensive understanding of the system and its physics of the wave propagation. Therefore, in this section, a general review on the acoustic metamaterials designed by solid layer and periodic holes will be introduced also with the physical mechanism of the transmission enhancement or suppression.

In the fields of acoustic metamaterials, transmission through a layer with periodic holes were widely investigated to find extraordinary physical phenomena. The studies showed that the excitation of Fabry-Pérot resonances in the holes along the thickness realize high transmission at specific frequencies [78]. In addition to the Fabry-Pérot resonances, suppression of transmission (Wood's anomalies) and

extraordinary transmission were observed when the wavelengths are around the periodicity of the holes [79]–[81].

More recently, researchers found that sound transmission in certain frequency range can be suppressed when the acoustic double layers with periodic holes [82]. The so-called acoustic double-fishnet metamaterial, named after the shape of the structures, support a stop band, displaying a negative bulk modulus. The stop band appears due to a resonance mode between the adjacent layers, whose resonance frequency is dictated by the pitch of hole arrays. The controllability of the stop band has been investigated by adjusting a gap [83], [84], misaligning [85], [86] and by changing the shape of holes to Helmholtz resonators [87]. However, the considered frequency range of the above works lies in a high frequency range, even to ultrasound, to be used for practical purpose. There has been a study that considered audible frequency range [88], however, it requires large space to install because it only considers the basic concept in Ref. [82].

Before designing the metamaterials, the sound transmission performance of acoustic double layer will be presented. Figure 4.1(a) shows a schematic configuration of acoustic double layer. The thickness of layers is 1.0 mm and they are spaced 1.0 cm apart. The acoustic layers have periodic rectangular holes whose periodicity is in subwavelength scale in the frequency range considered. Figure 4.1(b) presents sound transmission performance of the considered acoustic double layer. From the

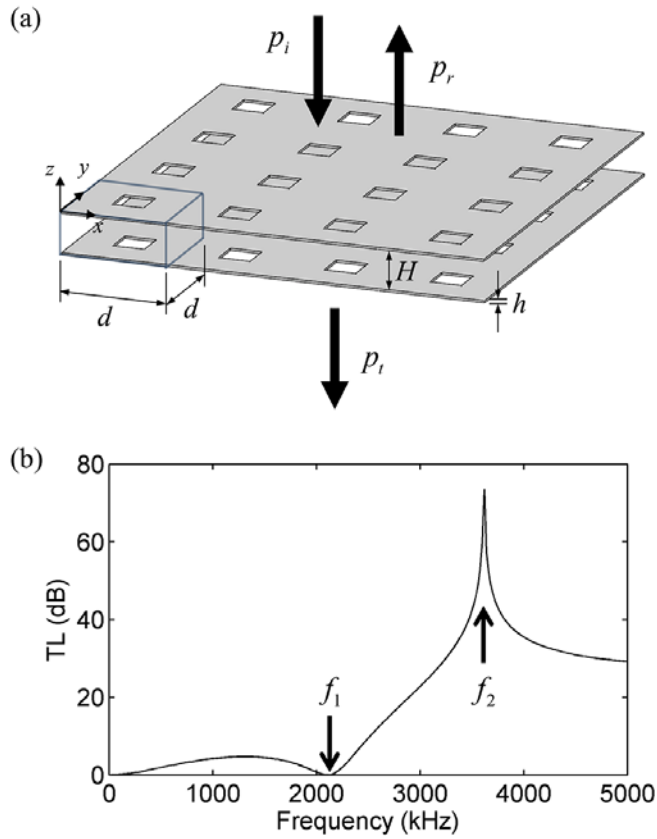


Fig. 4.1 (a) Acoustic double layer with periodic rectangular holes. (b) The sound transmission through the acoustic double layer in (a).

transmission loss (TL) graph, it is observable that the high frequency performance is rather ensured, on the other hand, the performance is very poor in the low frequency region. This work aims to improve low frequency performance of the acoustic double layer. In order to do that, the acoustic behavior of the acoustic double layer will be analyzed first.

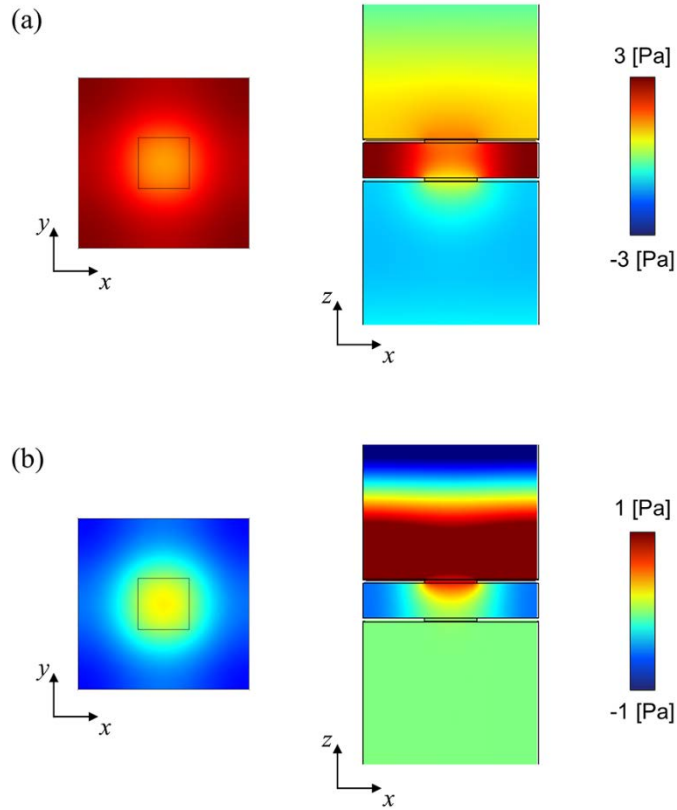


Fig. 4.2 Acoustic pressure fields in the xy and zx plane of the unit cell at the frequencies (a) f_1 and (b) f_2 denoted in Fig. 4.1(b).

In the graph, two distinct features can be observed. The first one is a resonant transmission when the TL becomes zero, denoted as f_1 in the figure. At this resonance frequency, the bulk resonance related to the volume of air in the gap is occurred, similar to Helmholtz resonance. Figure 4.2(a) shows acoustic pressure fields in the unit cell at f_1 . The left-hand side figure shows cross-sectional view in the xy plane and the right-hand side figure, in the zx plane, which sliced at the center

of the unit cell. The pressure field between the two layers are in the same phase, which confirms the bulk resonance mode.

The second one is a transmission loss peak at frequency f_2 . This transmission peak is related to the resonance phenomenon in the xy plane between the two acoustic layers. As shown in Fig. 4.2(b), acoustic pressure at this frequency has maximum amplitude at the ends of the unit cell and has near zero value around the hole. The sound transmission is suppressed due to the destructive interferences between the waves propagating along the wave incident direction and the waves trapped between the acoustic two layers. Therefore, it is observable that the acoustic pressure in the transmitted side of the right-hand side figure of Fig. 4.2(b) is zero.

This phenomenon is similar to the transmission problem of an acoustic duct with side branch resonators, commonly used for noise control in ducts [89]–[91]. The main difference between the acoustic double layer with holes and the duct problem is the presence of discontinuity of the wave propagating area. Especially, the transmission problem considered here is under assumption of normal incidence and subwavelength periodicity, acoustic response of the entire system is almost similar to that of the unit cell itself embedded in a rectangular duct. When the waves propagate in the rectangular duct, they go through abrupt change of propagating area on the top and bottom surface of the layers. Therefore, the transmission is affected by both of the effect of side resonator and the area change whereas the transmission

is affected only by the effect of side resonator in the case of acoustic duct. However, the important thing is that the acoustic phenomenon at the frequency f_2 can be interpreted in a similar manner for the case of acoustic duct.

Based on the findings presented above, it is conceivable that the low frequency performance can be improved when the resonance frequency of f_2 can be shifted to low frequency range. To suppress single tone of transmitted wave is relatively easy; one can add mass effect to the holes to form Helmholtz resonators [87], or elongate the wave path in the xy plane by using coiling-up method [11]. However, the low frequency, broadband transmission control is not easily achieved. To enhance broadband performance in acoustic ducts, serial arrangement of multiple resonators are commonly used [92], [93]. This strategy also may be adopted to reduce sound transmission through the acoustic double layer. However, provided that the dimension of the unit cell and hole are already defined, the design of multiple resonators would not be easy because it would require considerably large space to add multiple resonators. Therefore, it is desirable to design an acoustic device in a compact space to have multiple resonances in order to efficiently reduce transmitted sound waves.

4.3 Metamaterial resonators for transmission reduction

For this purpose, metamaterial resonators inserted in the acoustic double layer is proposed. The metamaterial resonators are designed to have resonance modes in low frequency range to enhance the sound insulation performance of the considered acoustic double layer. Figure 4.3(a) shows a unit configuration of the double layer with metamaterial resonator. The unit cell will be placed infinitely along the x and y direction with a subwavelength period d . In the gap between the two acoustic layers, acoustically rigid partitions are inserted to form multiple quarter-wavelength resonators. Figures 4.3(b) and 4.3(c) show examples of the resonator configurations. The partitions can be placed as in Fig. 4.3(b) to form four planar resonators in the xy plane and also can be placed as in Fig. 4.3(c) to form two planar resonators for their own target performances. The red arrows in the figures indicate the entrances of the resonators. The presented metamaterial resonator has similar structural shapes with the metaporous layer with multiple slow waves in previous section 3.4. Thus, the physical phenomena related to the multiple slow waves can be generated in the metamaterial resonator.

In the following subsections, design issues of the metamaterial resonators will be discussed first. After then, theoretical model to represent the acoustic performance of the proposed system will be derived. Finally, the acoustic performances of the proposed system obtained by theoretical and numerical methods will be shown.

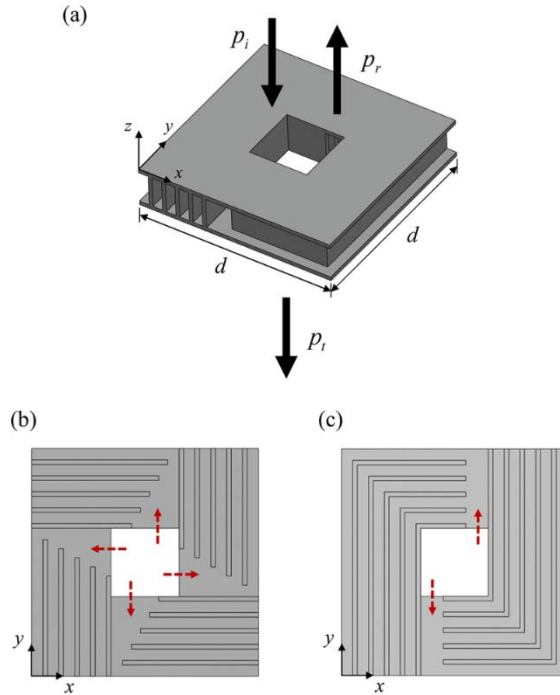


Fig. 4.3 (a) The unit cell configuration of the double layer with multiple slow wave resonator. The examples of the resonators are shown in (b) and (c).

4.3.1 Design issues on the metamaterial resonators

In Section 3.4, it was shown that the multiple slow waves can be successfully generated by inserting rigid partitions of various lengths which are placed perpendicular to the wave incidence to form multiple side resonators. The outstanding broadband sound absorption performance of the metamaterial layer comes from combination of the global resonances which are generated over the thickness of the porous layer in effective regime and the local resonances generated

at the specific location of the side resonators.

The absorption problem in section 3.4 and the transmission problem in this section can make significant differences in the designing and the response of the acoustic waves. First of all, the installed direction of the multiple resonators and the wave propagation direction in the absorption and the transmission problem are different. In the absorption problem, it was important to elongate the effective thickness of the porous layer by installing the side resonators in the thickness direction. However, in the transmission problem, the elongation of the effective thickness would not be effective to suppress transmission. As it has been shown in section 4.2, the thickness of the layer is a parameter to determine the Fabry-Pérot resonances. Accordingly, the elongated thickness rather results in resonant transmission in lower frequency range. To effectively suppress the transmission, it is important to use the resonance phenomena in the xy plane, as the transmission loss peak at frequency f_2 of Fig. 4.2(b).

The dimension of the period d in the absorption problem was small to meet the condition of the subwavelength condition so that the metaporous layer can be represented as effective layers in one dimensional concept. On the other hand, in the considered transmission problem, the multiple slow wave side resonators can have longer dimension within the allowed dimension in the considered configuration because the slow waves to be used here are generated in the xy plane, perpendicular

to the wave incident. Once the subwavelength periodicity is satisfied in the xy plane, the actual dimension of the side resonators of the multiple slow wave resonator can be further elongated, by coiling up the path, as shown in Fig. 4.3(b).

Therefore, in the following, parametric studies based on numerical modeling will be performed to investigate the influence on the acoustic response of various dimensional configuration of the metamaterial resonator. It will be examined which acoustic modes dominate the sound transmission performance of the proposed system.

4.3.2 Parametric studies on the metamaterial resonator

Figure 4.4(a) presents a configuration of a waveguide sided by the metamaterial resonator (multiple slow wave resonator) in two dimensional xy plane. The configuration of the waveguide has differences from the acoustic double layer, but it is presented here to examine the physical phenomena more easily by simplifying the problem. Four configurations of the resonators are shown in Fig. 4.4(b). In the multiple slow wave resonators, acoustically-rigid partitions of length L_i are inserted to form quarter-wavelength side resonators. To avoid confusion, the multiple slow wave resonators are called as ‘resonators’ and the quarter-wavelength resonators in the multiple slow wave resonators are called as ‘inserted resonators’. Likewise, the waveguide will be called as ‘waveguide’ and the waveguide section in

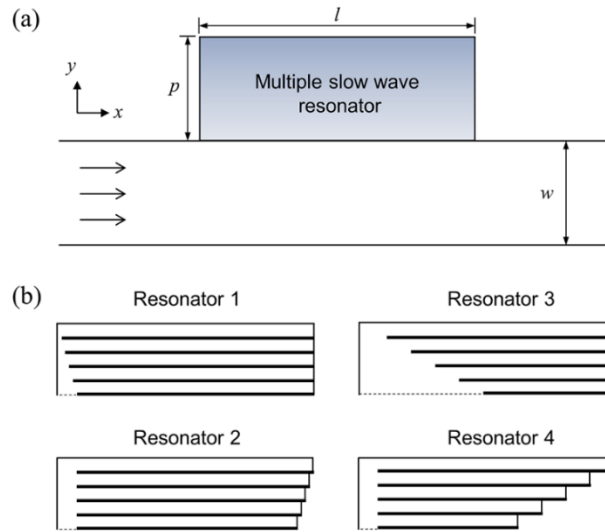


Fig. 4.4 (a) The configuration of a waveguide sided by the multiple slow wave resonator in two dimensional xy plane. (b) Four configurations of the resonators considered for the study.

the multiple slow wave resonators will be called as ‘inserted waveguide’.

To investigate the influence of the gradual variation of the partition length, two resonators (resonators 1 and 2) are designed to have the partition lengths of small variation and the other two resonators (resonators 3 and 4) are designed to have the partition lengths of large variation. The width of the waveguide w is set to be 3.0 cm, thus, the waves propagate in the waveguide remain the plane-wave propagation in the frequency range up to 5700 Hz. The geometric parameters of the resonators are set to be $p = 10$ cm, $l = 3.0$ cm. The shortest length of the rigid partition is 9.0 cm

and 4.0 cm for the resonators 1,2 and the resonators 3,4, respectively. The lengths of the partitions increase linearly along the y direction. For the resonators 1 and 3, the rigid partitions are aligned to the right side, as same as in the configuration for the multiple slow waves in Section 3.4. For the resonators 2 and 4, the partitions are aligned to the left side so that the cross-sectional area of the inserted waveguide remains same.

Figures 4.5 present transmission loss through the waveguide in Fig. 4.4(a) with the resonators 1 and 2. Figure 4.5(a) is the result of the waveguide with the resonator 1

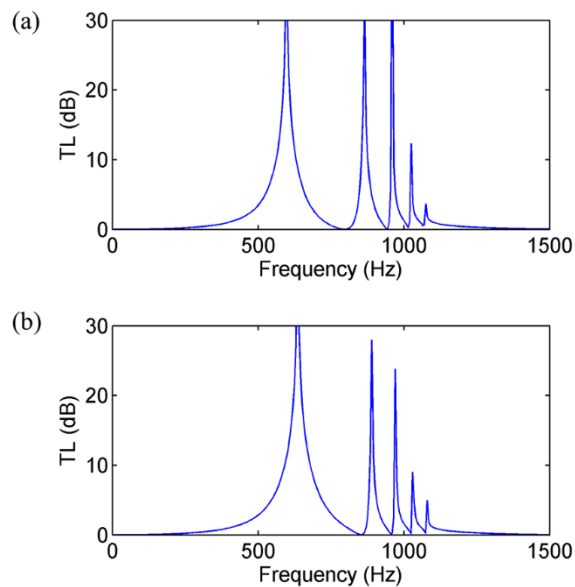


Fig. 4.5 The transmission loss through the waveguide in Fig. 4.4(a) with (a) the resonators 1 and (b) the resonator 2.

and Fig. 4.5(b) is with the resonator 2. The transmission loss graph in Figs. 4.5(a) and (b) have similar shape except slight differences of the peak frequencies. In Fig. 4.6, the velocity fields of the waveguide with the resonator 1 and 2 are presented at the transmission peak frequencies in Fig. 4.5. The velocity profiles demonstrate that the transmission peaks are from the global resonances along the y -directional dimension of the side resonator. The first peak is for the quarter-wavelength resonance for the thickness p with the slow wave velocity, and the second peak is for the three quarter-wavelength resonance, and so on. Similar to the multiple slow waves in Section 3.4, the active region for the resonances move to the region with the high-frequency resonator, i.e., the layer with shorter partition length.

It also shows that the transmission peaks by the inserted side resonators are not observable, whereas the local resonances of the inserted resonators are distinctive especially when the porous material is not used in section 3.4. It comes from the differences of the structural shape where the waves go through. In the absorption problem, the propagating incident waves meet the inserted resonator directly therefore the reflected waves are influenced directly from the inserted resonator. However, in the transmission problem, the incident waves do not encounter the inserted resonators directly, the destructive interference occurs only after the waves propagated into the resonator came out to the waveguide.

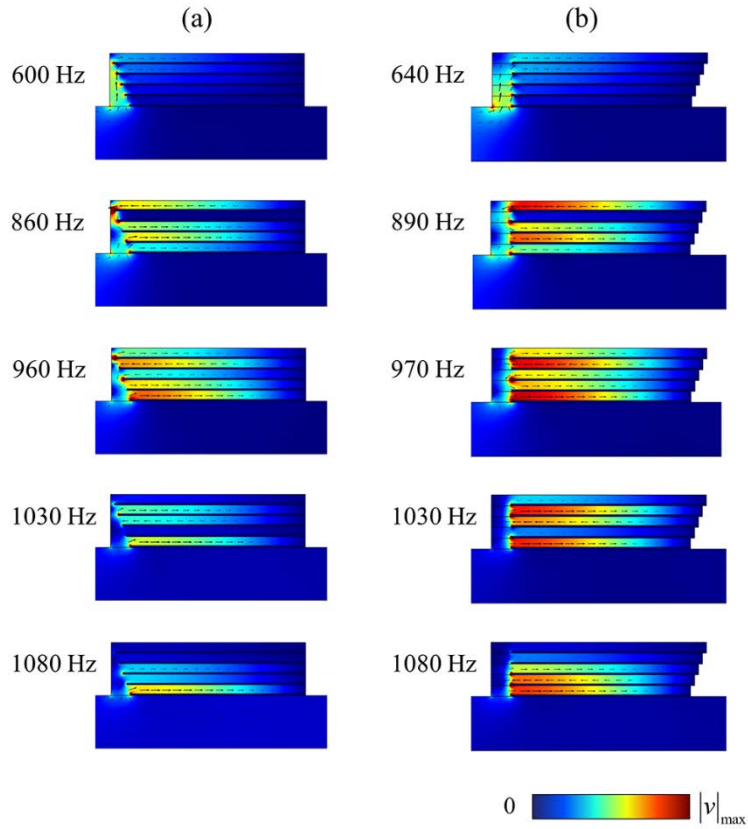


Fig. 4.6 The velocity fields of the waveguide with (a) the resonator 1 and (b) the resonator 2 are presented at the transmission peak frequencies in Fig. 4.5(a) and (b), respectively. The corresponding peak frequencies are written on the left-hand side of each figure.

In Fig. 4.7, the transmission loss graphs of the waveguide with the resonators 3 and 4 are shown in (a) and (b), respectively. The magnitude of the velocity fields at the lowest five peak frequencies are also shown in Fig. 4.8(a) for the waveguide with the resonator 3 and Fig. 4.8(b) for the waveguide with the resonator 4. The noticeable

thing is that the waves are confined at each inserted resonator, distinctive from the velocity fields in Fig.4.6. This phenomenon attributes to how steeply the lengths of the rigid partitions are changed. Likewise, in Section 3.4, the waveguide region of the resonator and the inserted resonators can be modelled as an effective layer. Then in the case when the lengths of the partitions change steeply, the effective medium properties also vary steeply along the y direction. Therefore, the local behavior of the inserted resonators become stronger than the global behavior along the y direction in the effective multilayer.

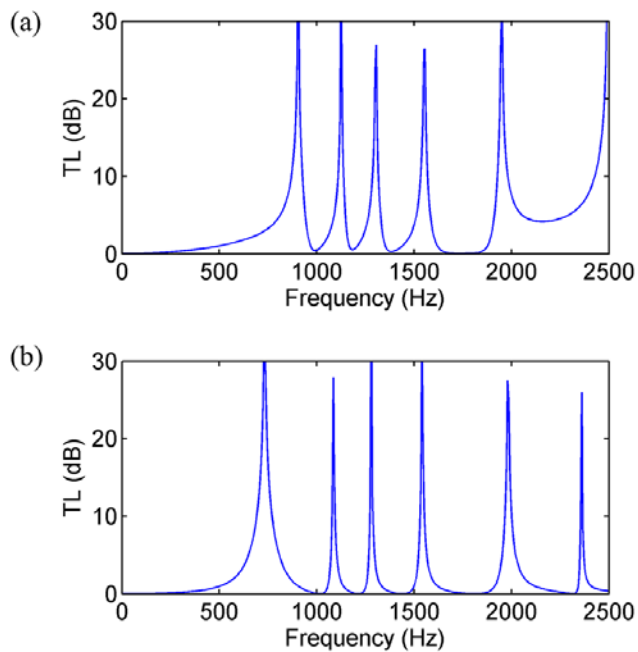


Fig. 4.7 The transmission loss through the waveguide in Fig. 4.4(a) with (a) the resonators 3 and (b) the resonator 4.

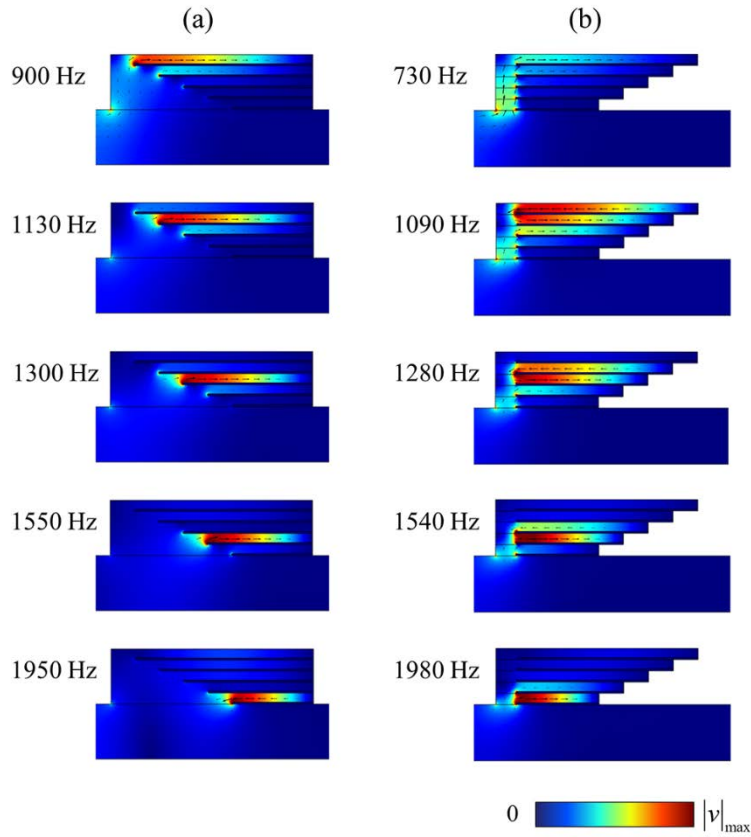


Fig. 4.8 The velocity fields of the waveguide with (a) the resonator 3 and (b) the resonator 4 are presented at the transmission peak frequencies in Fig. 4.7(a) and (b), respectively. The corresponding peak frequencies are written on the left-hand side of each figure.

Figure 4.8(a), the velocity fields of the resonator 3, also shows that the waves are more confined at each inserted resonator whereas there are interactions between the neighboring inserted resonators for the resonator 4. It is due to the different alignment of the rigid partitions in the resonators 3 and 4. For the resonator 3, the

partitions are aligned to the right side and the cross-sectional area of the waveguide in the resonator become smaller along the y direction. The waves propagate from the lower part are blocked as the partition lengths increase, therefore, the waves are confined in each inserted resonator. For the resonator 4, the cross-sectional area of the inserted resonator remains the same, which enables the interaction with the neighboring inserted resonator. The different of the cross-sectional area of the inserted waveguide also influence on the peak frequencies of the transmission loss curve. The first peak frequency, for example, of the resonator 3 is higher than that of the resonator 4. As it can be seen in the velocity fields, the waves with the resonator 3 is directly influenced by the longest inserted resonator that is placed on the top of the configuration. However, the first peak frequency of the resonator 4 is determined by the sum of the wave propagation length in the inserted waveguide and the length of the inserted partition. In addition to that, the interaction between neighboring inserted resonators also influences on the peak frequencies [93].

The studies presented above provide useful information in designing and understanding the metamaterial resonators. The engineers may prefer to design the resonator by using the global resonance phenomena or by using the local resonance phenomena in the metamaterial resonators. Based on the results above, a proper choice of the length variations of the rigid partitions should be considered to design the metamaterial-based structures for desired purpose.

4.3.3 Theoretical model of the proposed metamaterial

By using transfer matrix method, the performance of the proposed metamaterial can be obtained analytically. A schematic of the theoretical model of the proposed metamaterials is shown in Fig. 4.9. Figure 4.9(a) presents three dimensional view of the unit cell and Fig. 4.9(b) is drawn as a 2 dimensional configuration for convenience. The sound pressure and the volume velocity of the incident (denoted as subscription i) and transmitted (denoted as subscription f) region are represented as

$$p_i = Ae^{-jk_0z} + Re^{jk_0z}, \quad v_i = \frac{1}{z_0}(Ae^{-jk_0z} - Re^{jk_0z}), \quad (4.1)$$

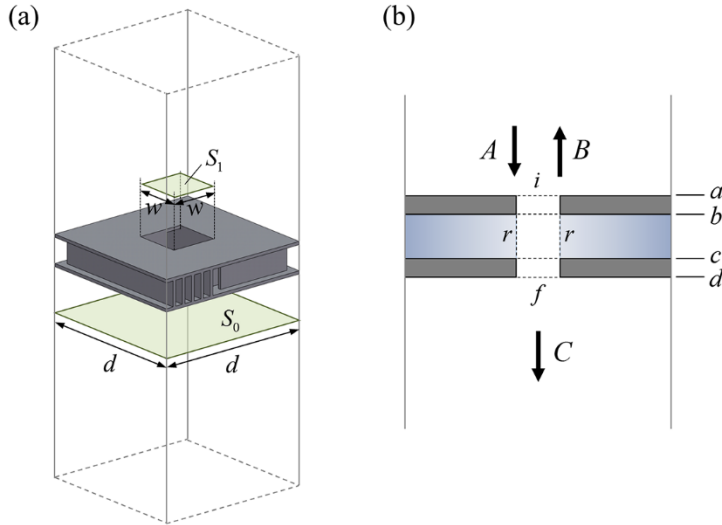


Fig. 4.9 The schematics of the theoretical model of the proposed metamaterials. (a) The three dimensional view of the unit cell. (b) The twodimensional configuration presented to help the understanding of the theoretical model.

$$p_f = T e^{-jk_0 z}, \quad v_f = \frac{1}{z_0} T e^{-jk_0 z}, \quad (4.2)$$

where A , R , and T are the magnitude of the incident, reflected, and transmitted waves, respectively, and z_0 the acoustic impedance of the incident and transmitted region. Following the transfer matrix modelling introduced in section 2.5, the acoustic wave fields in the incident and transmitted region can be related by the total transfer matrix \mathbf{T} as below.

$$\begin{pmatrix} p_i \\ v_i \end{pmatrix} = \mathbf{T} \begin{pmatrix} p_f \\ v_f \end{pmatrix} = \begin{bmatrix} T_{11} & T_{12} \\ T_{21} & T_{22} \end{bmatrix} \begin{pmatrix} p_f \\ v_f \end{pmatrix}. \quad (4.3)$$

The total transfer matrix is constructed by multiplication of the transfer matrix that connects the wave fields at the positions a , b , c , and d in Fig. 4.9(b),

$$\mathbf{T} = \mathbf{T}_{ab} \mathbf{T}_{bc} \mathbf{T}_{cd}. \quad (4.4)$$

When the waves propagate through the first layer, the area where the waves propagate is contracted from S_0 to S_1 . In this case, the effect of elongated thickness due to the radiation impedance should be considered. Thus, effectively, the thickness of the layer can be represented as $t_e = t + \Delta t$. Following the results of Ref. [94], the end correction for a rectangular aperture is represented as

$$\Delta t = 0.85w \cdot (1 - 1.25\sqrt{\phi_0}), \quad (4.5)$$

where ϕ_0 is fraction of open area, S_1/S_0 . Then the transfer matrix \mathbf{T}_{ab} becomes

$$\mathbf{T}_{ab} = \begin{bmatrix} \cos(k_0 t_e) & j \frac{z_0}{\phi_0} \sin(k_0 t_e) \\ j \frac{\phi_0}{z_0} \sin(k_0 t_e) & \cos(k_0 t_e) \end{bmatrix}. \quad (4.6)$$

The transfer matrix of the proposed side resonators can be obtained by using the impedance of the resonator. At point 1, the conditions for the pressure and the volume velocity are

$$p_B = p_r = p_C, \quad (4.7)$$

$$S_0 v_B = n S_r v_r + S_0 v_C, \quad (4.8)$$

where S_r means cross sectional area of the entrance of the resonator where acoustic waves flows into and n is the number of the resonators. The velocity at the entrance of the resonators v_r is represented as p_r/Z_r , by the definition of the impedance, therefore, Eq. (4.8) becomes

$$v_B = \frac{n S_r}{S_0 Z_r} p_C + v_C. \quad (4.9)$$

From Eqs. (4.7) and (4.9), the transfer matrix \mathbf{T}_{bc} is represented as

$$\mathbf{T}_{bc} = \begin{bmatrix} 1 & 0 \\ \frac{nS_r}{S_0 Z_r} & 1 \end{bmatrix}. \quad (4.10)$$

The impedance of the resonators, Z_r , can be obtained by using a similar procedure to obtain the surface impedance of the metaporous layer with multiple slow waves in Section 3.4. The detailed configuration is changed, but the surface impedance of the resonator is obtained in the same manner by regarding the acoustic structures in the resonator as a multilayer of effective layers with different material properties. Figure 4.10(a) shows a top view of one of the resonators. Although the acoustic paths made by partitions are bent, they can be considered as a straight one with the same length as shown in Fig. 4.10(b).

When sound propagates in structures and geometries with small dimensions, the sound waves become attenuated because of thermal and viscous losses. Therefore, the dissipative effect due to the thermal and viscous losses should be accounted for describing the waves in the narrow chambers. Following the equations in Eq. (2.41) and Eq. (2.54) in section 2.3, the equivalent acoustic model for the rectangular tubes of the cross-sectional dimension s are represented as

$$\rho_c = \frac{\rho_0}{1 - \tanh\left(\frac{s}{2}\sqrt{j\frac{\rho_0\omega}{\mu}}\right) \Big/ \left(\frac{s}{2}\sqrt{j\frac{\rho_0\omega}{\mu}}\right)}, \quad (4.11)$$

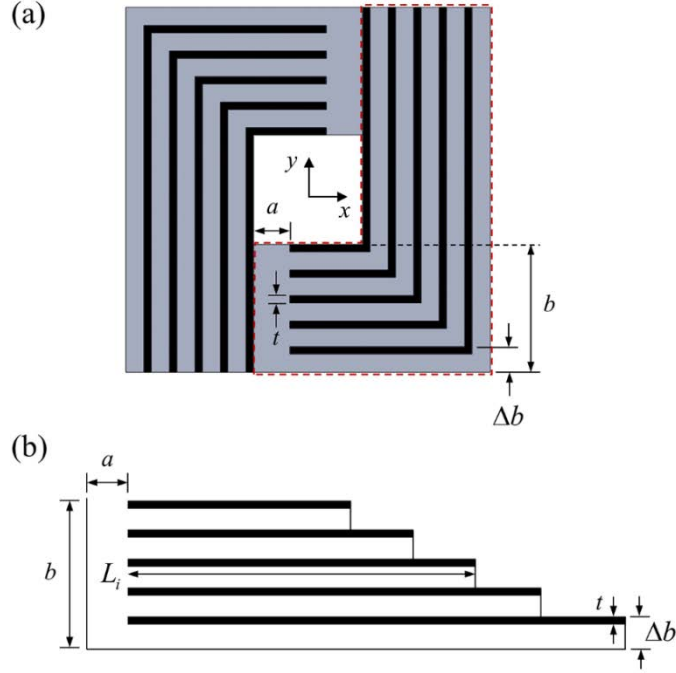


Fig. 4.10 (a) A sliced top view of the presented metamaterial. The one resonator indicated as red dashed line can be analyzed as the configuration in (b).

$$\kappa_c = \frac{\gamma P_0}{1 + (\gamma - 1) \tanh \left(\frac{s}{2} \sqrt{j \frac{\rho_0 \text{Pr} \omega}{\mu}} \right) / \left(\frac{s}{2} \sqrt{j \frac{\rho_0 \text{Pr} \omega}{\mu}} \right)}. \quad (4.12)$$

For the considered configuration, the cross-sectional dimension s becomes a for the waveguide and $(\Delta b - t)$ for the side resonators. The acoustic medium properties of in the waveguide and in the side resonators are represented with subscription w and s , respectively, as ρ_w , κ_w and ρ_s , κ_s . The wave velocity and the wavenumber in the waveguide and the side resonators are then obtained as $c_w = \sqrt{\kappa_w / \rho_w}$,

$$c_s = \sqrt{\kappa_s / \rho_s} \quad \text{and} \quad k_w = \omega / c_w, \quad k_s = \omega / c_s.$$

By adopting the approach used in Section 3.4.1, effective wave number and effective characteristic impedance of the effective layer from the bottom can be obtained as

$$k_i^e = \sqrt{k_w^2 + \eta \frac{\rho_w k_s}{\rho_s a} \tan(k_s L_i)}, \quad (4.13)$$

$$z_i^e = \frac{\omega \rho_0}{k_i^e}, \quad (4.14)$$

where a is the width of the resonator entrance, L_i is the length of the side resonator, and η is the volume fraction of the air in each side resonator, $1 - t/\Delta b$. Also as in Section 3.4.1, the surface impedance on the effective layer i (Z_i^e) is obtained by successive relation of the surface impedances as

$$\begin{aligned} Z_1^e &= -jz_1^e \cot(k_1^e \Delta b), \\ Z_i^e &= z_i^e \frac{Z_{i-1}^e + jz_i^e \tan(k_i^e \Delta b)}{jZ_{i-1}^e \tan(k_i^e \Delta b) + z_i^e}, \quad (i = 2, 3, \dots, N). \end{aligned} \quad (4.15)$$

The transfer matrix \mathbf{T}_{cd} is equal to \mathbf{T}_{ab} due to the same geometry. Once the overall transfer matrix is obtained, transmission loss of the system can be found following the Eq. (2.72) as

$$TL = 20 \log \frac{1}{2} \left| T_{11} + \frac{T_{12}}{z_0} + T_{21} z_0 + T_{22} \right|. \quad (4.16)$$

4.3.4 Sound insulation performance of the metamaterial system

Figures 4.11-16 present the acoustic performance of some examples of the proposed metamaterials. In each figure, a cross-sectional view of the unit cell and wave velocities in the resonator are presented as well as the transmission loss of the considered metamaterial. The transmission loss curves are obtained by theoretical model described in section 4.3.2 and the results are validated by the numerical simulations. For the numerical simulations, finite element method of COMSOL Multiphysics 4.3 is used. To account the viscous losses in the cross-sectional areas in the numerical simulations, thermoacoustic analysis based on linearized Navier-Stokes equation should be considered. However, due to the high time cost of the thermoacoustic analysis, pure acoustic analysis without viscous losses are presented in Figs. 4.11-16. For the results obtained by the theoretical model, both results when the viscous losses are considered or not are presented to examine the effects of the viscous losses on the sound transmission through the metamaterial.

The metamaterials presented in Figs. 4.11-15 assumed to be placed in a rectangular tube whose dimension is 50 mm by 50 mm. The tube is assumed to be sided by hard walls. The frequency range considered here is up to 3000 Hz. Therefore, only

fundamental acoustic mode is propagative in the tube. The holes on the acoustic layer have dimension of 15 mm by 15 mm and placed on the center of the layer, thus the opening ratio is 9 %. The thickness of the top and bottom layers are the same as 1.0 mm and they are spaced 1.0 cm apart. Therefore, total thickness of the metamaterial becomes 1.2 cm. The rigid partitions are inserted between the layers and the width of the partitions is set to be 1.0 mm. For the metamaterials presented here, the resonators are equally divided to five regions by the rigid partitions. Therefore, b and Δb are 17.5 mm and 3.5 mm. The width of the inserted side resonators becomes 2.5 mm.

The metamaterial in Fig. 4.11(a) has four resonators of which lengths of rigid partitions are the same so as to form identical inserted side resonators in the resonator. The length of rigid partitions is set to be 28 mm. The characteristic length of the inserted resonators is directly determined by the length of the rigid partitions. The medium in the resonator can be modelled as a single effective medium and the resonator has one type of slow wave as shown in Fig. 4.11(b). The peaks in the transmission loss in Fig. 4.11(c) attribute to the resonances by the slow wave, formed globally from the resonator entrance to the boundary of the unit cell. This global resonance mode by the slow wave allows low frequency peak by elongating effective dimension of the resonator. As the slow waves are generated, the dimension of the resonator b is elongated to b^* . The first peak is the quarter-wavelength resonance $b^* = \lambda^*/4$, the second one is $b^* = 3\lambda^*/4$, and so on as in Section 3.4. For example,

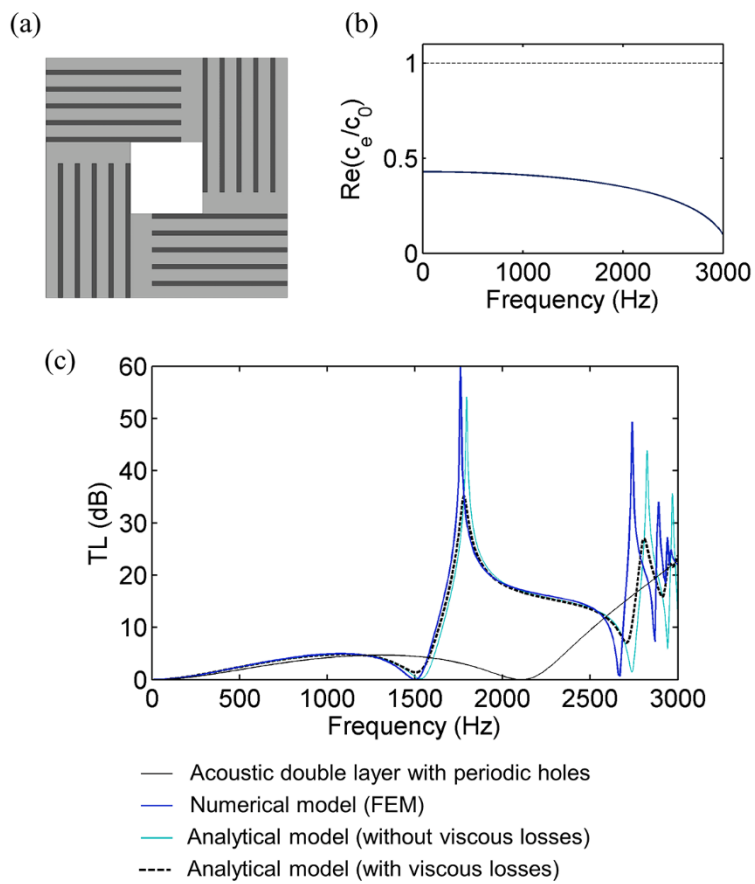


Fig. 4.11 (a) The configuration of the considered metamaterial. (b) The effective sound velocity in effective medium filling the resonator normalized to the sound velocity in air (c_0). (c) The transmission loss through the considered metamaterial.

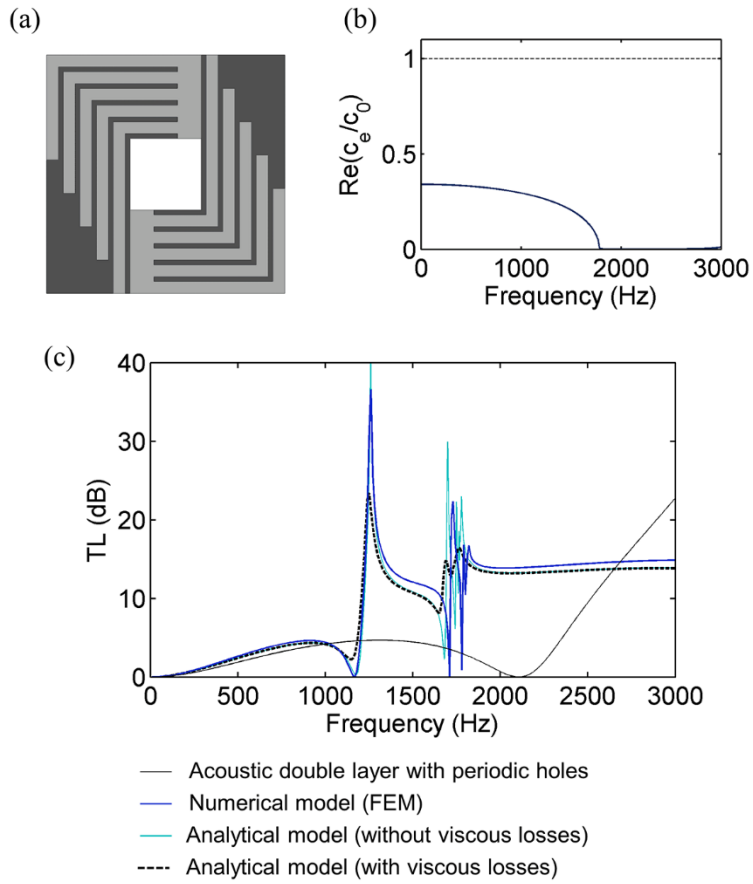


Fig. 4.12 (a) The configuration of the considered metamaterial. (b) The effective sound velocity in effective medium filling the resonator normalized to the sound velocity in air (c_0). (c) The transmission loss through the considered metamaterial.

the effective wave velocity is $0.37c_0$ at the first peak 1780 Hz, which means that the dimension is elongated by a factor of $1/0.37 \cong 2.7027$. When it is compared with the resonance frequency of the original length b ($=1.75$ cm) that is $f_r = c_0/4b = 4885$ Hz, the peak frequency is reduced by $0.364 f_r$. Between the successive resonance frequencies, dips of transmission loss are occurred due to the anti-resonance phenomena. Note that the local resonance of the inserted resonator is not observed because the local resonance frequency is above the frequency range considered here.

The metamaterial shown in Fig. 4.12(a) is designed to have lower resonance frequency of the inserted resonators to generate slower waves compared to the metamaterials in Fig. 4.11. The rigid partitions are placed to make L shape to elongate the characteristic length of the inserted resonators and two resonators are formed by utilizing sparse space between the acoustic layers. Then the characteristic length of the inserted side resonators becomes 48 mm. Although the inserted resonators are bent but the acoustic behavior is the same as in the straight inserted resonators. Therefore, low frequency absorption peaks can be obtained as shown in Fig. 4.12(c). The peak value is small compared to the transmission loss peak in Fig. 4.11(c) and narrowband. This is because the acoustic response is affected by the number of parallel-coupled resonators. When more resonators are coupled in parallel, the transmission loss peaks tend to be high and broadband due to the change of

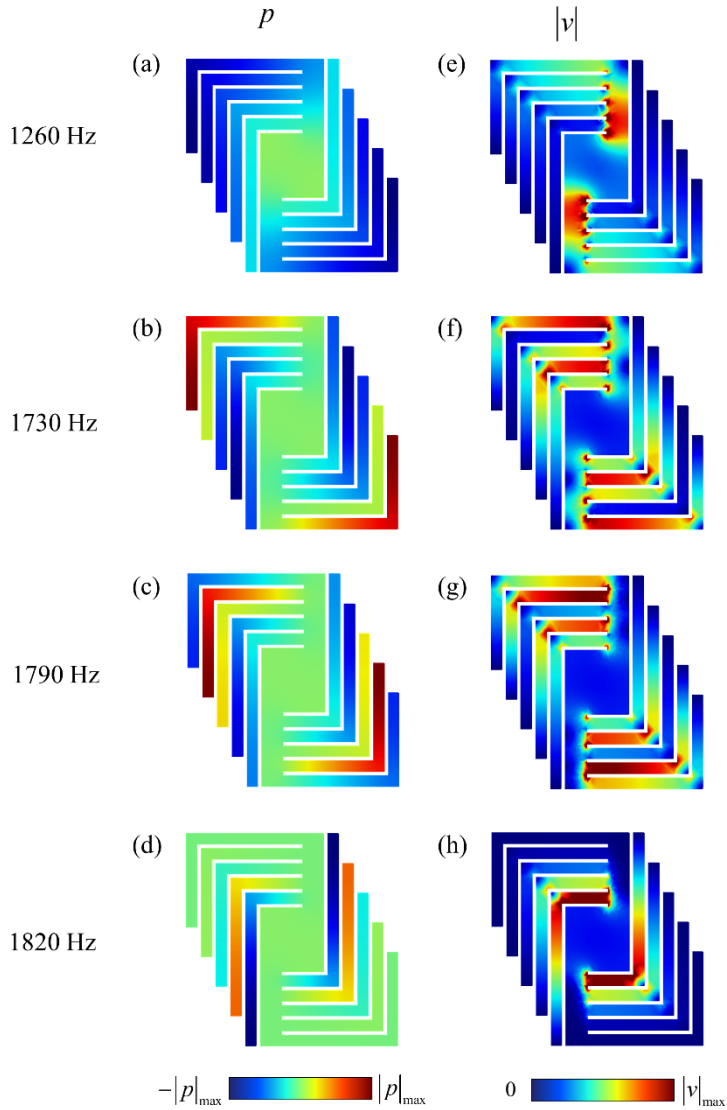


Fig. 4.13 The contour plots of the (a)-(d) acoustic pressure and (e)-(h) magnitude of velocities in the metamaterial presented in Fig. 4.12(a) at the transmission loss peak frequencies in Fig. 4.12(c). The corresponding peak frequencies are written on the left-hand side.

impedances [95], [96]. The resonance frequency of the inserted resonators considered here is present in the frequency range considered.

Figure 4.13 shows acoustic pressure (a-d) and velocity magnitude fields (e-h) in the metamaterial at the peak frequencies of the transmission loss curve in Fig. 4.12(c). There exist four transmission loss peaks including small peaks at 1260, 1730, 1790 and 1820 Hz. The local resonance frequency of the inserted resonators is 1800 Hz. While the waves in the resonator are scattered globally at the other frequencies, the waves at the frequency 1820 Hz are confined mostly at the one inserted resonator, which demonstrates that the transmission loss peak at 1820 Hz comes from the local resonance of the inserted resonator. As mentioned above, the wave fields at other peak frequencies form odd multiples of $\lambda^*/4$ in the resonator.

Figure 4.14 presents a metamaterial with varying lengths of rigid partitions. The average length is higher than the wave velocity in the resonator in Fig. 4.14(a). Therefore, the first peak frequency in the transmission loss curve in Fig. 4.14(c) is higher than the first peak frequency in Fig. 4.11(c). The use of multiple slow waves is not much effective in the configuration compared to the results in Fig. 4.11 because the frequency range considered here is rather low to make full use of the multiple slow waves for the present configuration.

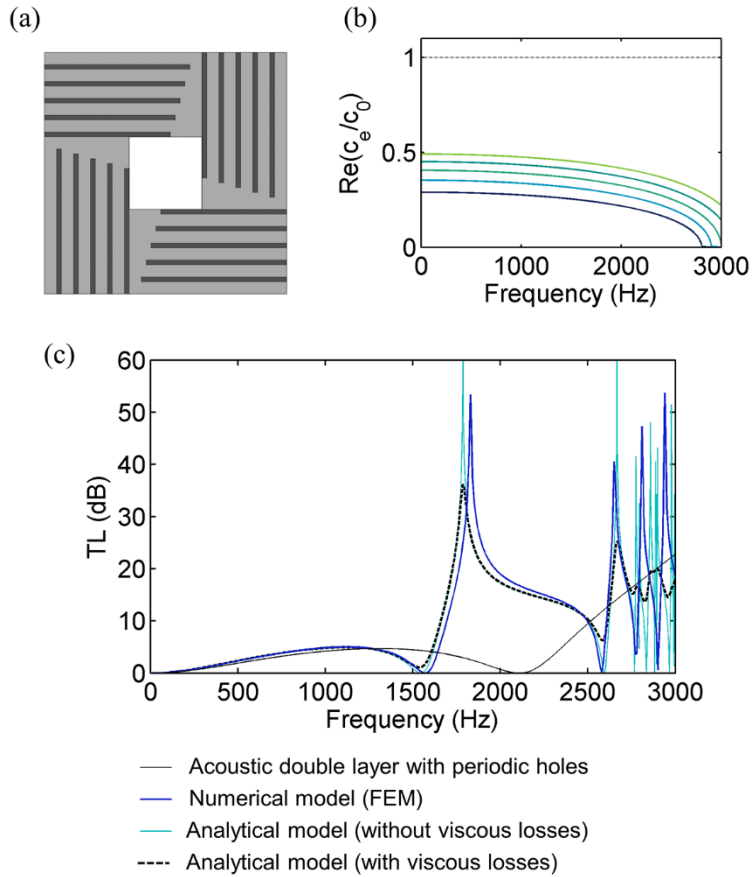


Fig. 4.14 (a) The configuration of the considered metamaterial. (b) The effective sound velocities in effective media filling the resonator normalized to the sound velocity in air (c_0). (c) The transmission loss through the considered metamaterial.

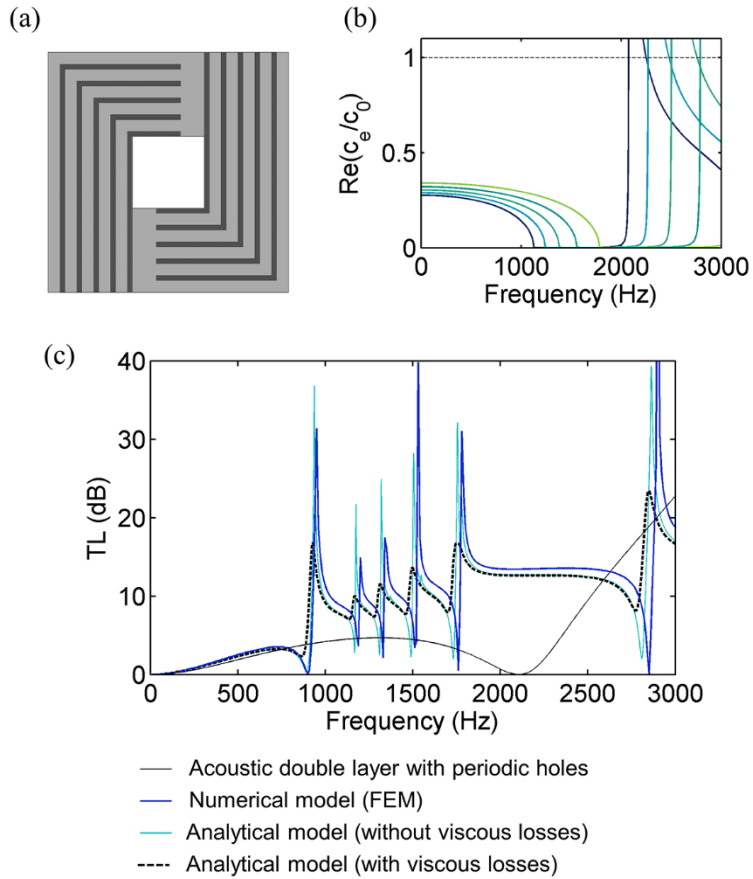


Fig. 4.15 (a) The configuration of the considered metamaterial. (b) The effective sound velocities in effective media filling the resonator normalized to the sound velocity in air (c_0). (c) The transmission loss through the considered metamaterial.

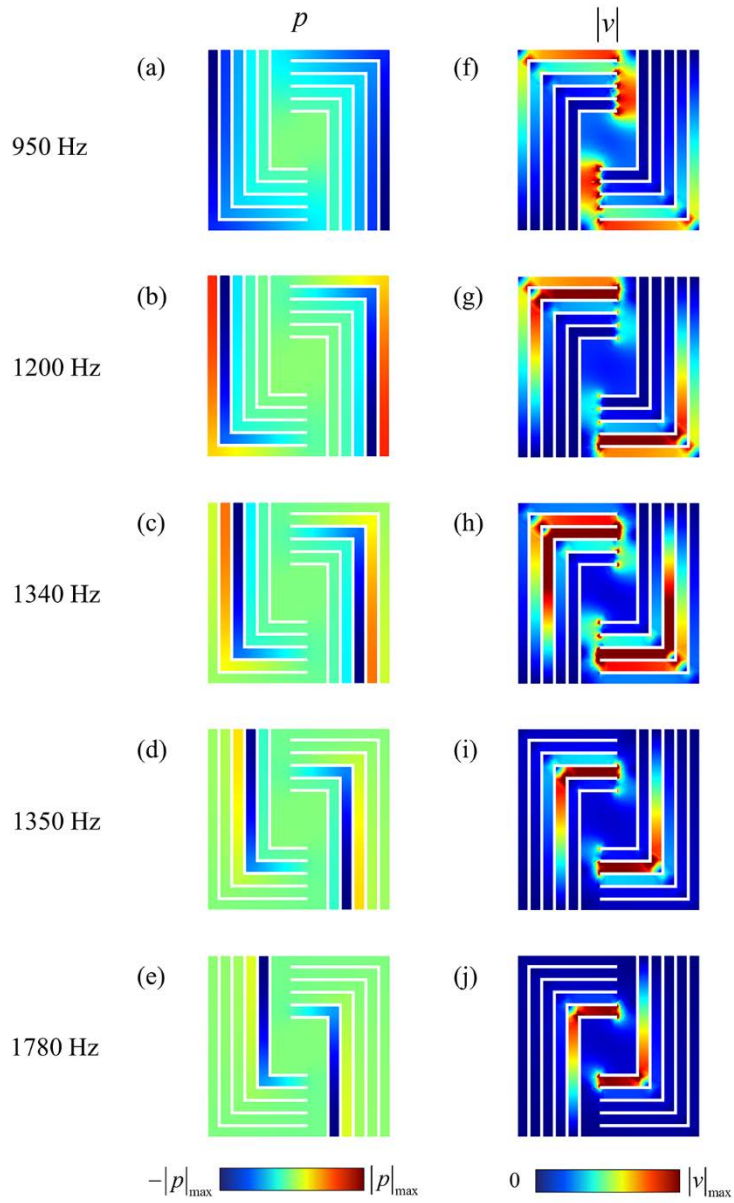


Fig. 4.16 The contour plots of the (a)-(e) acoustic pressure and (f)-(j) magnitude of velocities in the metamaterial presented in Fig. 4.15(a) at the transmission loss peak frequencies in Fig. 4.15(c).

The metamaterial in Fig. 4.15(a) also has multiple inserted resonators and the rigid partitions are placed to form L shape to lower the resonance frequencies of the inserted resonators as the metamaterial in Fig. 4.12. The characteristic lengths of the inserted resonators are 76 mm, 69 mm, 62 mm, 55 mm and 48 mm. The wave velocities of the effective media consisting the resonator are shown in Fig. 4.15(b). In the frequency range considered, the metamaterial allows several transmission peaks around 1000 Hz to 2000 Hz as shown in Fig. 4.15(c).

Figure 4.16 shows acoustic pressure (a-e) and velocity magnitude fields (f-j) in the metamaterial at the peak frequencies of the transmission loss curve in Fig. 4.15(c). It can be observed that the waves are usually confined at the inserted resonators, which means that the transmission loss peaks originate from the local resonances of the inserted resonators. As it is investigated in section 4.3, the variation of the characteristic lengths of the inserted resonators influence on the generation of the global resonance modes of the resonator. The length variation of the present metamaterial is 7 mm, thus each medium acts more independently rather than acts as a part of continuous medium of a layer. Therefore, the waves are trapped when the wave velocity is zero, at the local resonance frequency of the inserted resonator. However, the peak frequencies and the local resonance frequencies are different because the wave lengths are elongated while the waves pass through the inserted waveguide. For example, the waves need to travel the distance of $(b - \Delta b / 2)$ to reach the inserted resonator of the longest characteristic length.

The effects of the viscous losses can be observed by comparing the results with and without considering viscous losses. When the viscous losses are considered, the peak and the dip from the resonance and anti-resonances become smooth. This is because the imaginary parts of wave vector generated by viscous losses effect on the phase interference of the wave propagating through the holes and the one from the resonator.

The simulations conducted above are under the assumption of the infinite domain in the xy plane by imposing periodic boundary conditions on the edges of the unit cell along the x and y directions. However, in the practical applications, the space for the insulation panel is generally limited in a finite dimension. To check the applicability in the finite domain, the configurations in Fig. 3.17(a) that are composed of 4 and 9 unit cells, respectively, are considered. The 4-cell and 9-cell configurations are placed in the rectangular duct of dimension $2d \times 2d$ and $3d \times 3d$, respectively, whose outer boundaries are assumed to be hard walls. The acoustic performances of them are shown in Fig. 3.17(b) compared with the 1-cell configuration that is placed in a rectangular duct of dimension $d \times d$ in the same manner. The results show that the transmission loss values of all of the considered configurations are the same. For normally-incident sound waves, the hard wall boundary conditions on the unit cell edges are actually the same as the Floquet-Bloch periodic boundary conditions because the tangential components in the xy plane of the wave vector remains zero as long as the period of the structures are in a subwavelength scale. Therefore, there

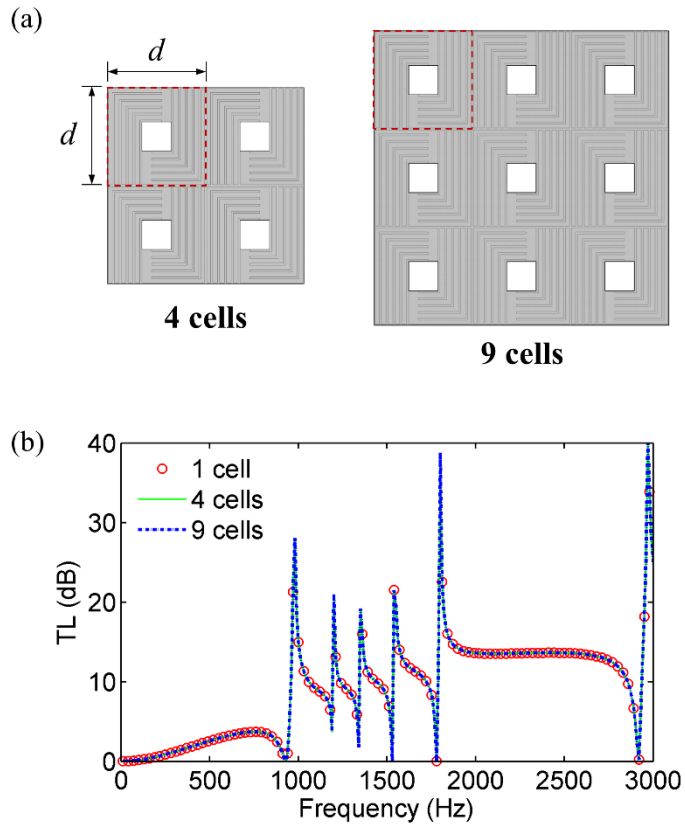


Fig. 4.17 (a) The cross section in the xy plane of the configurations composed of multiple unit cells. (b) The transmission loss curves obtained by finite element simulations using the configurations in (a).

is no difference in the results even the multiple unit cells are considered. However, it should be noted that the results can be different if oblique incidence is considered.

4.4 Experiments on the proposed acoustic metamaterials

This section presents experimental verification of the proposed acoustic metamaterials for sound transmission performance.

4.4.1 Experimental setup

The transmission experiments were conducted by using an impedance tube (Brüel & Kjaer's Transmission Loss Tube Kit Type 4206-T). With a circular impedance tube of 10 cm diameter, sound transmission in the frequency range 50 – 1600 Hz can be measured. Figure 4.18 shows a schematic diagram of the impedance tube for measuring sound transmission. A loudspeaker located on the left-hand side of the

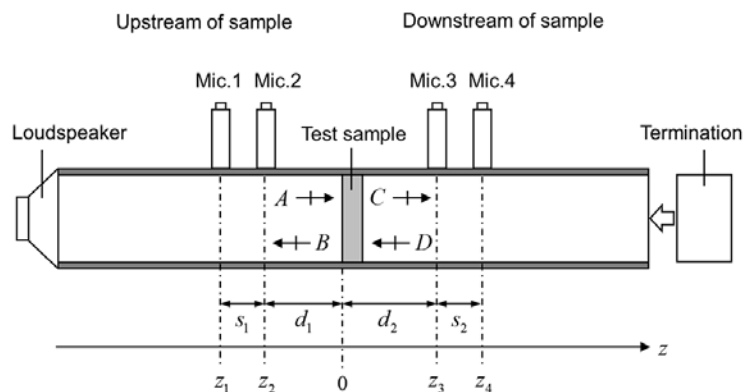


Fig. 4.18 Schematic diagram of the standing wave impedance tube for measuring sound transmission loss.

impedance tube shown in the figure generate one dimensional plane wave propagating along the z direction. At four measurement positions, microphones are mounted to measure sound pressure. Two microphones (mic. 1 and mic. 2) are mounted on the upstream of the sample at the positions z_1 and z_2 on the z axis indicated in the Fig. 4.18 and other two microphones (mic. 3 and mic. 4) are mounted on the downstream of the sample at the positions z_3 and z_4 . In the upstream part, the pressure and the velocity are given by

$$p(z) = Ae^{-jk_0z} + Be^{jk_0z}, \quad (4.17)$$

$$v_z(z) = \frac{1}{\rho_0 c_0} (Ae^{-jk_0z} - Be^{jk_0z}), \quad (4.18)$$

and in the downstream part,

$$p(z) = Ce^{-jk_0z} + De^{jk_0z}, \quad (4.19)$$

$$v_z(z) = \frac{1}{\rho_0 c_0} (Ce^{-jk_0z} - De^{jk_0z}), \quad (4.20)$$

where A and B indicate the amplitudes of the incident and reflected waves in the upstream part and C and D indicate the amplitudes of the transmitted and reflected waves in the downstream part. Using the measured pressures at the four microphones, Eqs. (4.17) – (4.20) can be rearranged in terms of the pressure amplitudes as

$$A = j \frac{p(z_1)e^{jk_0z_2} - p(z_2)e^{jk_0z_1}}{2\sin(k_0(z_1 - z_2))}, \quad (4.21)$$

$$B = j \frac{p(z_2)e^{-jk_0z_1} - p(z_1)e^{-jk_0z_2}}{2\sin(k_0(z_1 - z_2))}, \quad (4.22)$$

$$C = j \frac{p(z_3)e^{jk_0z_4} - p(z_4)e^{-jk_0z_3}}{2\sin(k_0(z_3 - z_4))}, \quad (4.23)$$

$$D = j \frac{p(z_4)e^{-jk_0z_3} - p(z_3)e^{-jk_0z_4}}{2\sin(k_0(z_3 - z_4))}. \quad (4.24)$$

When the perfect anechoic termination is fulfilled ($D = 0$), the transmission loss is directly obtained by $TL = 20 \log_{10}(|A/C|)$.

4.4.2 Experimental results and discussion

Figures 4.19(a) and (b) shows a schematic configuration and a photograph of the fabricated samples of the designed metamaterials for experiments, respectively. To conduct the experiment by using the circular-shaped impedance tube, the samples were made to have circular boundaries. Thus, the samples are made of as if the rectangular metamaterials of dimension $d \times d$, which are considered in this work, are inserted in the circular plate of a finite thickness. The fabricated samples are composed of three layers, layers A, B and A' as indicated in Fig. 4.19(a). The thickness of the layers and A', h , is set to be 1.0 mm, and the thickness of the layer

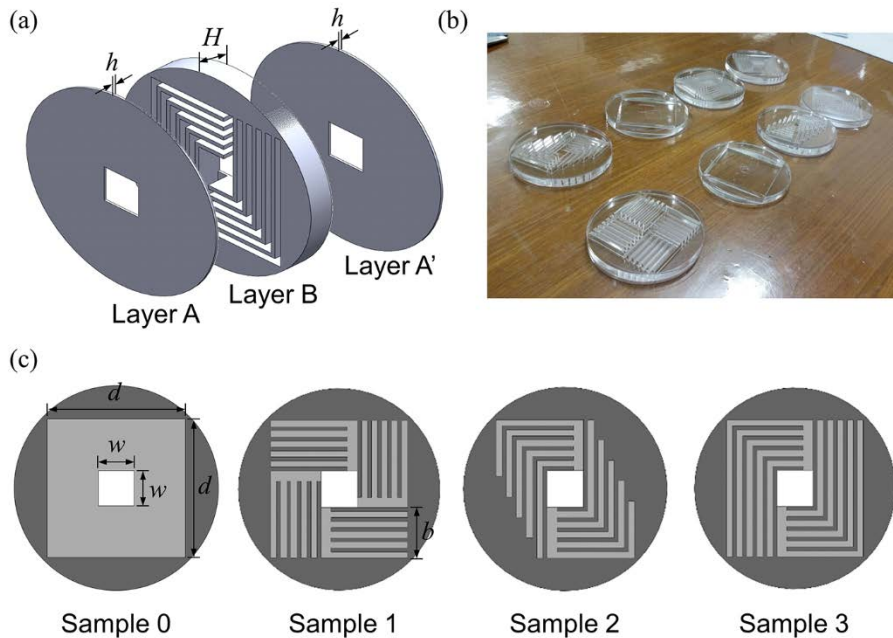


Fig. 4.19 (a) Designed metamaterials are fabricated by bonding three layers made of acrylic plates; Layer A, B, and A'. (b) Photograph of the fabricated metamaterials. (c) Cross sections of the fabricated samples.

B, H , is 10 mm. Therefore, the total thickness of the metamaterial is 12 mm. The metamaterials are made of acrylic plates manufactured via laser cutting. The three layers are fabricated separately and are attached by using adhesive glue. Figure 4.19(c) shows cross sections of four types of samples designed for experiments. The sample 0 is a nominal case, without the inserted metamaterial resonator. For all samples, sample 0 to 3, the dimension of the metamaterial and the rectangular hole are set to be $d = 68$ mm and $w = 18$ mm, respectively. Sample has four single slow wave resonators, sample 2 has of two single slow wave resonators, and sample 3 has

two multiple slow wave resonators. In layer B, the inserted waveguide length b becomes 30 mm for samples 1-3. The rigid partitions divide b equally to form inserted side resonators. The characteristic length L_i of the inserted resonators are 38 mm (sample 1), 63 mm (sample 2) and {103 mm, 93 mm, 83 mm, 73 mm, 63 mm} (sample 3), respectively.

The transmission loss curves obtained by the transmission experiments for the samples 0-3 are shown in Fig. 4.20 compared with those obtained by theoretical model presented in section 4.3.3. It is observable that the two results show good agreement with each other in general. However, the peak and anti-peak frequencies corresponding of the measured data slightly deviate the results predicted by the theoretical model. In addition, it is also observed that the overall transmission loss value, especially for the sample 1 and 2, and the transmission loss values at the peaks obtained by the experiments are lower than the ones by the theoretical model. The causes of these differences may come from several reasons. The main reason of the frequency deviation and the smaller value of peaks would be the error occurred in manufacturing process of laser cutting and bonding. Especially, because the layers A-B-A' are bonded manually, the glue left in the metamaterial cavity could have increased the viscous effect in the narrow waveguides or side resonators. The overall transmission difference can be attribute to a leakage of the sound waves. To insert the designed metamaterials in the impedance tube, the samples were fabricated to have a smaller diameter (99.5 mm) than the actual diameter of the impedance tube

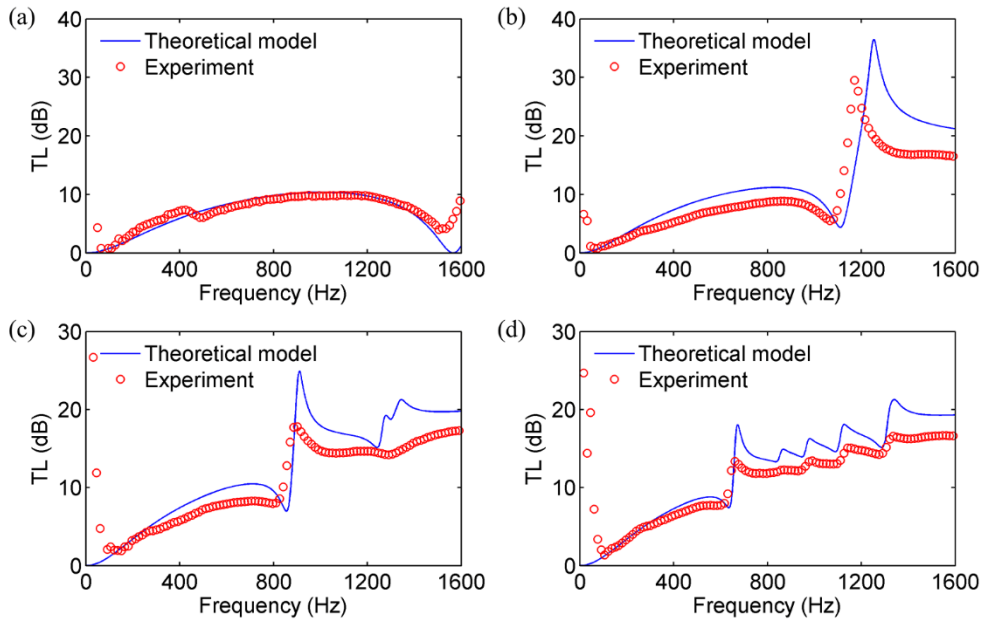


Fig. 4.20 The results of the experiments for the samples in Fig. 4.19 for frequency range upto 1600 Hz. The results by the theoretical model are also presented for comparison. (a) Sample 0, (b) Sample 1, (c) Sample 2, and (d) Sample 3.

(100 mm). And due to the manufacturing error, some samples were fabricated even smaller. Nevertheless, the results in Fig. 4.20 show that the sound insulation performance of the acoustic double layer with holes can be enhanced by the proposed metamaterials.

4.5 Concluding remarks

This chapter proposed the acoustic metamaterials for sound transmission control. More specifically, the metamaterials were designed to enhance the sound insulation performance of the acoustic double layers with holes. It was shown that the proposed metamaterials could improve the low frequency sound insulation performance compared with the conventional acoustic double layer with holes, or acoustic double fishnet, by properly inserting the rigid partitions inside the gap between the double layers.

The rigid partitions in the gap are inserted to form several resonators with various resonance frequencies, unlike the conventional acoustic resonators, such as Helmholtz resonators, that have resonance mode at single frequency. The designed resonators have waveguide parts and side resonator parts of different resonance frequencies. Then the wave velocity traveling along the waveguide in the resonator are changed due to the interaction with the side resonators. Therefore, the resonance frequencies of the resonator can be changed following the relation between the dimension of the resonator and the changed velocity.

The theoretical analysis showed that the sound transmission of the metamaterials can be successfully modelled by adopting transfer matrix method. The impedances of the designed resonators also can be modelled by using effective medium concept,

and multi-layering of the effective layers. In the theoretical analysis, the viscous and thermal losses occurred due to the small dimension between the rigid partitions are involved in the model. By comparing with the results obtained by numerical methods based on the finite element method, the validity of the theoretical model was confirmed. In addition, the transmission experiments showed that the designed metamaterials show enhanced sound insulation performances compared with the nominal case of the acoustic double layer with holes.

CHAPTER 5.

CONCLUSIONS

The conventional acoustic systems used for sound attenuation suffer from a limitation in achieving broadband performance. Even though various acoustic metamaterials, well-known for their extraordinary performances, have investigated so far, but their acoustic performances are still limited in a narrow band of frequency. This is due to the lack of design method to incorporate physical mechanisms effective for a broad range of frequency, especially covering the low frequency region. Under the circumstance, this thesis presented that the broadband sound attenuation performance can be greatly enhanced by using proposed acoustic metamaterials designed with rigid partitions. The rigid partitions inserted in the acoustic metamaterials can act as waveguides or resonators so that wave propagation characteristics in the metamaterials can be tailored at will. The results showed that the acoustic metamaterials provided a breakthrough not only to overcome the limitation of the conventional acoustic materials but also to compensate the limited performance of the previously-proposed acoustic metamaterials.

The key physical phenomenon for the achievement is the multiple resonance modes generated in a single system. It could be realized by properly allocating the rigid partitions in porous layers or in acoustic double layer for the purpose of sound absorption and insulation, respectively. The physics of the metamaterials were investigated using the theoretical models derived based on the effective medium approach. Once the effective medium properties of the metamaterial were obtained, the reflection and transmission of the acoustic waves were evaluated by using an impedance concept and a transfer matrix modeling.

For the sound absorption problem, the metaporous layers with tuned thickness resonances and multiple slow waves are presented. A study on the absorption mechanism of a porous layer revealed that the resonances related to the thickness of the porous layer have a strong influence on the sound absorption performance. The two types of metaporous layers presented in the thesis effectively controlled the corresponding resonance frequencies by tailoring effective thicknesses and by slowing effective wave velocities. In the metaporous layer with tuned thickness resonances, the periodic perpendicular, horizontal rigid partitions are inserted to control the effective thickness of the porous layer. The effective thickness was able to be increased from the original thickness of a given porous layer by inserting the gap at the end of the perpendicular partition and decreased by the horizontal partition. In the metaporous layer with multiple slow waves, the horizontal rigid partitions of various lengths are used to form side resonators along the wave propagation direction.

The resonators of various resonance frequencies change the dispersion characteristic of the waves, which results in multiple slow wave propagation. As a result, the metaporous layers exhibited significantly enhanced sound absorption performance in a broad range of frequency compared with the homogeneous layer with a same thickness.

For the sound transmission problem, the acoustic double layer with holes was considered. The hole in the layer allows airflow through the acoustic medium so that it can be useful when ventilation or heat exhaustion are necessary. For the considered configuration, the cross-sectional dimension in the gap between the two layers determines the frequency of the transmission loss peak. The transmission peak is located in high frequency range due to the restricted dimension in the plane. To enhance the performance in the low frequency range, the rigid partitions are inserted in the gap to form multiple resonators. Then the structure made of the rigid partitions compose a planar resonator with various resonance frequencies. Similar to the results in the metaporous layer with multiple slow waves, the multiple slow waves can be generated in the proposed meta-resonator. The analysis showed that the sound insulation performance can be enhanced in the broad frequency range by using the proposed metamaterial. The validity of the designed metamaterials is also confirmed by experimental results.

It is expected that the acoustic metamaterials presented in this thesis can be used in various industries for sound absorption and insulation purpose. The metaporous layers can be installed on walls or ceilings in a room for sound absorption and they can be also used as duct liners. The metamaterials designed for sound insulation can be used as noise barrier in various circumstances especially for the cases ventilation or heat exhaust are needed, such as radiator panels for vehicle engine, refrigerators, etc. Because the proposed metamaterials can overcome the geometric limitation of the space for the installation, they have the advantage to guarantee outstanding performance while occupying less space. To use the metamaterials for a target frequency or frequency band, the geometric parameters of the designed metamaterials can be changed as long as the periodicity remains in a subwavelength scale. Once the target frequency ranges are determined, the desired structures can be obtained by simple parametric studies or by using optimization methods. In addition, the metamaterials can be used in airplanes or vehicles that need substantial stiffness as well as the noise reduction capability.

APPENDIX A.

EFFECTIVE MEDIUM MODELS

FOR AXISYMMETRIC

METAPOROUS LAYERS

Section 3.4 mainly dealt with the metaporous layers with multiple slow waves in two dimensional configurations. However, as revealed in section 3.4.4, the three-dimensional metaporous layers can be obtained by using the same physical phenomena. In this appendix, the derivation of the effective medium model of the axisymmetric configurations shown in Fig. 3.23 will be presented.

In Fig. 3.23, it was shown that two types of axisymmetric configuration of the metaporous layer designed to have multiple slow waves are possible. The first one is shown in Fig. 3.23(a), the rigid partitions of the shapes of circular plates are inserted aligned to the center of the cylindrical coordinates. The second one is shown in Fig. 3.23(b), the rigid partitions are aligned to the outer side of the circle and have

the shapes of disk. For convenience, the configuration in Fig. 3.23(a) will be referred as ‘Axisymmetric 1’ and the other one in Fig. 3.23(b), ‘Axisymmetric 2’ in the followings.

Axisymmetric 1

Figure A.1 shows a configuration of an axisymmetric metaporous layer whose rigid partitions of circular plates have the same radius a . As same as in the metaporous layer in two-dimensional configuration, dispersion relation of the metaporous layer can be obtained by considering the waves in the region (1) and region (2) denoted in the figure. The pressure waves in the region (1) and (2) can be expressed as

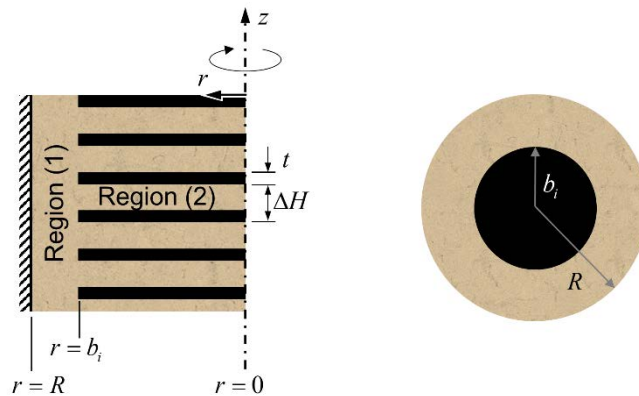


Fig. A.1 Axisymmetric configurations of the metaporous layer of radius R when the rigid partition of circular shapes are aligned at the center of the layer. The radius of the rigid partitions are set to be equal to b_i .

$$p_1 = AJ_0(k_1 r), \quad (\text{A.1})$$

$$p_2 = \{BJ_0(k_r r) + CY_0(k_r r)\} e^{jk_z z}. \quad (\text{A.2})$$

respectively, where J_n and Y_n ($n = 0, 1, 2, 3, \dots$) are the Bessel functions of the first and second kind. The wavenumber in the r and z direction, k_r and k_z respectively, satisfied that $k_1^2 = k_r^2 + k_z^2$. Accordingly, the particle velocities in the r direction are obtained as

$$v_{1r} = \frac{-k_1}{j\omega\rho_1} AJ_1(k_1 r), \quad (\text{A.3})$$

$$v_{2r} = \frac{-k_r}{j\omega\rho_1} \{BJ_1(k_r r) - CY_1(k_r r)\} e^{jk_z z}. \quad (\text{A.4})$$

By considering a boundary condition at $v_{2r}(r=R)=0$, Eq. (A.2) can be rewritten as

$$p_2 = B[Y_1(k_r R)J_0(k_r r) - J_1(k_r R)Y_0(k_r r)] e^{jk_z z}. \quad (\text{A.5})$$

Then, the continuity of the pressure and the volume velocity at $r=b_i$ gives the dispersion relation

$$\eta k_1 \frac{J_1(k_1 b_i)}{J_0(k_1 b_i)} = k_r \frac{Y_1(k_r R)J_1(k_r b_i) - J_1(k_r R)Y_1(k_r b_i)}{Y_1(k_r R)J_0(k_r b_i) - J_1(k_r R)Y_0(k_r b_i)}, \quad (\text{A.6})$$

where η is the volume ratio of the porous medium in the z direction, $1-t/\Delta H$.

The Bessel function of the first and the second kind can be expressed roughly as [97]

$$J_n(x) \sim \sqrt{\frac{2}{\pi x}} \cos\left(x - \left(\frac{n}{2} + \frac{1}{4}\right)\pi\right), \quad (\text{A.7})$$

$$Y_n(x) \sim \sqrt{\frac{2}{\pi x}} \sin\left(x - \left(\frac{n}{2} + \frac{1}{4}\right)\pi\right), \quad (\text{A.8})$$

therefore, the substitution of Eqs. (A.7) and (A.8) into Eq. (A.6) yields

$$\eta k_1 \frac{J_1(k_1 b_i)}{J_0(k_1 b_i)} = -k_r \sin(k_r (R - b_i)). \quad (\text{A.9})$$

By using that $\sin x \approx x$ when $x \ll 1$ (low frequency assumption), Eq. (A.9) becomes

$$\eta k_1 \frac{J_1(k_1 b_i)}{J_0(k_1 b_i)} = -k_r^2 (R - b_i). \quad (\text{A.10})$$

Rearrangement of Eq. (A.10) in terms of the k_r gives

$$k_r^2 = -\frac{\eta k_1 J_1(k_1 b_i)}{R - b_i J_0(k_1 b_i)}. \quad (\text{A.11})$$

Because the z -directional wavenumber k_z becomes the effective wavenumber when the medium is regarded as an one-dimensional effective medium, the effective wavenumber k_e is obtained as

$$k_e = k_z = \sqrt{k_1^2 - k_r^2} = k_1 \sqrt{1 + \frac{\eta}{k_1(R-b_i)} \frac{J_1(k_1 b_i)}{J_0(k_1 b_i)}}. \quad (\text{A.12})$$

The effective wave velocity is also obtained as

$$c_e = \frac{\omega}{k_e} = c_1 / \sqrt{1 + \frac{\eta}{k_1(R-b_i)} \frac{J_1(k_1 b_i)}{J_0(k_1 b_i)}}. \quad (\text{A.12})$$

By considering the amount of the reflected energy fraction due to the rigid circular partition, the effective density is obtained as

$$\rho_e = \frac{\rho_1}{(1-\phi_i)}, \quad (\text{A.13})$$

where ϕ_i is b_i^2/R^2 , then the effective bulk modulus is given by

$$\kappa_e = \rho_e c_e^2 = \frac{\kappa_1}{(1-\phi_i) \left[1 + \frac{\eta}{k_1(R-b_i)} \frac{J_1(k_1 b_i)}{J_0(k_1 b_i)} \right]}. \quad (\text{A.14})$$

Axisymmetric 2

The effective medium model of the configuration shown in Fig. A.2 also can be obtained by the procedures presented above. The pressure fields in the region (1) and (2) denoted in Fig. A.2 are

$$p_1 = A[Y_1(k_1 R)J_0(k_1 r) - J_1(k_1 R)Y_0(k_1 r)], \quad (\text{A.15})$$

$$p_2 = B J_0(k_r r) e^{jk_z z}, \quad (\text{A.16})$$

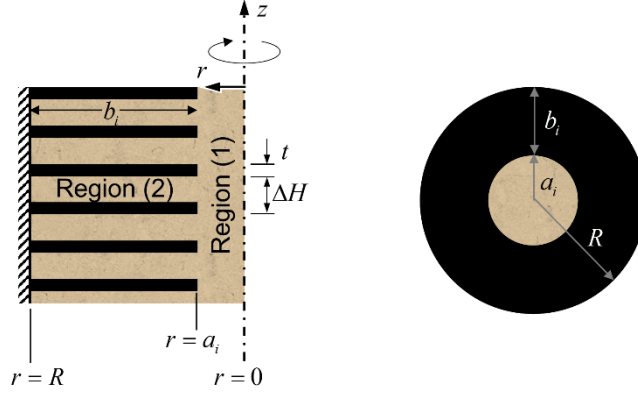


Fig.A.2 (b) Axisymmetric configurations of the metaporous layer of radius R when the rigid partitions of disk shapes are aligned at the outer boundary of the layer. The inner radius of the rigid partitions are set to be equal to a_i .

respectively, and particle velocities along the r direction are given by

$$v_{1r} = \frac{-k_1}{j\omega\rho_1} A [Y_1(k_1 R) J_1(k_1 r) - J_1(k_1 R) Y_1(k_1 r)], \quad (\text{A.17})$$

$$v_{2r} = \frac{-k_r}{j\omega\rho_1} B J_1(k_r r) e^{jk_z z}. \quad (\text{A.18})$$

The continuity of the pressure and the volume velocity at $r = a_i$ gives the dispersion relation

$$\eta k_1 \frac{Y_1(k_1 R) J_1(k_1 a_i) - J_1(k_1 R) Y_1(k_1 a_i)}{Y_1(k_1 R) J_0(k_1 a_i) - J_1(k_1 R) Y_0(k_1 a_i)} = k_r \frac{J_1(k_r a_i)}{J_0(k_r a_i)} \quad (\text{A.19})$$

By using that $J_0(x) \sim 1$ and $J_1(x) \sim x/2$ for $x \ll 1$, the right-hand side of Eq.(A.19) becomes $k_r^2 a_i / 2$. By rearranging Eq. (A.19) in terms of k_r gives

$$k_r^2 = \frac{2\eta k_1}{a_i} \frac{Y_1(k_1 R) J_1(k_1 a_i) - J_1(k_1 R) Y_1(k_1 a_i)}{Y_1(k_1 R) J_0(k_1 a_i) - J_1(k_1 R) Y_0(k_1 a_i)}. \quad (\text{A.20})$$

The effective wavenumber of the effective medium can be obtained by

$$k_e = k_z = \sqrt{k_1^2 - k_r^2} = k_1 \sqrt{1 - \frac{2\eta}{k_1 a_i} \frac{Y_1(k_1 R) J_1(k_1 a_i) - J_1(k_1 R) Y_1(k_1 a_i)}{Y_1(k_1 R) J_0(k_1 a_i) - J_1(k_1 R) Y_0(k_1 a_i)}}. \quad (\text{A.21})$$

The effective wave velocity becomes

$$c_e = \frac{\omega}{k_e} = c_1 / \sqrt{1 - \frac{2\eta}{k_1 a_i} \frac{Y_1(k_1 R) J_1(k_1 a_i) - J_1(k_1 R) Y_1(k_1 a_i)}{Y_1(k_1 R) J_0(k_1 a_i) - J_1(k_1 R) Y_0(k_1 a_i)}}. \quad (\text{A.21})$$

Likewise, the effective density is obtained by

$$\rho_e = \frac{\rho_1}{(1 - \phi_i)}, \quad (\text{A.22})$$

where ϕ_i is $1 - a_i^2 / R^2$, then the effective bulk modulus is given by

$$\kappa_e = \rho_e c_e^2 = \frac{\kappa_1}{(1 - \phi_i) \left[1 - \frac{2\eta}{k_1 a_i} \frac{Y_1(k_1 R) J_1(k_1 a_i) - J_1(k_1 R) Y_1(k_1 a_i)}{Y_1(k_1 R) J_0(k_1 a_i) - J_1(k_1 R) Y_0(k_1 a_i)} \right]}. \quad (\text{A.23})$$

REFERENCES

- [1] Z. Liu, X. Zhang, Y. Mao, Y. Y. Zhu, Y. Zhiyu, C. T. Chan, and P. Sheng, “Locally Resonant Sonic Materials,” *Science*, vol. 289, no. 5485, pp. 1734–1736, Sep. 2000.
- [2] Z. Yang, J. Mei, M. Yang, N. H. Chan, and P. Sheng, “Membrane-Type Acoustic Metamaterial with Negative Dynamic Mass,” *Phys. Rev. Lett.*, vol. 101, no. 20, p. 204301, 2008.
- [3] M. Yang, G. Ma, Z. Yang, and P. Sheng, “Coupled Membranes with Doubly Negative Mass Density and Bulk Modulus,” *Phys. Rev. Lett.*, vol. 110, no. 13, p. 134301, 2013.
- [4] F. Ma, J. H. Wu, M. Huang, W. Zhang, and S. Zhang, “A purely flexible lightweight membrane-type acoustic metamaterial,” *J. Phys. D: Appl. Phys.*, vol. 48, no. 17, p. 175105, 2015.
- [5] C. J. Naify, C. M. Chang, G. McKnight, F. Scheulen, and S. Nutt, “Membrane-type metamaterials: Transmission loss of multi-celled arrays,” *J. Appl. Phys.*, vol. 109, no. 10, pp. 3–11, 2011.
- [6] J. Mei, G. Ma, M. Yang, Z. Yang, W. Wen, and P. Sheng, “Dark acoustic metamaterials as super absorbers for low-frequency sound,” *Nat. Commun.*, vol. 3, p. 756, Mar. 2012.
- [7] G. Ma, M. Yang, S. Xiao, Z. Yang, and P. Sheng, “Acoustic metasurface with hybrid resonances,” *Nat. Mater.*, vol. 13, no. 9, pp. 873–878, 2014.

- [8] S. Varanasi, J. S. Bolton, T. H. Siegmund, and R. J. Cipra, “The low frequency performance of metamaterial barriers based on cellular structures,” *Appl. Acoust.*, vol. 74, no. 4, pp. 485–495, 2013.
- [9] N. Sui, X. Yan, T.-Y. Huang, J. Xu, F.-G. Yuan, and Y. Jing, “A lightweight yet sound-proof honeycomb acoustic metamaterial,” *Appl. Phys. Lett.*, vol. 106, no. 17, p. 171905, 2015.
- [10] X. Cai, Q. Guo, G. Hu, and J. Yang, “Ultrathin low-frequency sound absorbing panels based on coplanar spiral tubes or coplanar Helmholtz resonators,” *Appl. Phys. Lett.*, vol. 105, no. 12, p. 121901, 2014.
- [11] Y. Li and B. M. Assouar, “Acoustic metasurface-based perfect absorber with deep subwavelength thickness,” *Appl. Phys. Lett.*, vol. 108, no. 6, p. 063502, Feb. 2016.
- [12] J.-P. Groby, W. Huang, A. Lardeau, and Y. Aurégan, “The use of slow waves to design simple sound absorbing materials,” *J. Appl. Phys.*, vol. 117, no. 12, p. 124903, Mar. 2015.
- [13] J. Christensen, V. Romero-García, R. Picó, A. Cebrecos, F. J. G. de Abajo, N. A. Mortensen, M. Willatzen, and V. J. Sánchez-Morcillo, “Extraordinary absorption of sound in porous lamella-crystals,” *Sci. Rep.*, vol. 4, p. 4674, Apr. 2014.
- [14] X. Jiang, B. Liang, R. Li, X. Zou, L. Yin, and J. Cheng, “Ultra-broadband absorption by acoustic metamaterials,” *Appl. Phys. Lett.*, vol. 105, no. 24, p. 243505, Dec. 2014.

- [15] V. Romero-García, G. Theocharis, O. Richoux, A. Merkel, V. Tournat, and V. Pagneux, “Perfect and broadband acoustic absorption by critically coupled sub-wavelength resonators,” *Sci. Rep.*, vol. 6, p. 19519, Jan. 2016.
- [16] J. B. Pendry, A. J. Holden, W. J. Stewart, and I. Youngs, “Extremely Low Frequency Plasmons in Metallic Mesostructures,” *Phys. Rev. Lett.*, vol. 76, no. 25, pp. 4773–4776, Jun. 1996.
- [17] J. B. Pendry, A. J. Holden, D. J. Robbins, and W. J. Stewart, “Low frequency plasmons in thin-wire structures,” *J. Phys. Condens. Matter*, vol. 10, no. 22, pp. 4785–4809, Jun. 1998.
- [18] D. R. Smith, W. J. Padilla, D. C. Vier, S. C. Nemat-Nasser, and S. Schultz, “Composite Medium with Simultaneously Negative Permeability and Permittivity,” *Phys. Rev. Lett.*, vol. 84, no. 18, pp. 4184–4187, May 2000.
- [19] N. I. Landy, S. Sajuyigbe, J. J. Mock, D. R. Smith, and W. J. Padilla, “Perfect Metamaterial Absorber,” *Phys. Rev. Lett.*, vol. 100, no. 20, p. 207402, 2008.
- [20] Y. Cui, K. H. Fung, J. Xu, H. Ma, Y. Jin, S. He, and N. X. Fang, “Ultrabroadband light absorption by a sawtooth anisotropic metamaterial slab,” *Nano Lett.*, vol. 12, no. 3, pp. 1443–1447, 2012.
- [21] D. Ye, Z. Wang, K. Xu, H. Li, J. Huangfu, Z. Wang, and L. Ran, “Ultrawideband Dispersion Control of a Metamaterial Surface for Perfectly-Matched-Layer-Like Absorption,” *Phys. Rev. Lett.*, vol. 111, no. 18, p. 187402, Oct. 2013.
- [22] D. Ji, H. Song, X. Zeng, H. Hu, K. Liu, N. Zhang, and Q. Gan, “Broadband

- absorption engineering of hyperbolic metafilm patterns,” *Sci. Rep.*, vol. 4, p. 4498, 2014.
- [23] T. W. Ebbesen, H. J. Lezec, H. F. Ghaemi, T. Thio, and P. A. Wolff, “Extraordinary optical transmission through sub-wavelength hole arrays,” *Nature*, vol. 391, pp. 667–669, Feb. 1998.
- [24] L. Martín-Moreno, F. J. García-Vidal, H. J. Lezec, K. M. Pellerin, T. Thio, J. B. Pendry, and T. W. Ebbesen, “Theory of Extraordinary Optical Transmission through Subwavelength Hole Arrays,” *Phys. Rev. Lett.*, vol. 86, no. 6, pp. 1114–1117, 2001.
- [25] H. Liu and P. Lalanne, “Microscopic theory of the extraordinary optical transmission,” *Nature*, vol. 452, pp. 728–731, Apr. 2008.
- [26] A. B. Khanikaev, S. H. Mousavi, G. Shvets, and Y. S. Kivshar, “One-way extraordinary optical transmission and nonreciprocal spoof plasmons,” *Phys. Rev. Lett.*, vol. 105, no. 12, p. 126804, 2010.
- [27] J. B. Pendry, “Negative Refraction Makes a Perfect Lens,” *Phys. Rev. Lett.*, vol. 85, no. 18, pp. 3966–3969, Oct. 2000.
- [28] Z. Liu, H. Lee, Y. Xiong, C. Sun, and X. Zhang, “Far-Field Optical Hyperlens Magnifying Sub-Diffraction-Limited Objects,” *Science (80-.)*, vol. 315, no. 5819, pp. 1686–1686, Mar. 2007.
- [29] N. Fang, D. Xi, J. Xu, M. Ambati, W. Srituravanich, C. Sun, and X. Zhang, “Ultrasonic metamaterials with negative modulus,” *Nat. Mater.*, vol. 5, no. 6, pp. 452–456, Jun. 2006.

- [30] V. M. García-Chocano, R. Graciá-Salgado, D. Torrent, F. Cervera, and J. Sánchez-Dehesa, “Quasi-two-dimensional acoustic metamaterial with negative bulk modulus,” *Phys. Rev. B*, vol. 85, no. 18, p. 184102, May 2012.
- [31] Y. Cheng, C. Zhou, B. G. Yuan, D. J. Wu, Q. Wei, and X. J. Liu, “Ultra-sparse metasurface for high reflection of low-frequency sound based on artificial Mie resonances,” *Nat. Mater.*, vol. 14, no. 10, pp. 1013–1019, 2015.
- [32] C. Lagarrigue, J. P. Groby, V. Tournat, O. Dazel, and O. Umnova, “Absorption of sound by porous layers with embedded periodic arrays of resonant inclusions,” *J. Acoust. Soc. Am.*, vol. 134, no. 6, pp. 4670–4680, 2013.
- [33] J.-P. Groby, B. Brouard, O. Dazel, B. Nennig, and L. Kelders, “Enhancing rigid frame porous layer absorption with three-dimensional periodic irregularities,” *J. Acoust. Soc. Am.*, vol. 133, no. 2, pp. 821–831, 2013.
- [34] M. R. Stinson, “The propagation of plane sound waves in narrow and wide circular tubes, and generalization to uniform tubes of arbitrary cross-sectional shape,” *J. Acoust. Soc. Am.*, vol. 89, no. 2, pp. 550–558, 1991.
- [35] J. F. Allard and N. Atalla, *Propagation of Sound in Porous Media: Modelling Sound Absorbing Materials*, 2nd ed. John Wiley & Sons, 2009.
- [36] J. Dubois, C. Aristégui, and O. Poncelet, “Spaces of electromagnetic and mechanical constitutive parameters for dissipative media with either positive or negative index,” *J. Appl. Phys.*, vol. 115, no. 2, p. 024902, 2014.
- [37] M. A. Biot, “Theory of Propagation of Elastic Waves in a Fluid-Saturated

- Porous Solid. I. Low-Frequency Range,” *J. Acoust. Soc. Am.*, vol. 28, no. 2, pp. 168–178, 1956.
- [38] M. E. Delany and E. N. Bazley, “Acoustical properties of fibrous absorbent materials,” *Appl. Acoust.*, vol. 3, no. 2, pp. 105–116, Apr. 1970.
- [39] Y. Miki, “Acoustical properties of porous materials. Modifications of Delany-Bazley models,” *J. Acoust. Soc. Japan*, vol. 11, no. 1, pp. 19–24, 1990.
- [40] W. Qunli, “Empirical relations between acoustical properties and flow resistivity of porous plastic open-cell foam,” *Appl. Acoust.*, vol. 25, no. 3, pp. 141–148, 1988.
- [41] F. P. Mechel, “Design charts for sound absorber layers,” *J. Acoust. Soc. Am.*, vol. 83, no. 3, pp. 1002–1013, 1988.
- [42] T. Komatsu, “Improvement of the Delany-Bazley and Miki models for fibrous sound-absorbing materials,” *Acoust. Sci. Technol.*, vol. 29, no. 2, pp. 121–129, 2008.
- [43] D. K. Wilson, “Relaxation-matched modeling of propagation through porous media, including fractal pore structure,” *J. Acoust. Soc. Am.*, vol. 94, no. 2, pp. 1136–1145, 1993.
- [44] D. L. Johnson, J. Koplik, and R. Dashen, “Theory of dynamic permeability and tortuosity in fluid-saturated porous media,” *J. Fluid Mech.*, vol. 176, pp. 379–402, 1987.
- [45] Y. Champoux and J.-F. Allard, “Dynamic tortuosity and bulk modulus in air-

- saturated porous media,” *J. Appl. Phys.*, vol. 70, no. 4, p. 1975, 1991.
- [46] D. Lafarge, “Dynamic compressibility of air in porous structures at audible frequencies,” *J. Acoust. Soc. Am.*, vol. 102, no. 4, pp. 1995–2006, Oct. 1997.
- [47] Y. Champoux, “Air-based system for the measurement of porosity,” *J. Acoust. Soc. Am.*, vol. 89, no. 2, pp. 910–916, 1991.
- [48] L. L. Beranek, “Acoustic Impedance of Porous Materials,” *J. Acoust. Soc. Am.*, vol. 13, no. 3, pp. 248–260, 1942.
- [49] D. A. Bies and C. H. Hansen, “Flow resistance information for acoustical design,” *Appl. Acoust.*, vol. 13, no. 5, pp. 357–391, Sep. 1980.
- [50] M. R. Stinson, “Electronic system for the measurement of flow resistance,” *J. Acoust. Soc. Am.*, vol. 83, no. 6, pp. 2422–2428, 1988.
- [51] D. L. Johnson, J. Koplik, and L. M. Schwartz, “New Pore-Size Parameter Characterizing Transport in Porous Media,” *Phys. Rev. Lett.*, vol. 57, no. 20, pp. 2564–2567, Nov. 1986.
- [52] J.-P. Groby, C. Lagarrigue, B. Brouard, O. Dazel, V. Tournat, and B. Nennig, “Enhancing the absorption properties of acoustic porous plates by periodically embedding Helmholtz resonators,” *J. Acoust. Soc. Am.*, vol. 137, no. 1, pp. 273–280, Jan. 2015.
- [53] J.-P. Groby, A. Duclos, O. Dazel, L. Boeckx, and W. Lauriks, “Absorption of a rigid frame porous layer with periodic circular inclusions backed by a periodic grating,” *J. Acoust. Soc. Am.*, vol. 129, no. 5, pp. 3035–3046, 2011.
- [54] J.-P. Groby, W. Lauriks, and T. E. Vigran, “Total absorption peak by use of

- a rigid frame porous layer backed by a rigid multi-irregularities grating,” *J. Acoust. Soc. Am.*, vol. 127, no. 5, pp. 2865–2874, May 2010.
- [55] T. J. Cox and P. D’Antonio, *Acoustic absorbers and diffusers: theory, design and application*, 2nd ed. CRC Press, 2009.
- [56] M. L. Munjal, *Acoustics of Ducts and Mufflers*, 2nd ed. Chichester, UK: John Wiley & Sons, 2014.
- [57] F. P. Mechel, *Formulas of Acoustics*. Berlin, Heidelberg: Springer Berlin Heidelberg, 2004.
- [58] O. Tanneau, J. B. Casimir, and P. Lamary, “Optimization of multilayered panels with poroelastic components for an acoustical transmission objective,” *J. Acoust. Soc. Am.*, vol. 120, no. 3, pp. 1227–1238, 2006.
- [59] J. S. Lee, E. I. Kim, Y. Y. Kim, J. S. Kim, and Y. J. Kang, “Optimal poroelastic layer sequencing for sound transmission loss maximization by topology optimization method,” *J. Acoust. Soc. Am.*, vol. 122, no. 4, pp. 2097–2106, Oct. 2007.
- [60] J. S. Lee, Y. Y. Kim, J. S. Kim, and Y. J. Kang, “Two-dimensional poroelastic acoustical foam shape design for absorption coefficient maximization by topology optimization method,” *J. Acoust. Soc. Am.*, vol. 123, no. 4, pp. 2094–2106, Apr. 2008.
- [61] J.-P. Groby, A. Wirgin, L. De Ryck, W. Lauriks, R. P. Gilbert, and Y. S. Xu, “Acoustic response of a rigid-frame porous medium plate with a periodic set of inclusions,” *J. Acoust. Soc. Am.*, vol. 126, no. 2, pp. 685–693, Aug. 2009.

- [62] J.-P. Groby, O. Dazel, A. Duclos, L. Boeckx, and L. Kelders, “Enhancing the absorption coefficient of a backed rigid frame porous layer by embedding circular periodic inclusions,” *J. Acoust. Soc. Am.*, vol. 130, no. 6, pp. 3771–3780, Dec. 2011.
- [63] J. Christensen, N. A. Mortensen, and M. Willatzen, “Modelling the acoustical response of lossy lamella-crystals,” *J. Appl. Phys.*, vol. 116, no. 16, p. 163508, Oct. 2014.
- [64] V. Romero-García, J. V. Sánchez-Pérez, and L. M. Garcia-Raffi, “Tunable wideband bandstop acoustic filter based on two-dimensional multiphysical phenomena periodic systems,” *J. Appl. Phys.*, vol. 110, no. 1, p. 014904, 2011.
- [65] A. S. Elliott, R. Venegas, J. P. Groby, and O. Umnova, “Omnidirectional acoustic absorber with a porous core and a metamaterial matching layer,” *J. Appl. Phys.*, vol. 115, no. 20, p. 204902, May 2014.
- [66] L. E. Kinsler, A. R. Frey, A. B. Coppers, and J. V Sanders, *Fundamentals of acoustics*, 4th ed. Wiley-VCH, 1999.
- [67] H. Kuttruff, *Room acoustics*, 5th ed. CRC Press, 2009.
- [68] J. Li, L. Fok, X. Yin, G. Bartal, and X. Zhang, “Experimental demonstration of an acoustic magnifying hyperlens,” *Nat. Mater.*, vol. 8, no. 12, pp. 931–934, Dec. 2009.
- [69] “COMSOL Multiphysics 4.3.” COMSOL Inc., Stockholm, Sweden, 2012.
- [70] Z. Liang and J. Li, “Extreme Acoustic Metamaterial by Coiling Up Space,” *Phys. Rev. Lett.*, vol. 108, no. 11, p. 114301, 2012.

- [71] Y. Li, B. Liang, X. Tao, X. Zhu, X. Zou, and J. Cheng, “Acoustic focusing by coiling up space,” *Appl. Phys. Lett.*, vol. 101, no. 23, p. 233508, 2012.
- [72] Y. Li, B. Liang, X. Zou, and J. Cheng, “Extraordinary acoustic transmission through ultrathin acoustic metamaterials by coiling up space,” *Appl. Phys. Lett.*, vol. 103, no. 6, p. 063509, 2013.
- [73] Y. Xie, B.-I. Popa, L. Zigoneanu, and S. A. Cummer, “Measurement of a Broadband Negative Index with Space-Coiling Acoustic Metamaterials,” *Phys. Rev. Lett.*, vol. 110, no. 17, p. 175501, Apr. 2013.
- [74] J. Zhu, Y. Chen, X. Zhu, F. J. Garcia-Vidal, X. Yin, W. Zhang, and X. Zhang, “Acoustic rainbow trapping,” *Sci. Rep.*, vol. 3, p. 1728, Apr. 2013.
- [75] G. Theocharis, O. Richoux, V. R. García, A. Merkel, and V. Tournat, “Limits of slow sound propagation and transparency in lossy, locally resonant periodic structures,” *New J. Phys.*, vol. 16, no. 9, p. 093017, Sep. 2014.
- [76] J. Yang, J. S. Lee, and Y. Y. Kim, “Metaporous layer to overcome the thickness constraint for broadband sound absorption,” *J. Appl. Phys.*, vol. 117, no. 17, p. 174903, May 2015.
- [77] L. Fan, Z. Chen, S. Y. Zhang, J. Ding, X. J. Li, and H. Zhang, “An acoustic metamaterial composed of multi-layer membrane-coated perforated plates for low-frequency sound insulation,” *Appl. Phys. Lett.*, vol. 106, no. 15, p. 151908, 2015.
- [78] M. H. Lu, X. K. Liu, L. Feng, J. Li, C. P. Huang, Y. F. Chen, Y. Y. Zhu, S. N. Zhu, and N. Ben Ming, “Extraordinary acoustic transmission through a

- 1D grating with very narrow apertures,” *Phys. Rev. Lett.*, vol. 99, no. 17, p. 174301, 2007.
- [79] J. Christensen, L. Martín-Moreno, and F. J. García-Vidal, “Theory of Resonant Acoustic Transmission through Subwavelength Apertures,” *Phys. Rev. Lett.*, vol. 101, no. 1, p. 014301, 2008.
- [80] X. Wang, “Theory of resonant sound transmission through small apertures on periodically perforated slabs,” *J. Appl. Phys.*, vol. 108, no. 6, p. 064903, 2010.
- [81] H. Estrada, P. Candelas, A. Uris, F. Belmar, F. Meseguer, and F. J. García de Abajo, “Influence of the hole filling fraction on the ultrasonic transmission through plates with subwavelength aperture arrays,” *Appl. Phys. Lett.*, vol. 93, no. 1, p. 011907, 2008.
- [82] J. Christensen, L. Martín-Moreno, and F. J. García-Vidal, “All-angle blockage of sound by an acoustic double-fishnet metamaterial,” *Appl. Phys. Lett.*, vol. 97, no. 13, p. 134106, 2010.
- [83] Z. Liu and G. Jin, “Acoustic transmission resonance and suppression through double-layer subwavelength hole arrays,” *J. Phys. Condens. Matter*, vol. 22, no. 30, p. 305003, 2010.
- [84] J. S. Bell, I. R. Summers, A. R. J. Murray, E. Hendry, J. R. Sambles, and A. P. Hibbins, “Low acoustic transmittance through a holey structure,” *Phys. Rev. B*, vol. 85, no. 21, p. 214305, 2012.
- [85] A. R. J. Murray, E. Hendry, I. R. Summers, J. R. Sambles, and A. P. Hibbins,

- “Control of the stop band of an acoustic double fishnet,” *J. Acoust. Soc. Am.*, vol. 134, no. 3, pp. 1754–1759, 2013.
- [86] C. Rubio, A. Uris, P. Candelas, F. Belmar, and V. Gomez-Lozano, “A tunable acoustic barrier based on periodic arrays of subwavelength slits,” *AIP Adv.*, vol. 5, no. 5, p. 057150, May 2015.
- [87] A. R. J. Murray, I. R. Summers, J. R. Sambles, and A. P. Hibbins, “An acoustic double fishnet using Helmholtz resonators,” *J. Acoust. Soc. Am.*, vol. 136, no. 3, pp. 980–984, 2014.
- [88] C. Rubio, P. Candelas, F. Belmar, V. Gomez-Lozano, and A. Uris, “Subwavelength slit acoustic metamaterial barrier,” *J. Phys. D: Appl. Phys.*, vol. 48, no. 39, p. 395501, 2015.
- [89] F. Fahy, *Foundations of Engineering Acoustics*. San Diego: Academic Press, 2000.
- [90] W. K. R. Lippert, “Sound propagation in ducts with side branches,” *Acoustica*, vol. 7, no. 3, pp. 137–145, 1957.
- [91] S. K. Tang, “Sound transmission characteristics of Tee-junctions and the associated length corrections,” *J. Acoust. Soc. Am.*, vol. 115, no. 1, pp. 218–227, 2004.
- [92] S.-H. Seo and Y.-H. Kim, “Silencer design by using array resonators for low-frequency band noise reduction,” *J. Acoust. Soc. Am.*, vol. 118, no. 4, pp. 2332–2338, 2005.
- [93] S. K. Tang, “Narrow sidebranch arrays for low frequency duct noise control,”

- J. Acoust. Soc. Am.*, vol. 132, no. 5, pp. 3086–3097, 2012.
- [94] U. Ingard, “On the Theory and Design of Acoustic Resonators,” *J. Acoust. Soc. Am.*, vol. 25, no. 6, pp. 1037–1061, 1953.
- [95] Y. Cheng, J. Y. Xu, and X. J. Liu, “Broad forbidden bands in parallel-coupled locally resonant ultrasonic metamaterials,” *Appl. Phys. Lett.*, vol. 92, no. 5, p. 051913, 2008.
- [96] A. Isozaki, H. Takahashi, H. Tamura, T. Takahata, K. Matsumoto, A. Isozaki, H. Takahashi, H. Tamura, and T. Takahata, “Parallel Helmholtz resonators for a planar acoustic notch filter,” *Appl. Phys. Lett.*, vol. 105, no. 24, p. 241907, 2014.
- [97] J. Harrison, “Fast and Accurate Bessel Function Computation,” in *2009 19th IEEE Symposium on Computer Arithmetic*, 2009, pp. 104–113.

ABSTRACT (KOREAN)

강체벽 배열 설계를 통한 음향 메타물질의 광대역 흡차음 성능 구현

양 지 은

서울대학교 대학원

기계항공공학부

본 연구는 광대역 흡차음 성능을 갖는 음향 메타물질을 설계하는 것을 목표로 한다. 음향 메타물질이란 일반적으로 존재하는 물질에서는 찾아볼 수 없는 독특한 음향학적 특성을 갖도록 설계된 물질을 말한다. 음향 메타물질에 관한 연구는 새로운 기술의 지평을 여는 새로운 학문으로, 특히 이의 소음 저감 분야에의 응용 연구가 활발히 진행되어 왔다. 그러나 현재까지 제안된 음향 메타물질은 그 성능이 매우 좁은 주파수 대역에서만 작용한다는 한계를 가지고 있다.

광대역 흡차음 성능 구현을 위한 가장 큰 장애물은 구현하고자 하는 음향 시스템의 주어진 제한된 크기 혹은 두께를 유지하면서 그 시스템이 효과적인 성능을 발휘하는 주파수 범위를 확장시키는 것이다. 해당 문제

의 해결을 위해 본 연구에서는 음향학적 강제 특성을 갖는 얇은 벽으로 이루어진 구조를 사용하여 설계한 음향 메타물질을 제안한다. 본 논문에서 설계한 음향 메타물질은 구체적으로 흡음 성능을 목적으로 하는 다공성 흡음재와 차음 성능을 목적으로 하는 구멍이 있는 형태의 음향 투과층을 기반으로 한다. 제안한 음향 메타물질 설계에 사용된 강제벽은 특정한 형상으로 삽입되어 음향 도파관이나 공명기와 같은 역할을 할 수 있으며 제안한 음향 메타물질 내부에서 이 구조적 특징에 따른 독특한 파동 전파 현상을 발생시킨다. 이를 이용하여 구조물 내부 파동의 유효 전파 거리 혹은 유효 전파 속도를 조절할 수 있게 되며 이에 따른 파동 현상에 의해 제안한 메타물질의 흡차음 성능은 같은 두께 혹은 크기를 갖는 기존의 흡차음 구조에 비하여 저주파를 포함하는 넓은 주파수 대역에서 획기적으로 향상된다.

제안한 음향 메타물질에서 나타나는 물리적 현상을 효과적으로 설명하기 위해 유효 매질 모델링에 기반한 이론적 해석을 제시하며 이를 검증하기 위한 수치해석 및 실험 결과를 제시한다.

주요어: 음향 메타물질, 소음 저감, 광대역 성능, 흡음, 차음,

메타포러스 물질, 유효 매질 모델

학 번: 2010-24065